Soliton Structures in Bose-Einstein Condensates

by

Harry Proud

A thesis submitted to
The University of Birmingham
for the degree of
DOCTOR OF PHILOSOPHY

Ultracold Atoms Group
School of Physics and Astronomy
College of Engineering and Physical Sciences
The University of Birmingham

February 2018

Abstract

The generation of dark solitons in Bose-Einstein condensates has been an area of interest since the first experimental condensates were produced. The ubiquity of solitons in the natural world makes them an important phenomenon to understand. Despite excellent theoretical work in two dimensional dark solitons, few experiments have had the opportunity to investigate this regime.

The work presented investigates the generation of dark solitons in a Rb-87 Bose-Einstein condensate. The evolution and decay of these topological excitations are investigated. The decay of the dark solitons is found to vary with the phase-step used to generate them. Dark solitons created with a phase-step width of 0.60 $\pm$ 0.15μm are found to decay into vortices after 10 ms. Dark solitons generated with larger phase-steps are found not to exhibit this vortex decay, instead dissipating over 10-15 ms back into the condensate.

The first experimental generation of two dimensional Jones-Roberts solitons is reported in this work. These dark solitons differ from the standard planar dark soliton in that they are finite in extent and are found to be more dynamically stable. The Jones-Roberts solitons are observed for 40 ms with no observed change in energy.

ACKNOWLEDGEMENTS

I would first like to thank Prof. Kai Bongs for giving the me the opportunity to experience the world of ultra-cold atoms over summer studentships as an undergraduate. Working alongside other members of the Birmingham group really inspired me to continue on in the field. I would like to acknowledge the financial support of the Leverhulme Trust, without which the work presented would not been possible.

Learning how to manage a large Bose-Einstein condensate experiment was a daunting prospect. Dr. Michael Holynski, Dr. Marisa Perea-Ortiz and Dr. Charlotte O'Neale were very patient in explaining and teaching me the quirks of the system and the design choices they made in the experiment construction. I'm indebted to the previous students who built and qualified the system from the ground up.

My supervisor during my time on the experiment was Dr. Nadine Meyer. Her experience and support made the daily pushing of the experiment into new territory a much more enjoyable venture. Discussion was always welcomed and her guidance in all matters was greatly appreciated. I was also lucky enough to spend a brief amount of time with Dr Giovanni Barontini with whom there were plenty of discussion about the Jones-Roberts solitons.

The fellow students in the group provided great discussion, relevant and irrelevant, as well as comparing trials and tribulations of the day. No matter what people were up to, there was always a helping hand.

I'd like to thank my parents for the support and interest they provided during the process. They always asked questions, wanting to understand what I was up to in the basement of the building.

Finally I'd like to thank Nicole for being there to help me throughout the whole process. Her love, intellect and dedication to her own profession inspired me to continue working towards the end.

CONTENTS

LIST OF FIGURES

LIST OF TABLES

CHAPTER 1

INTRODUCTION

The work presented in this thesis is focussed on the topic of soliton structures which are experimentally generated in Bose-Einstein condensates and the first experimental realisation of the 2D Jones-Roberts soliton. The production of topological structure in Bose-Einstein condensates has been a rich field since the first experimental realisation of the Bose-Einstein condensation effect in 1995 by W.Ketterle, C.Wieman and E.Cornell. This achievement was recognised in 2001 when they received the Nobel Prize for Physics. Over time the production of Bose-Einstein condensates has become common in institutions around the world. Bose-Einstein condensates are a desirable resource as they are highly controllable and clean testing grounds. Experiments using Bose-Einstein condensates can range from atom interferometry [27] to the simulation of Hawking radiation [61]. The non-linear nature of Bose-Einstein condensates allow the formation of long lived structures such as dark solitons, vortices and Jones-Roberts solitons. The importance of generating these structures in condensates is the ability to mimic different systems using the condensate as an analogue. A recent example of this is with ray solitons, which are dark solitons with an intermediate contrast, being utilised to simulate the event horizons of black holes, which has indicated verification of Hawking radiation [61].

One of the first forms of topological excitation generated in experimental condensates was a vortex lattice. This was done by imparting rotation to the condensate via a stirring laser beam leading to the formation of vortices. The vortices manifest as low density regions of the condensate where the rotation of the condensate is quantised. Vortices are distributed in the condensate which minimises the potential energy in the condensate.

Solitary waves, or solitons, were produced in Bose-Einstein condensates shortly after the first vortices [14]. The lifetimes of the first dark solitons in Bose-Einstein condensates are tens of milliseconds as they decayed away to instabilities. The stability of experimental dark solitons was improved through advances

in creating lower temperature condensates, around 30 nK [8], as well as changing the dimensionality of the condensate in which the soliton is created. Dark solitons are more stable in lower dimensions as there are fewer energetically accessible trap modes for the soliton to excite. This reduction in dimensionality is achieved by highly confining an axis of the condensate, increasing the energy required to excite that mode. The dimensionality of the dark soliton is determined by the trapping frequencies of the condensate that the soliton is produced in. Condensates with quasi 1D and 3D dimensionality are more regularly produced by experiments, which has resulted in a gap of experimental investigation of 2D dark solitons and their evolution. The properties and collapse of 2D dark solitons in a condensate are presented in this thesis.

Within the family of 2D dark solitons another branch of excitation was identified. Jones-Roberts solitons were identified theoretically in 1982 [39]. The physical structure and behaviour of a Jones-Roberts soliton was found to vary with a dispersion curve linked to the dimensionality of the medium it was created in. A 3D Jones-Roberts soliton exists as a vortex ring or as a rarefaction pulse, whilst a 2D Jones-Roberts soliton is a pair of bound vortices or a rarefaction pulse, depending on the soliton energy. The first experimental production of Jones-Roberts solitons in a Bose-Einstein condensate is presented in this thesis. Their creation, using a phase-imprinting method, allows for the future testing of their properties and investigation into their potential as signal carriers in a condensate where the standard dark soliton is found to decay away to instability.

The experimental apparatus was designed to become a quantum simulator, with soliton physics as one of the many avenues it can investigate. The combination of the micro-mirror Spatial Light Modulator (SLM) and the tunable wavelength of the Ti-Saph laser leads to future programmable dipole potentials. The Ti-Saph is measured to be stable to ± 0.001 nm using an optical wavemeter during the soliton imprint process. Efforts are made towards creating both 1D and 2D lattice potentials by changing the image loaded to the spatial light modulator. A simple interference measurement is made to verify that there is still a degree of coherence between lattice populations.

Thesis Outline

The content of the thesis is as follows:

- **Chapter 2**: The relevant theory of Bose-Einstein condensation is presented. This will involve discussion of the Gross-Pitaevskii equation, leading to key physical properties of the condensate relevant for soliton description.

- **Chapter 3**: The experimental apparatus is presented with a focus on the characterisation of the optical

system responsible for the phase imprinting of dark solitons and imaging of the condensate. The optical resolution of multiple arrangements of the microscope system are measured, as the optical resolution can limit the size of soliton produced.

- **Chapter 4**: Presentation of soliton theory is given with solutions to the 1D Gross-Pitaevskii equation. The properties of the 1D dark soliton are covered with an inclusion to two dimensions. The data for solitons being produced is then displayed. Dark solitons produced with a higher optical resolution are found to evolve differently to those generated with lower optical resolution.

- **Chapter 5**: Discussion of the Jones-Roberts soliton is first covered. The Jones-Roberts soliton properties are then examined in both the three dimensional and two dimensional case. The first experimental production of 2D Jones-Roberts solitons is presented with the observed evolution including comparison with simulation. Good agreement between experiment and simulation is found.

- **Chapter 6**: The future outlook of the experiment is detailed. Preliminary experimental work into the Kibble-Zurek mechanism is outlined. Through hastening the quench across the critical temperature, the likelihood of spontaneous vortex formation is found to increase. The technical capabilities of the spatial light modulator (SLM) are also outlined as a potential area of development. Optical potentials of various shapes and structures are presented where the SLM potential is combined with that of the optical harmonic trap.

- **Chapter 7**: The conclusion summarises the results of this thesis.

CHAPTER 2

THEORY

In this chapter the relevant theory of Bose-Einstein condensation (BEC) will be introduced. The mean-field description of BEC using the Gross-Pitaevskii equation (GPE) is presented. Important parameters of the condensate such as speed of sound are discussed. These condensate properties will be required for understanding dark soliton theory as well as interpreting the experimental data.

2.1 Bose-Einstein Condensation

The theoretical basis for a quantum degenerate gas began in the early twentieth century with the initial work of Satyendra Nath Bose on the distribution of particles among energy states [12]. It was in collaboration with Albert Einstein in which the statistics of identical point-like particles were formulated and led to the concept of a condensation-type effect. Despite this early theoretical work, experimentalists had a longer journey realising the Bose-Einstein condensation effect.

It was a widely held view that everything would condense to a solid as it got colder, limiting the density of the sample, which in turn prevented the crossing of the quantum phase transition. Spin-polarized hydrogen and liquid Helium were identified as the first good candidates for achieving Bose-Einstein condensation as they were known to remain fluid as the temperature tended to zero. Helium remains liquid at low temperature due to a low mass and a large zero-point kinetic energy which prevents solidification [40]. Decades of advances in cooling methods, as well as changing the condensation medium to alkali earth metal sources, was finally rewarded in 1995 when the groups of Ketterle and Philips achieved Bose-Einstein condensation in an alkali gas system [41]. The change to alkali metals to achieve a dilute gas Bose-Einstein condensate was possible as the low density of the alkali vapour results in a suppressed recombination process, allowing the alkali to remain gaseous during the cooling to BEC [40]. Today many labs have achieved Bose-Einstein condensation

in various species including sodium, rubidium and strontium, allowing for a wealth of investigations into a wide array of areas of quantum physics [3][66][62].

2.1.1 Bosons and Condensation

Particles with integer total spin are bosons. The framework for the statistical properties of an ensemble of bosons was set out by Satyendra Nath Bose in 1924 and was extended following collaboration with Albert Einstein [12]. It was found that the distribution of bosons across the available energy levels of a system is described by the Bose-Einstein distribution

$$f_{BE}(\epsilon) = \frac{1}{e^{\beta(\epsilon-\mu)} - 1} \tag{2.1}$$

where $\beta = 1/k_B T$, where k_B is the Boltzmann constant, T is temperature and μ is the chemical potential. At high temperature the Bose-Einstein distribution approximately becomes a Maxwell-Boltzmann distribution. As the temperature lowers towards zero, more bosons begin to occupy the ground state. When the number of atoms in the ground state N_0 becomes macroscopic, the system has undergone Bose-Einstein condensation.

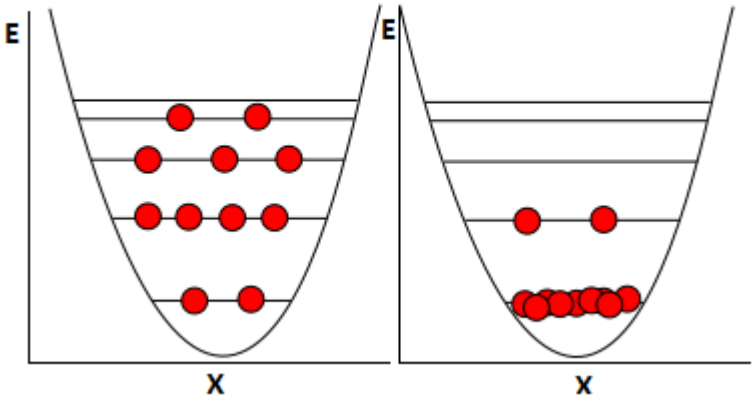

Figure 2.1: The schematics of two energy distributions, the left being uncondensed and the right being condensed.

Bose-Einstein condensation is a phase transition which occurs when the thermal De Broglie wavelength λ_{DB} of bosons of mass m becomes larger than the inter-atomic distance. Beginning with the wavelength of a particle

$$\lambda = \frac{h}{p} \tag{2.2}$$

$$p = \sqrt{2mE_k} \tag{2.3}$$

$$\lambda = \frac{h}{\sqrt{2mE_k}} \tag{2.4}$$

where $E_k = \pi k_B T$ is the non-relativistic kinetic energy of a particle. Substituting E_k gives the thermal De Broglie wavelength

$$\lambda_{DB} = \frac{h}{\sqrt{2\pi m k_B T}} \tag{2.5}$$

As λ_{DB} increases, the wave functions of different atoms begin to overlap. This phenomenon can be characterised by a quantity known as the phase space density (PSD). Phase space density relates the value of λ_{DB} and the peak number density n of atoms. It is defined as $PSD = n\lambda_{DB}^3$. The phase space density at the onset of Bose-Einstein condensation is given by $n\lambda_{DB}^3 = 1$. The physical interpretation of $PSD \geq 1$ is that the volume generated by thermal wavelength begins to contain more than an individual atom which is a departure from classical particle dynamics where $PSD \ll 1$.

The critical temperature [20], T_c, at which condensation begins can is obtained by considering how many atoms are supportable in the system before mass occupation of the ground state begins. The number of particles N at temperature T in the grand-canonical ensemble is given by [21]

$$N = \sum \frac{1}{\exp\left(\beta(\epsilon_{n_x,n_y,n_z} - \mu)\right) - 1} \tag{2.6}$$

where $\beta = 1/k_B T$ and ϵ_{n_x,n_y,n_z} is the energy levels in the three dimensions. As the temperature lows past the critical temperature T_c, there is mass occupation of the ground state ϵ_{000}. The atoms occupying the ground state can be distinguished from the total particle N as N_0. The condensed atoms N_0 tend to N in a condensed system where the chemical potential becomes equal to the lowest energy state. The chemical potential in this case is given by

$$\mu \to \mu_c = \frac{3}{2}\hbar\bar{\omega} \tag{2.7}$$

where $\bar{\omega}$ is the arithmetic mean of the trap frequencies. Subtracting the condensed atoms from the total number gives

$$N - N_0 = \sum_{n_x n_y n_z \neq 0} \frac{1}{\exp\left[\beta\hbar\left(\omega_x n_x + \omega_y n_y + \omega_z n_z\right)\right] - 1} \tag{2.8}$$

The assumption that the energy level spacing decreases as $N \to \infty$ leads to the integral [21]

$$N - N_0 = \int_0^\infty \frac{dn_x dn_y dn_z}{\exp\left[\beta\hbar\left(\omega_x n_x + \omega_y n_y + \omega_z n_z\right)\right] - 1} \tag{2.9}$$

This approach relies on the excitation energies being much larger than the level spacing enforced by the trap frequencies. This is a good assumption if the trapped atom number is high as well as $k_B T \gg \hbar\omega_{ho}$. The integral can be calculated by performing the substitution $\beta\hbar\omega_x n_x = \bar{n}_x$. For a gas trapped in a harmonic potential, the result is

$$N - N_0 = \zeta(3)\left(\frac{k_B T}{\hbar\omega_{ho}}\right)^3 \tag{2.10}$$

The critical temperature T_c can be obtained by considering that there are no condensed atoms at the critical temperature, thus $N_0 = 0$. This results in

$$k_B T_c = \hbar\omega_{ho}\left(\frac{N}{\zeta(3)}\right)^{\frac{1}{3}} = 0.94\hbar\omega_{ho}N^{\frac{1}{3}} \tag{2.11}$$

The condensate fraction can be obtained by inserting the above equation for T_c into the Equation 2.10. This results in

$$\frac{N_0}{N} = 1 - \left(\frac{T}{T_c}\right)^3 \tag{2.12}$$

where N_0 is the number of atoms in the ground state out of possible total of atoms N [40]. At low temperatures where ballistic expansion may not provide an accurate measure, measuring the condensate temperature using the fraction is a viable technique.

2.1.2 Gross-Pitaevskii Equation

The effect of atom-atom interaction on Bose-Einstein condensation is modelled by the Gross-Pitaevskii equation (GPE). The GPE was independently derived by both Gross and Pitaevskii in 1961 [21]. The GPE is a non-linear mean-field approximation of the time dependent Schrödinger equation.

A gas of N bosons can be described as a many-body problem where the second quantised Hamiltonian of the Bose field operator $\hat{\Psi}$ is given by [21]

$$\hat{H} = \int d\mathbf{r}\hat{\Psi}^\dagger(\mathbf{r})H_0\hat{\Psi}(\mathbf{r}) + \frac{1}{2}\int d\mathbf{r}d\mathbf{r}'\hat{\Psi}^\dagger(\mathbf{r})\hat{\Psi}^\dagger(\mathbf{r}')V_{int}(\mathbf{r}-\mathbf{r}')\hat{\Psi}(\mathbf{r}')\hat{\Psi}(\mathbf{r}) \tag{2.13}$$

where V_{int} is the two body interaction potential by bosons at $\mathbf{r}$ and $\mathbf{r}'$, $H_0 = -\frac{\hbar^2}{2m}\nabla^2 + V_{ext}(\mathbf{r})$ where V_{ext} is

the external trapping potential.

The creation and annihilation operators $\hat{\Psi}^\dagger(\mathbf{r})$ and $\hat{\Psi}(\mathbf{r})$ satisfy the following relations

$$\left[\hat{\Psi}(\mathbf{r}), \hat{\Psi}^\dagger(\mathbf{r}')\right] = \delta(\mathbf{r} - \mathbf{r}') \tag{2.14}$$

$$\left[\hat{\Psi}(\mathbf{r}), \hat{\Psi}(\mathbf{r}')\right] = \left[\hat{\Psi}^\dagger(\mathbf{r}), \hat{\Psi}^\dagger(\mathbf{r}')\right] = 0 \tag{2.15}$$

Using the Heisenberg relation $i\hbar\frac{\delta\hat{\Psi}}{\delta t} = \left[\hat{\Psi}, \hat{H}\right]$ and commutation relations for the field operators yields [21]

$$i\hbar\frac{\delta\hat{\Psi}(\mathbf{r},t)}{\delta t} = H_0\hat{\Psi}(\mathbf{r},\mathbf{t}) + \int d\mathbf{r}'\hat{\Psi}^\dagger(\mathbf{r}',t)V_{int}(\mathbf{r}'-\mathbf{r})\hat{\Psi}(\mathbf{r}',\mathbf{t})\hat{\Psi}(\mathbf{r},t) \tag{2.16}$$

The mean-field approximation allows the decomposition of the Bose field operator $\hat{\Psi}(\mathbf{r},\mathbf{t})$ into two components given by

$$\hat{\Psi}(\mathbf{r},t) = \psi(\mathbf{r},t) + \hat{\Psi}'(\mathbf{r},t) \tag{2.17}$$

where $\psi(\mathbf{r},t) = \left\langle\hat{\Psi}(\mathbf{r},t)\right\rangle$ is the classical field expectation value. For a BEC, $\psi(\mathbf{r},t)$ is the mean-field order parameter corresponding to condensed atoms. The second term, $\hat{\Psi}'(\mathbf{r},t)$, corresponds to fluctuations about the expectation value and can be associated with atoms which are not condensed. This term can be removed by considering the atoms at $T = 0$ where all atoms are condensed.

The dilute nature of the trapped gas means that the atom-atom interactions are dominated by s-wave scattering length a. This results in an interaction potential given by

$$V_{int}(\mathbf{r}'-\mathbf{r}) = g\delta(\mathbf{r}'-\mathbf{r}) \tag{2.18}$$

$$g = \frac{4\pi\hbar^2 Na}{m} \tag{2.19}$$

Substituting this interaction potential and considering the atoms at $T = 0$ gives the Gross-Pitaevskii equation

$$GPE = i\hbar\frac{\delta\psi(\mathbf{r},t)}{\delta t} = \left(-\frac{\hbar^2}{2m}\nabla^2 + V_{ext}(\mathbf{r}) + g|\psi(\mathbf{r},t)|^2\right)\psi(\mathbf{r},t) \tag{2.20}$$

The time-independent GPE can be arrived at by substituting the solution $\psi(\mathbf{r},t) = \phi(\mathbf{r})e^{-i\mu t/\hbar}$ which results in

$$\left(-\frac{\hbar^2}{2m}\nabla^2 + V_{ext}(\mathbf{r}) + g|\phi(\mathbf{r})|^{\mathbf{2}}\right)\phi(\mathbf{r}) = \mu\phi(\mathbf{r}) \tag{2.21}$$

In the limit that the interaction energy dominates the kinetic energy it is possible to neglect the contribution

of the kinetic energy. This is called the Thomas-Fermi approximation (TFA). It is applicable where the gas is still considered dilute. Being dilute requires $N > \frac{a_{ho}}{a}$ where a_{ho} is the harmonic oscillator length $a_{ho} = \sqrt{\frac{\hbar}{m\omega}}$. Applying the TFA to the GPE results in

$$\left(V(\mathbf{r}) + g|\psi|^2\right)\psi = \mu\psi \tag{2.22}$$

This can be rearranged to show that the density of the condensate is given by

$$|\psi|^2 = n(r) = \frac{\mu - V(\mathbf{r})}{g} \tag{2.23}$$

Which if the trap is harmonic, provides an inverted parabola as the shape of the ground state density distribution when $\mu > V(\mathbf{r})$. Outside this condition the density is zero. Taking the centre of the harmonic trap, the number density is given by

$$n_0 = \frac{N\mu}{g} \tag{2.24}$$

The benefit of using the GPE with the TFA is that it is possible to describe the entire ensemble with a single wave function, without having to calculate the individual wave functions of each atom within the condensate. This leads to simpler simulation and calculation within the limits of the approximations taken.

2.2 Properties of a Bose-Einstein Condensate

In the Thomas-Fermi approximation, the condensate density distribution is not smooth at the edge of the condensate. The number density goes to zero at a distance from the centre of the condensate given by Thomas-Fermi radius

$$R_{x,y,z} = \sqrt{\frac{2\mu}{m\omega_{x,y,z}^2}} \tag{2.25}$$

The infinite gradient at the Thomas-Fermi radius is not physical. The smallest distance over which the condensate wave function can change is denoted by ξ, the healing length. As the BEC is super fluid, the maximum fluid velocity is set by equating the kinetic energy of the atoms at the BEC edge to the energy of the system, the chemical potential. Atoms travelling faster will escape the condensate, leading to μ setting

an upper energetic limit. The chemical potential and healing length are given by

$$\frac{\hbar^2}{2M\xi^2} \simeq \mu = \frac{gn_0}{N} = \frac{4\pi\hbar^2 a n_0}{M} \tag{2.26}$$

$$\xi = \frac{1}{\sqrt{8\pi a n_o}} = \frac{\hbar}{\sqrt{2m\mu}} \tag{2.27}$$

The healing length is generally of the order of $\xi \simeq 1\mu$m for a Rb-87 condensate of the order of 10^5 atoms, making it a small correction to the to the overall size of the condensate compared to the Thomas-Fermi radius. The healing length is important as it provides a size scale for excitations such as vortices and dark solitons.

The BEC can react to disturbances through particle collisions, which are mediated at the Bogoliubov speed of sound. This is given by [21]

$$c_s = \sqrt{\frac{\mu}{m}} \tag{2.28}$$

Using the healing length and the speed of sound, the shortest timescale over which the BEC wave function reacts can be calculated. This is given by the parameter known as the coherence time of the BEC

$$\tau_c = \frac{\xi}{c_s} = \frac{\sqrt{m}\hbar}{\sqrt{2m}\mu} = \frac{\hbar}{\sqrt{2\mu^2}} \approx \frac{420 \text{ nm}}{1.2 \text{ mm/s}} \approx 1 \text{ ms} \tag{2.29}$$

The coherence time is important for phase engineering exercises used in soliton production as τ_c acts as an upper limit for the period of exposure to the altered potential. If the BEC experiences the altered potential for longer than the coherence time, the condensate will begin to find the lowest energy density distribution of the new combined potential which is not the purpose of a phase imprint.

2.3 Conclusion

This chapter introduces the the concept of the Bose-Einstein condensate and other important concepts such as the condensate fraction. The Gross-Pitaevkii equation is discussed and how it can describe the condensate as a mean-field based theory. The Thomas-Fermi approximation is introduced and the important properties of a Bose-Einstein condensate are detailed. The healing length and speed of sound are important for understanding the dark solitons discussed later in this work.

CHAPTER 3

EXPERIMENT

This chapter covers the experimental apparatus and sequence used to create and image the BEC and dark solitons. The key experimental components are described and discussed. An emphasis in this chapter is placed on the dipole trap geometry as this defines the dynamics of the condensate. The high resolution optical system used to generate and image the soliton excitation is also detailed as this was installed and optimised to collect the data in this thesis.

3.1 Experimental Apparatus

The experimental set-up has been heavily detailed previously [49, 35, 6, 54, 1], covering the construction and performance of the experiment. As a result of this extensive back catalogue, what shall be presented in this chapter is the first full utilisation of their individual contributions as a single experiment.

3.1.1 Vacuum System

The vacuum system of the experiment comprises of three distinct chambers where trapping and cooling of atoms is performed. These chambers are the 2D Magneto-Optical Trap (MOT) chamber, the 3D MOT chamber and the science cell where the BEC is formed. The 2D MOT chamber has the highest pressure of the system at 10^{-7} mbar, which leads on to the 3D MOT chamber which has a vacuum pressure two orders of magnitude less at 10^{-9} mbar, which leads to the science cell where the vacuum pressure reaches 10^{-10} mbar. This reduction in pressure at each stage is important as lower pressure decreases the likelihood of cooled atoms being heated out of the respective trap through two and three body collisions with the background gas [51]. The reduction in pressure results in an increased lifetime of the atomic sample, where lifetime τ is

modelled by an exponential decay $N(t) = N_0 e^{-\frac{t}{\tau}}$.

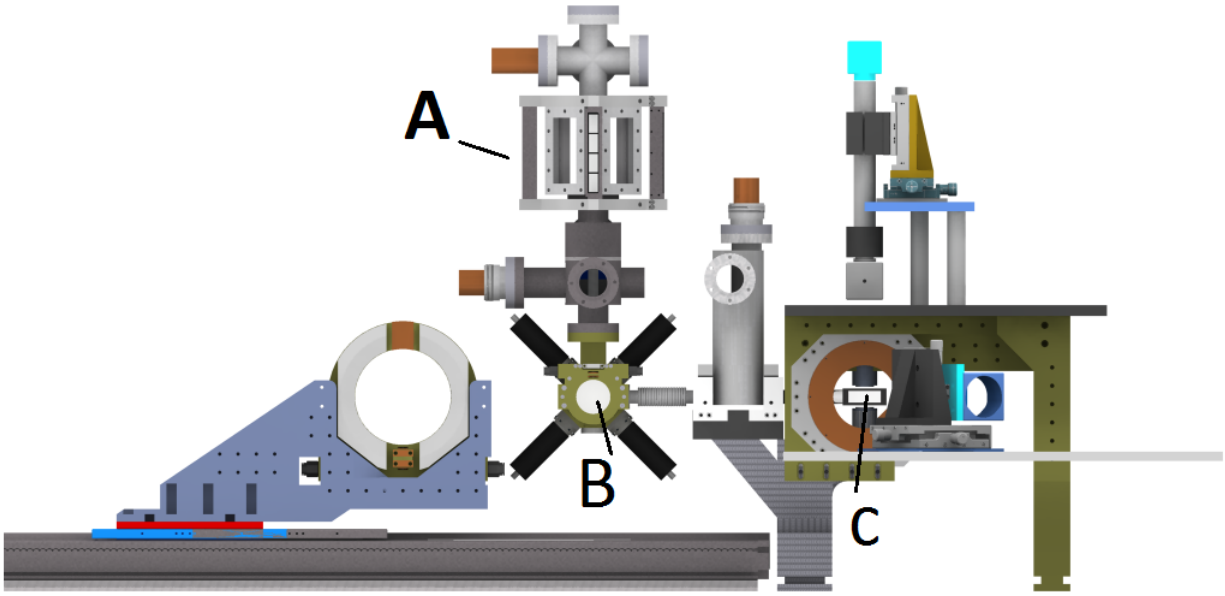

Figure 3.1: Render of the experiment vacuum system and magnetic transport rail. **A** is the 2D MOT chamber, **B** is the 3D MOT chamber and **C** is the science cell where the BEC is formed.

In Figure 3.1, a render of the experiment is presented. The transfer of atoms from the 3D MOT chamber to the science cell is achieved through a moving magnetic trap. The transport process begins with further cooling the atomic sample using a process called optical molasses[1]. Experimentally the optical molasses stage is performed by switching off the magnetic field used for a 3D MOT whilst the three counter propagating laser beam pairs remain on. The optical molasses lasts for 35 ms which prevents the atomic sample from falling too far from the centre of the transport coils. The following stage is optically pumping the rubidium sample. This is done using a 1 ms pulse of light at the D2 transition frequency $2\pi \times 377.11$ THz. This pumps the optical molasses in to the $5P_{3/2}F' = 3$ state before de-exciting to the $5S_{1/2}F = 2$ state [2]. The magnetic potential experienced by the atoms is linearly dependant on the magnetic sub-state of the atom m_F. Optical pumping ensures that a higher proportion of the atoms are low field seekers and will be trapped by the ramped quadrupole field. The anti-Helmholtz coils used to transport the atoms [1] produce a calculated magnetic field gradient of 132.4 G/cm during the experimental sequence. The process of moving the atomic sample takes a total of 0.9 seconds where the coils and cooling system move from the 3D MOT, around a differential

[1] Further discussion of optical molasses is given in Appendix B

[2] The notation of the state is the spectroscopic notation where the F denotes the atomic hyperfine structure. It is given by $\mathbf{F} = \mathbf{I} + \mathbf{J}$ where $\mathbf{I}$ is the nuclear spin contribution and $\mathbf{J} = \mathbf{L} + \mathbf{S}$ is the possible range of angular momentum

pumping stage, to the science cell. The exchange of the atomic cloud between the moving magnetic coils to the science cell magnetic coils is performed by a smooth transition of current, allowing the moving coils to move away from the science cell after a 0.5 second transfer period.

The full loading sequence of the 3D and subsequent transfer of atoms to the science cell is a slow process for this experiment taking 10 seconds to capture 10^8 atoms. Other 3D MOT experiments are able to load at rates up to 3×10^9 atoms/s [52] [1]. It is believed that the slow atom loading rate experienced in this experiment is due to a depleted atomic source resulting in low flux to the 2D MOT. This is overcome by loading the 3D MOT for longer.

3.1.2 Science Cell Lifetime Measurements

The vacuum pressure in the science cell is not static over the course of the data production in this work. Over the course of months, the vacuum pressure degrades leading to a decrease in lifetime of the atomic sample and subsequently a decrease in the efficiency of the experimental sequence. The increase in pressure results in a larger proportion of the atoms lost in processes which do not result in cooling of the cloud. The experimental threshold for the science cell lifetime being acceptable is when τ becomes approximately equal to the time taken for evaporative cooling techniques to reach BEC in the science cell. This experiment generally had a 20 second evaporation sequence.

In order to measure the lifetime, an atomic sample is held in the quadrupole field at the science cell for periods of time of up to 30 seconds. Measuring the number of atoms remaining after different time periods, and fitting an exponential to the decay of total atom number yields the lifetime τ of the sample. This method of measurement assumes that the major atomic loss mechanism is background gas collisions, neglecting other processes such as high density 3-body collisions or interaction with stray resonant light.

[1] There is a reported BEC experiment with a BEC creation cycle time of 1 Hz [26]

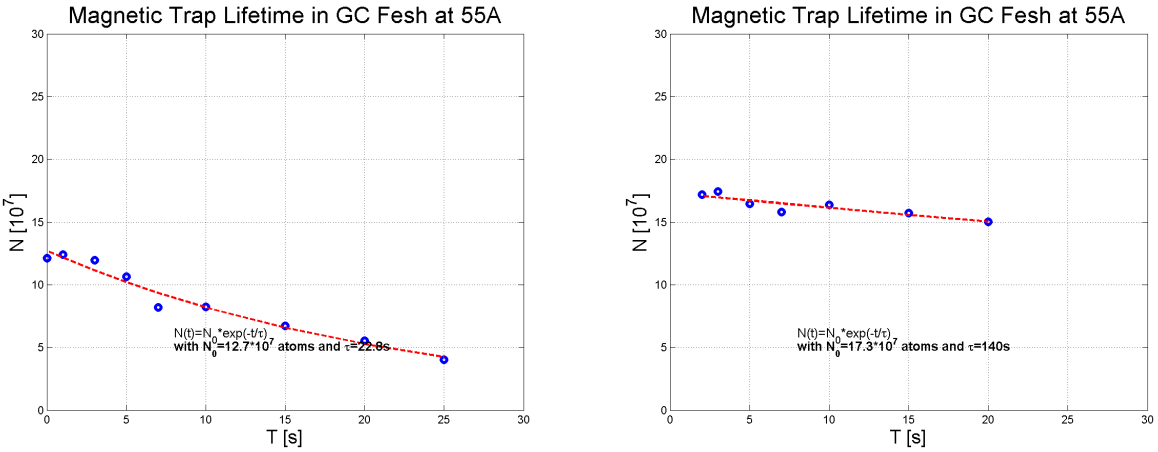

(a) Decemember Prebake

(b) January Postbake

Figure 3.2: Lifetime measurements in the science cell before and after baking. The lifetime of the atomic sample in the science cell improved from 22 seconds to 140 seconds.

The improvement in lifetime presented in Figure 3.2 is from 22 seconds to 140 seconds. As the lifetime of an atomic sample is inversely proportional to the pressure of the vacuum [51], the relative improvement in pressure was a factor of 6.4. The improvement was a result of a vacuum technique called baking. The science cell surface temperature was brought to 90°C for one week, increasing the background gas velocity and resulting in a faster pump rate.

The impact of this procedure is the lowering of the vacuum system pressure and setting a time-scale over which the vacuum would begin to degrade. This presented a time window of 6 months over which the condensation process could be performed reliably.

3.2 Dipole Trap

Once in the science cell, further cooling techniques are utilised to reach the critical temperature where the onset of condensation begins. The number of atoms which make it to the science cell is measured as 2×10^8 with a temperature of 244 $\pm 13 \mu K$. A combination of forced RF evaporation and dipole trap evaporation is used to reach the final condensate.

A dipole trap uses the AC Stark shift effect to generate a confining potential which contains the atomic sample. The discussion of the dipole potential will closely follow Reference [32].

An electric field $\mathbf{E}$ will induce an atomic dipole $\mathbf{p}$ at a frequency ω. The amplitude of this dipole moment

$\tilde{p}$ is related to the field amplitude $\tilde{E}$ given by

$$\tilde{p} = \alpha \tilde{E} \tag{3.1}$$

where α is the complex polarisability, which is dependent on ω. The interaction potential of an induced dipole $\mathbf{p}$ in the field $\mathbf{E}$ is given by

$$U_{dip} = -\frac{1}{2}\langle \mathbf{p}.\mathbf{E} \rangle = -\frac{1}{2\epsilon_0 c} Re(\alpha) I \tag{3.2}$$

where ϵ_0 is the vacuum permittivity and c is the speed of light. The oscillatory nature is accounted for with the 1/2 factor and the intensity $I = 2\epsilon_0 c|\tilde{E}|^2$ is that of the driving field. The real part of the polarisability describes the in-phase component of the dipole oscillation related to the dispersive portion of the interaction [32].

Taking the rotating wave approximation, which states that the detuning of the light Δ must be small compared to the frequency of the optical transition ω_0, ($\Delta = |\omega_0 - \omega_l| \ll \omega_0$), the dipole potential can be rewritten as

$$U_{dip}(r) = \frac{3\pi c^2}{2\omega_0^3} \frac{\Gamma}{\Delta} I(r) \tag{3.3}$$

where Γ is the linewidth of the excited transition of the atom. From Equation 3.3 the only experimentally accessible variables are the detuning and the intensity of the light used to generate the confining potential.

As well as the induced dipole potential, there is also the possibility that the atoms will scatter the photons. The scattering rate is given by

$$\Gamma_{sc}(r) = \frac{3\pi c^2}{2\hbar\omega_0^3} \left(\frac{\Gamma}{\Delta}\right)^2 I(r) \tag{3.4}$$

For an ideal dipole trap, the dipole potential should be maximised whilst minimising the scattering rate. As Equation 3.4 scales inversely with the detuning squared, whilst Equation 3.3 scales only inversely with detuning, using far detuned beams at high intensity is the optimal approach to a successful optical trap. With regard to the nature of the dipole potential, it is dependant on the sign of the detuning Δ. Red detuning ($\Delta < 0$) generates an attractive potential whilst blue detuning ($\Delta > 0$) is repulsive. In this experiment the dipole trap is a red detuning 1550 nm laser used to produce the confining potential where the final evaporation to BEC is performed. The wavelength stability of the dipole trap laser is less critical than that of the lasers used for cycle cooling and repumping transitions. Equation 3.3 shows the relationship between the linewidth of the atomic transition Γ, in this case the Rubidium-87 D2 line $\Gamma = 2\pi.6.06$ MHz $= 3.8 \times 10^7$ MHz[60], and the detuning from that by the dipole laser $\Delta = \omega_L - \omega_0 = 1.2 \times 10^{15}$ Hz as $U_{dip} \propto \frac{\Gamma}{\Delta}$. The detuning term is

so much greater than the linewidth that fluctuations in dipole laser wavelength result in little overall change to the dipole potential experienced by the atoms.

3.2.1 1550 nm Laser Light

The dipole trap is created using a seed 1550 nm laser which is fed to a fibre amplifier with a maximal output of 10 W. The intensity of the light, and thus the trap depth, is controlled by a high power acoustic optical modulator (AOM). The AOM is utilised in the dipole trap evaporation by reducing the light intensity in a timed sequence.

The oblate trap geometry is shaped by a combination of an aspherical lens followed by a cylindrical lens to create a pancake shaped potential.

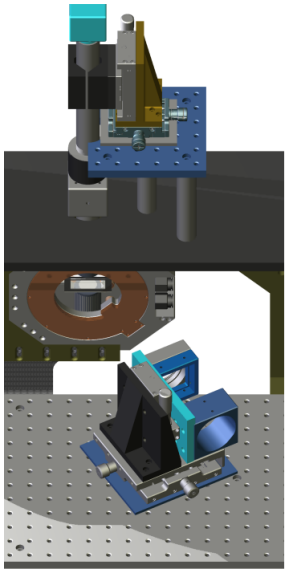

Figure 3.3: Render of the science cell section of the experiment where the condensate is formed in a dipole trap. The dipole trap is directed at an angle to the science cell. This prevents interference effects from retro-reflections from the outer and inner glass faces.

Figure 3.3 displays a render of the science cell section of the system where the 1550 nm light is shaped and introduced to the atoms. The dipole trap shaping lenses are contained in 2" lens tubes which are mounted on a three-axis translation stage. The three-axis stage allowed for precise control of the position of the dipole trap position in the science cell.

3.2.2 Dipole Trap Geometry

In this experiment the trap geometry is a pancake shaped confining potential. The purpose of confining one of the three axes is that this increases the spacing of the energetic states in that dimension. The energy levels of a quantum harmonic oscillator scale proportionately with ω. By using large trapping frequencies ω, it is possible to raise the first excited state E_1 above the chemical potential μ of the condensate. This results in the excited states of the confined dimension becoming energetically inaccessible. The level spacing for a particular dimension is related to the temperature of the condensate by

$$T = \frac{\hbar\omega_{x,y,z}}{k_B} \tag{3.5}$$

Provided the temperature of the condensate is below the first energy level of a dimension, the dimension cannot be accessed. This leads to restricting the dynamics of the condensate to a 2D plane. To achieve this experimentally, the dipole trap is shaped using an aspherical lens and a cylindrical lens. The cylindrical lens displaces the the beam waist in one axis to form a vertical pancake and a horizontal pancake separated by 25 mm. The horizontal configuration was selected as this provided the confined axis parallel to gravity which minimised gravitational displacement. Atoms are found to be trappable in both vertical and horizontal minima.

The trap frequencies of the dipole trap are measured using two techniques which both rely on oscillation of the atomic sample in the trap. The first technique used is known as parametric heating. Parametric heating is achieved by oscillating the trap intensity at a low level eg 20%. The fluctuating intensity results in a time varying dipole potential. If the frequency of the intensity oscillation is far from the trapping frequencies, the movement of the atomic ensemble in the trap does not resonate and there is little heating. This results in low atom loss from the trap. When the frequency of the intensity oscillation is half the trapping frequency or multiples of it, then the motion of the cloud is resonant with the oscillating trap potential and the cloud is efficiently heated leading to large atom loss from the trap.

The second method is a direct measurement of the motion of the condensate once it is formed in the trap. The coils used during the RF evaporation to hold the cloud were pulsed on for 2 ms providing a kick to the cloud through the pulsed magnetic field. The cloud is then imaged both vertically in the trap, and horizontally out of trap in order to assess the motion of the centre of mass. The centre of mass was observed over multiple oscillations to allow for reliable fitting of the trapping frequencies.

Using these methods the frequencies are measured as $\omega_x = 2\pi \times 249.5 \pm 3.1$ Hz, $\omega_y = 2\pi \times 30.0 \pm 1.2$

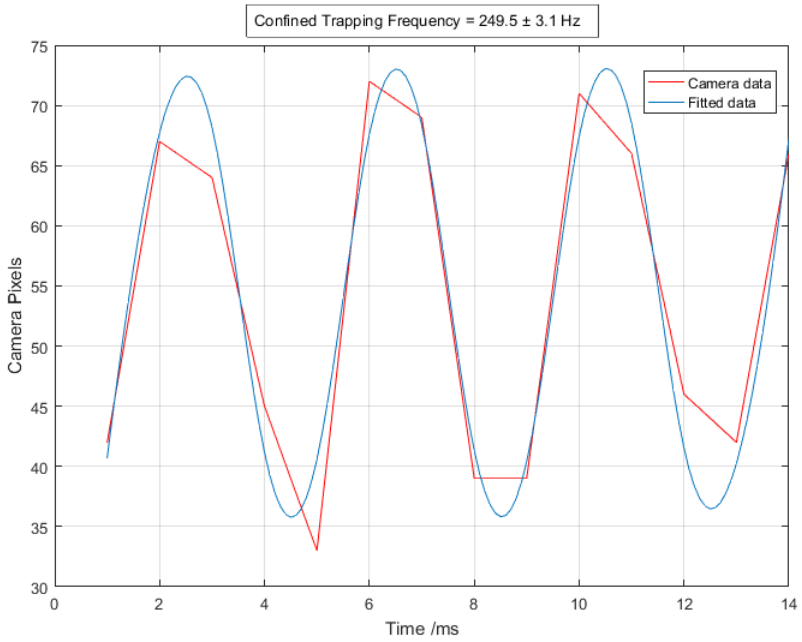

Figure 3.4: The atomic sample is perturbed by a magnetic kick produced by the science cell coils. The atoms are held and released in order to measure the oscillation of the centre of mass of the sample. The absorption images are taken at 35 ms after release.

Hz and $\omega_z = 2\pi \times 4.99 \pm 0.30$ Hz. An example fit of the centre of mass oscillations for the confined axis is displayed in Figure 3.4.

To establish if the 2D regime is achieved, the ratio of the Thomas-Fermi radius in each axis is considered. The Thomas-Fermi radius is given by

$$R_{TF,i} = \sqrt{\frac{2\mu}{m\omega_i}} \tag{3.6}$$

The lower limit for reaching the 2D regime is set when the Thomas-Fermi radius in the confined axis is a factor of 10 smaller than in the other two axes[64]. As the Thomas-Fermi radius is inversely proportional to the trapping frequency in that axis, the ratio of the frequencies is sufficient to check the dimensionality threshold. The ratio of confined and weak is a factor of 50 smaller, but the ratio of the confined and semi-confined axes is a factor of 6 smaller. This result determines that the experimental condensate is three dimensional.

3.2.3 Experimental BEC

The BEC that is generated by the experiment is characterised through absorption imaging. Once the dipole trap evaporation sequence has completed, the condensate is released from the dipole trap and imaged over 35 ms. An example of the condensate expansion during time-of-flight is displayed in Figure 3.5. The sample

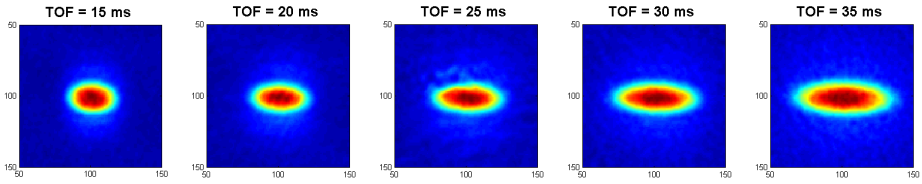

Figure 3.5: Identically prepared condensates released and imaged at times ranging from 15 ms to 35 ms. The characteristic change in aspect ratio is observed, indicating that the sample had condensed.

is considered to have condensed as it no longer expands uniformly after a long expansion. This is as a result of the mean-field interactions imparting velocity at the beginning of the expansion. The repulsive force is proportional to the density gradient of the condensate which is counter to the spatial extent [66]. The most tightly confined axis of the condensate will expand most rapidly. These interactions die away quickly as the initial expansion leads to a rapid decrease in density but the resultant velocity generates a non-Gaussian expansion which leads to the aspect ratio changing over time as observed in Figure 3.5.

The condensate is found to contain 4×10^4 atoms with a condensate fraction of over 80%. This is calculated using a bimodal fit using a parabolic distribution for the condensed fraction and a Gaussian distribution for the thermal fraction.

3.3 Microscopic Potentials and Imaging at the Science Cell

The optical system around the science cell has two requirements for the work presented in this thesis; produce dark solitons in the condensate and image the imprinted condensate. The optical resolution required to produce dark solitons is that the imprint step width is of the order of the condensate healing length $\xi \leq 1$ μm. High resolution microscope objectives are utilised to reach micron levels of imaging. The use of high resolution microscope objectives to both image and manipulate condensates is a common technique [30, 46]. The high resolution objectives and supporting optical design for this experiment had been produced [54] but not utilised fully. The same was true for the spatial light modulator (SLM) which is a micro-mirror array responsible for the shaping of the phase imprint applied to the condensate [1]. The full implementation of the previous students work results in the optical system displayed as a schematic in Figure 3.6

The individual optical sections of this arrangement will be discussed in order to clarify their structure and purpose.

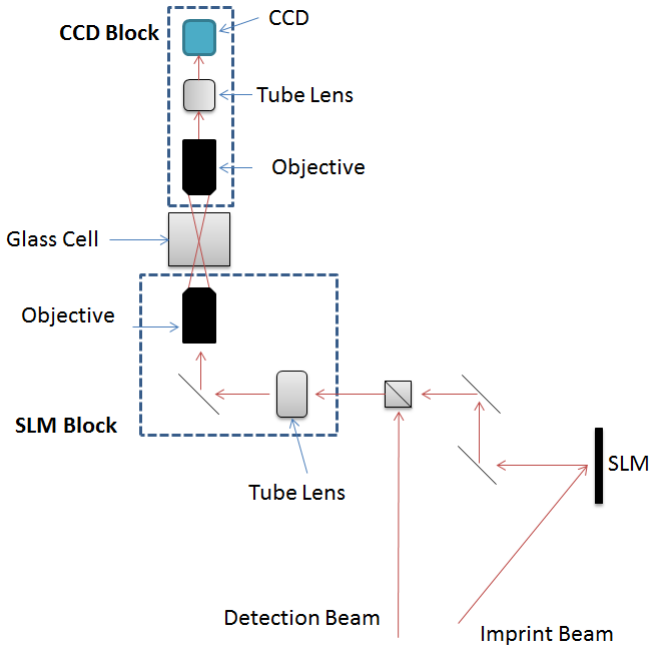

Figure 3.6: Schematic of the optical system around the science cell which generated the optical potentials and high resolution imaging of the condensate

3.3.1 Optical System

The majority of the work performed in this experiment relies on the ability to place spatially variant optical potentials on to the condensate and subsequently image the result. The design of the microscope system was performed and detailed in previous theses [35] [54] [1]. The implementation and optimisation of their design work was required in order to obtain the data presented in this thesis.

CCD Block

The optical system comprises the two telescope systems highlighted in Figure 3.6. The CCD block images the condensate on to the CCD in order to take data. The CCD telescope comprises of an infinity-corrected Mitutoyo objective which is placed at the focal point of a F = 200 mm tube lens. The PixelFly QE CCD tops the telescope, placed at the focal point on the other side of the tube lens. An optical cage containing a polarising beam splitter is placed between the microscope objective and tube lens. The polarising beam splitter redirects the imprint light away from the CCD, preventing damage being done during the soliton imprint. The polarisation of the light used for absorption imaging is orthogonal to that of the light used to illuminate the SLM. The presence of the beam splitter is found not to affect the quality of the camera image.

The CCD telescope is mounted on a three-axis translation stage which is used to position the field-of-view. The translation stages provide a minimum unit of movement of 5 μm in all three dimensions, allowing precise positioning of the CCD telescope.

SLM Block

The SLM telescope performs two functions; providing the light for absorption imaging and imaging the SLM on to the atom plane in the science cell in order to perform phase imprinting. Absorption imaging is a standard technique where the atomic sample is imaged using resonant light. The atomic sample, in this case the condensate, scatters the resonant light. This creates a shadow on the CCD where the opacity is governed by the column density in front of the CCD as image I_{atoms}. A second image $I_{noatoms}$ is subsequently taken after with no atoms in order to provide an intensity reference. The optical density of the cloud is given by [38]

$$OD = -ln\frac{I_{atoms}}{I_{noatoms}} \tag{3.7}$$

The SLM telescope has the same optical form as the CCD telescope, with the microscope objective at the focal point of the F = 200 mm tube lens with a 45 degree mirror mid path. After the tube lens the path bifurcates from a polarising beam splitter into a "detection" path and "SLM" path. A 1" collimated beam is used for absorption imaging with a pair of mirrors for alignment. The SLM path consists of a 1" collimated beam used to illuminate the SLM, with a pair of mirrors which direct the reflected SLM pattern into the tube lens. The SLM is placed at the focal length of the SLM tube lens such that the SLM is imaged correctly at the focal plane in the science cell.

3.3.2 Spatial Light Modulator

A spatial light modulator (SLM), is a device that is used to spatially engineer a light field either through amplitude or phase modulation. Phase modulating SLMs generally use a nematic crystal display to vary the transmitted light. The orientation of the crystals in a pixel is controlled by a voltage across the pixel. The crystal orientation varies the birefringence for each pixel, resulting in a spatially variant phase mask. An amplitude SLM, as used in this experiment, comprises a digital micro-mirror device (DMD) array of 1900 x 1080 mirrors. Each 10 μm square mirror acts as a pixel pivoting on a central axis between an 'on' and 'off' position separated by 48°. The 'on' position directs the light towards the SLM telescope system whereas the 'off' position allows the light to reflect away towards a beam dump. The benefit of a DMD SLM is in the frame rate that the SLM can achieve and the flexibility of the light fields produced. Previous experiments

have required physical masks to be fabricated to produce the spatial distributions of light. The DMD SLM allows for fast and complex light distributions. This is performed by loading a black and white JPEG file through the control software which the DMD displays. The black portions of the image are processed as 'off' and are not passed through the optics to the condensate. As for dynamic patterns, the DMD SLM frame rate limit is tested by oscillating the pattern between completely 'on' and 'off'. A fast acting photodiode is then used to measure the light reflected off of the SLM to measure the frame rate. The quoted frame rate limit of 10 kHz is measured using this process. This limit of 10 kHz is due to the electrical control of the DMD and could be faster with different control electronics. The condensate responds to potentials on a millisecond time scale.

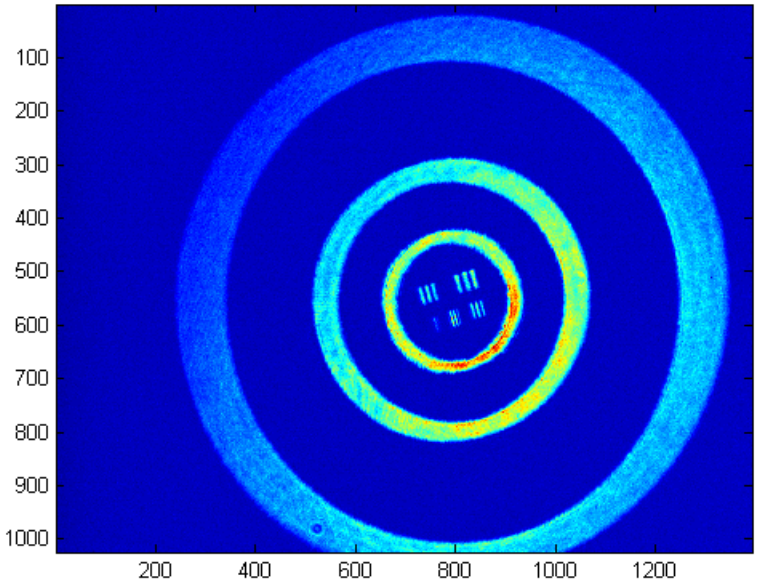

Figure 3.7: Example pattern produced by the micro-mirror SLM imaged through a pair of 20X high resolution objectives. The image corresponds to a total area of 449×352 μm

Figure 3.7 is an example of a bullseye resolution pattern used to optimise the focal position of the objectives. The total area displayed in Figure 3.7 was calculated as 449×352 μm. The centre of the bullseye comprises of groups of three rectangles which get progressively thinner. The CCD block is focussed using a live stream of Figure 3.7 aiming to resolve the smallest group.

3.3.3 SLM Illumination

The light used to generate solitons is required only for tens of microseconds. An acousto-optical modulator, or AOM, is used as an optical switch to control the imprint pulse timing and prevent stray light from reaching the condensate.

The source of the light used for the phase imprinting is an M2 Solstis Ti-Saph pumped by a 12 W Coherent Verdi. The optical output of the Ti-Saph ranges in wavelength between 700-950 nm with maximum output power of 2 W. The frequency stabilisation of the Ti-Saph laser is performed through a cavity locking scheme designed into the Solstis laser. The desired wavelength is selected and locked to using an internal cavity which allows the lasers software to actively maintain the frequency. The wavelength of the Solstis laser is measured using an optical wavemeter to ensure a wavelength stability of ± 0.001 nm. The control of total optical power reaching the SLM is done through polarisation optics prior to the fibre which leads to the AOM.

The illumination beam has a diameter of 1" when reflecting from the SLM. The Gaussian distribution of the intensity is present in the SLM image. The effect of the gradient is minimised by aligning the illumination beam of the SLM and the condensate centre. Over the condensate length the SLM illumination is effectively homogeneous.

The timing of the imprint pulse is confirmed to be accurate by using of a high speed photodiode. Figure 3.8 displays the photodiode signal of a 50 μs which is a typical pulse length for dark soliton generation.

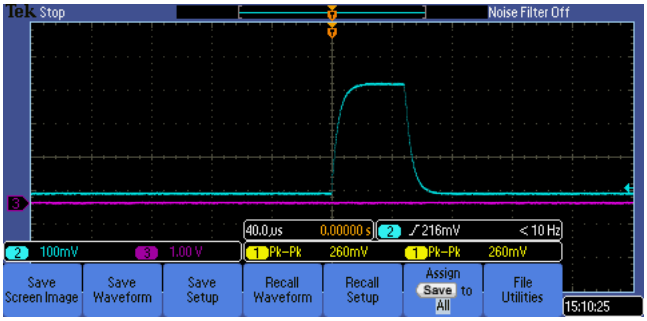

Figure 3.8: 50μs imprint pulse used to generate dark solitons. Trace produced using a fast acting photodiode

Magnification

The magnification provided by the combination of the microscope objectives and tube lens is a key parameter for data analysis. Magnification was stated in the data sheets for the combination of the objective and tube lens, however, with the introduction of other optical elements in the beam path the magnification

required verification. The simplest method of establishing the magnification was to use the translation stages which were used for positioning of the dipole trap, using the BEC in the trap as a point of reference. By displacing the dipole trap by 100 μm either side of the optimal position it is possible to verify that the magnification of the combined CCD telescope was given by the value of the objective selected. Once the CCD telescope was found to be correct, the SLM was then used as the reference for establishing the SLM telescope magnification. Placing images of squares of integer pixel lengths on the SLM it was possible to calculate the level of magnification provided by the SLM telescope.

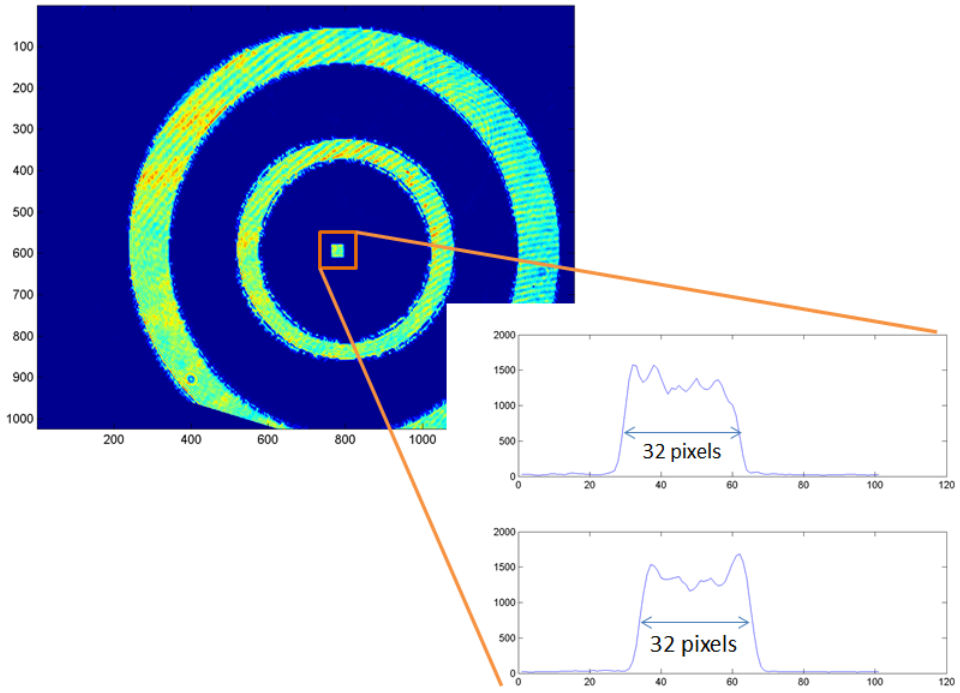

Figure 3.9: Imaging of the SLM in the atom plane of a bullseye with a 10×10 square at the centre. The width of the 10×10 square on the CCD is 32 pixels which corresponds to a real-space size of 206 μm after the 10× microscope magnification. The SLM pixel size was 10.8 μm which gives the magnification of the 5× objective in the SLM path as 5.2×

Figure 3.9 displays the image of the SLM through a 5× objective to the atom plane in the science cell. The CCD uses the 10× objective to take the image in this example. The blue portion of the image is the minimum light intensity, with red being the maximum intensity. At the centre of the rings is a 10×10 SLM pixel square which is used to characterise the magnification of the full optical system.

Using the measured magnification of the CCD telescope, the 10×10 pixel square of the SLM was measured as 206 μm in the science cell. As the SLM pixel size was 10.8 μm, the magnification of the SLM required to

produce the image was calculated to be 5.23 ±0.11.

Both telescopes produced the expected magnifications and as the objectives were infinity-corrected, it was possible to simply exchange them without changing the tube lens or its position in relation to the microscope objective.

Objective	**Numerical Aperture**	**Point Resolution μm** ($\lambda = 532nm$)
M Plan Apo ×5	0.14	2.3
M Plan Apo ×10	0.28	1.2
G Plan Apo ×20	0.28	1.2
G Plan Apo ×50	0.56	0.63

Table 3.1: Summary of the Mitutoyo microscopes objectives available in this experiment

3.3.4 Imprint Resolution

Characterising the resolution of the SLM in the science cell is important as the optical resolution will set the limit on the size of the soliton that can be created. To investigate the resolution, images of the SLM are taken with the sharp edge which is used to generate the dark solitons.

Figure 3.10 displays the section of the SLM responsible for imprinting the condensate with the dark soliton. The resolution is determined by fitting the image with

$$a\left(1+\tanh\left(\frac{x-x_0}{l}\right)\right)+c \tag{3.8}$$

where a is a scaling factor, x_0 is the horizontal offset of the edge, l is the resolution of the edge and c is scaling offset.

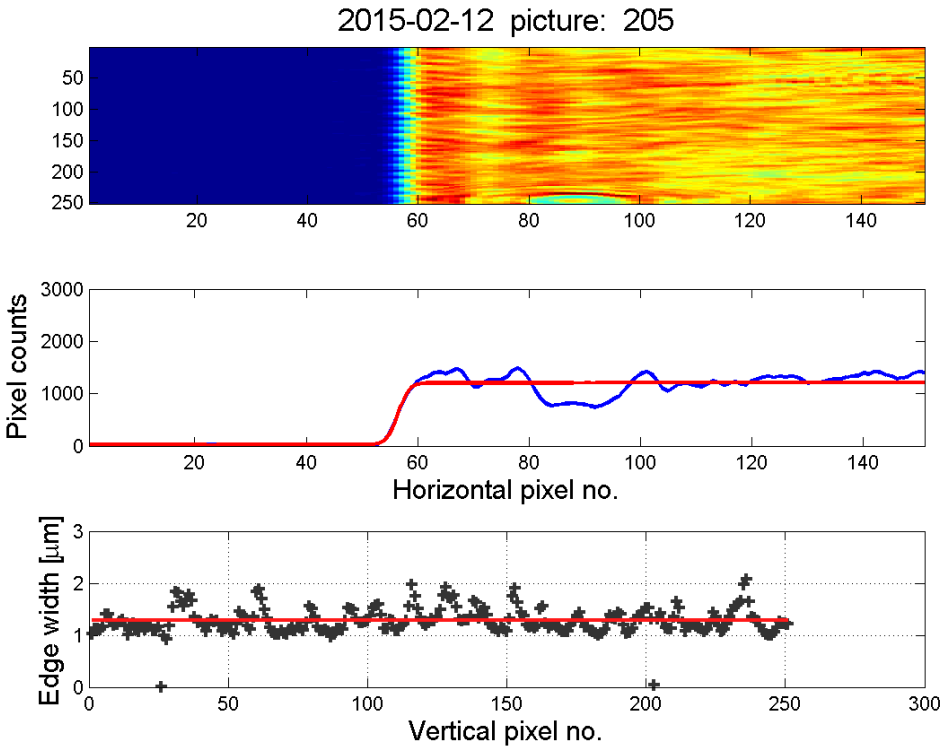

Figure 3.10: Resolution check using 5× objective for the SLM with a 10× objective for the CCD. Below is the analysis of the image displaying the sum with a fit and the residuals of the fit.

3.4 Conclusion

The experimental apparatus has been detailed from the vacuum system to the dipole trap used to create the Bose-Einstein condensate. The dipole trap characterisation is presented, establishing the condensate dimensionality as three dimensional. The high resolution optical system used to generate and image dark solitons is detailed. Measurements of the optical resolution are performed with objectives ranging from 10× to 50×. This is to establish the width of the phase step that is produced. The phase step width is an important factor in the formation and decay of the dark soliton.

CHAPTER 4

DECAY OF DARK SOLITONS IN BOSE-EINSTEIN CONDENSATES

Non-linear partial differential equations are used to describe the dynamics of systems ranging from oceanic deep waves [65] to Morning Glory cloud formations [58]. The Non-linear Schrödinger equation (NLSE) is principally utilised to describe a BEC in an anisotropic trap as well as light in optical wave-guides. Solitons and vortices are excitations which are solutions to the NLSE and can be generated in systems which are described by a NLSE. The importance of these excitations is that they are long-lived and form stable in the condensate [2]. In comparison, a random density fluctuation results in an energy state of the condensate which is larger than the ground state much like the dark soliton, but there is no reinforcing mechanism to maintain the fluctuation. The condensate will relax back to the ground state through dispersive mechanisms at a timescale on the order of the speed of sound in that medium ($c_s \sim 1.3$ mms^{-1}). Solitons and vortices are resistant to dispersion and can persist for many coherence times $\tau_c = \xi/c_s$.

The stability of solitons is due to the balancing of dispersion and kinetic energy of the medium. Thus, the soliton experiences no net dispersion, resulting in form stability. Vortices are form stable as a result of their quantised circulation which is a conserved property. The prevalence of non-linear environments and the longevity of the excitations allow these topological structures to manifest in a wide array of systems. One field where solitons are heavily researched both experimentally and theoretically is in optical wave guides [45, 63, 67, 5]. Solitons also appear in biological systems such as nerve communication and DNA replication [34]. This ubiquity makes soliton dynamics an important area of physics to understand.

The investigation of solitons in Bose condensed gas has been a burgeoning field where theoretical and experiment have been pulling each other along. With the groundwork of the theoretical conditions required

[2]Form stability refers to the property of the excitations to persist without change to their physical form over time

to generate a soliton [37, 59], experimental solitons in BEC were first generated in several experimental groups shortly after the first BEC was produced in 1999 [14, 23]. The first dark solitons generated in Bose-Einstein condensates were short lived, of the order 10 milliseconds. The subsequent increases in soliton lifetime arose primarily from two factors; the decrease in temperature of the BEC and the reduction of the condensate dimensionality as this prevents dynamic instabilities forming [8]. Other extensions in soliton lifetime have been achieved by "filling" the dark soliton with a secondary component condensate[8]. A two component condensate is the combination of two distinct states. The dark soliton is imprinted in one component, addressing the component using a phase imprint that only interacts with one component. The second component condensate then fills the density minimum associated with the imprinted component dark soliton. This results in a dark soliton in one component filled with the bright soliton of the second component. This is unlike a single component BEC where the dark soliton is a density minimum.

Dark soliton experiments in condensates have been performed in the quasi-1D regime and the 3D regime [23][14]. Condensates which reach the 2D condition have been created [18] [57] but experimental work with solitons has not been performed in this regime. It is a difficult regime to reach as it usually requires using multiple off-resonant lasers to confine the condensate heavily in one dimension. Despite experimental difficulty, there have been theoretical investigations such as [36] but there has been little experimental output to verify the theoretical models.

This chapter will introduce the theoretical 1D soliton followed by the extension to solitons in BECs. The role of dimensionality on the dynamic evolution of the soliton will be explored. Dark solitons will be presented from experimental data and discussion of their observed decay paths will be undertaken. Simulation of the experimental system was performed in order to compare the experimental observation to the predicted outcomes.

4.1 1D Soliton

Solitons are single wave packets that do not experience a net dispersion and are a fundamental topological excitation of the NLSE. Solitons and vortices are stable as the dispersion that would normally redistribute density variation is balanced by the non-linearity of the medium in which they are generated. For the BEC case, taking the GPE from the earlier section

$$i\hbar\frac{d}{dt}\psi(r,t) = \left[\frac{-\hbar^2}{2m}\nabla^2 + V(\mathbf{r}) + g|\psi(r,t)|^2\right]\psi(r,t) \tag{4.1}$$

it is possible to locate the non-linear term as the interaction with the mean-field, $g|\psi(x,t)|^2\psi(x,t)$ where $g = \frac{4\pi\hbar^2 Na}{m}$ is the atom-atom interaction term previously mentioned in Equation 2.19. This interaction term balances the dispersion introduced by the kinetic energy in the GPE.

Solitons have both a phase structure and a density distribution. A dark soliton is characterised by a phase distribution resembling a step $\delta\phi = 0$ to π, resulting in a density minimum at the mid-point of the phase gradient. If the phase difference across the soliton is less than π, then the dark soliton is not fully modulated in depth and is described as a grey soliton.

A bright soliton is a single wave packet with a density maximum and a constant phase. Bright solitons require attractive atom-atom interaction to produce the density maxima. This is possible when working with atoms which have a negative s-wave scattering length $a < 0$ such as Lithium-7 where the interaction is attractive [42]. The solution for representing a bright soliton is given by [15]

$$\psi_{bright}(z,t) = \sqrt{n_0}\,\mathrm{sech}\left(\frac{z-vt}{l_0}\right)e^{-i2mvz/\hbar}e^{-ign_0t/\hbar} \tag{4.2}$$

where v is the bright soliton velocity, l_0 is the soliton size and m is the soliton mass. Bright solitons can be difficult to maintain as the attractive interaction strength increases with density, potentially leading to collapse. The work in presented in this thesis only concerns dark solitons generated in a Rb-87 condensate.

In a homogeneous quasi-1D condensate with a repulsive mean-field, a dark soliton can be derived as a solution to the GPE[7]. It has the form

$$\psi(z,t) = \sqrt{n_0}\left(\frac{iv}{c_s} + \sqrt{1-\frac{v^2}{c_s^2}}\tanh\left[\kappa(z-vt)\right]\right)e^{-ign_0t/\hbar} \tag{4.3}$$

where n_0 is the peak number density of atoms, $c_s = \sqrt{\frac{\mu}{m}}$ is the speed of sound in the condensate from the previous section, the position of the soliton is in z with a soliton velocity of v over a time t. The term κ is the length scale over which the phase distribution of the dark soliton goes from 0 to π, given by

$$\kappa = \xi^{-1}\sqrt{1-\frac{v^2}{c_s^2}} \tag{4.4}$$

The equation for κ relates the length of the phase gradient to the velocity of the soliton and the speed of sound in the condensate. During the evolution of a dark soliton, the size $1/\kappa$ is of the order of the healing length ξ.

The depth of the dark soliton is characterised by the ratio of the dark soliton density n_s to the number

density of the unperturbed condensate n_0 at the soliton position. It is given by [7]

$$\frac{n_s}{n_0} = \sin^2(\delta\phi/2) = 1 - v^2/c_s^2 \tag{4.5}$$

where $\delta\phi$ is the phase shift across the soliton feature, v is the soliton velocity and c_s is the speed of sound in the condensate. A fully modulated dark soliton is stationary requiring $n_s/n_0 = 1$ with a corresponding maximal phase step of $\delta\phi = \pi$.

The dark soliton velocity dictates the soliton depth. A fully modulated dark soliton where $n_s = n_0$ has a zero velocity. As the velocity of the dark soliton increases, the soliton depth decreases and width increases. As the velocity reaches the speed of sound in the BEC, the soliton depth becomes zero and the condensate returns to the ground state distribution. The depth of a soliton can be derived from Eq 4.3 by taking the modulus squared of the wave function $\psi(z,t)$ to determine the distribution. The density and phase distribution for dark solitons with $0 \leq v \leq 0.75c_s$ is displayed in Figure 4.1

In a homogeneous 1D BEC, the soliton will propagate at a constant velocity and depth in space and time.

The phase across a dark soliton as shown above in Figure 4.1b, varies heavily over the low density region. The gradient of the phase is related to the soliton velocity, making the gradient larger the closer to stationary the soliton is. The flow of atoms across the two phase regions of the condensate is mediated by a velocity field generated by the phase gradient. The velocity field has the form $v_z(z) = (\hbar/m)\delta\phi(z)/\delta z$ where the soliton centre is considered to be at $z = 0$. Where $\delta v(z)/\delta z$ is positive, a low density region is formed; this is the dark soliton. Where $\delta v(z)/\delta z$ is negative, a high density region builds which then propagates at the speed of sound through the condensate [15]. The difference in evolution between the dark soliton and the density maximum is due to the effect of dispersion and atom-atom interactions. The reduced atom-atom interactions in the dark soliton prevent it from dispersing, whereas the density maximum has an increased interaction energy which does not protect against the dispersion [15]. If the soliton is not fully modulated, then it will propagate in the positive z direction against the atomic flow. A fully modulated dark soliton has no atomic flow across the phase step which leads the dark soliton being stationary.

So far the considered medium in which the soliton has been generated has been homogeneous and thus the parameters of the medium are constant. Experimentally, Bose-Einstein condensates are held in an external potential. The harmonic trap distributes the density of the condensate as a parabola in the Thomas-Fermi approximation. In the quasi 1D case of a elongated harmonic trap, this density distribution only affects the dynamics in so far that the condensate is finite in length. As the soliton travels to the lower density region it reflects in order to preserve the soliton density. With no energy loss mechanisms, the dark 1D soliton

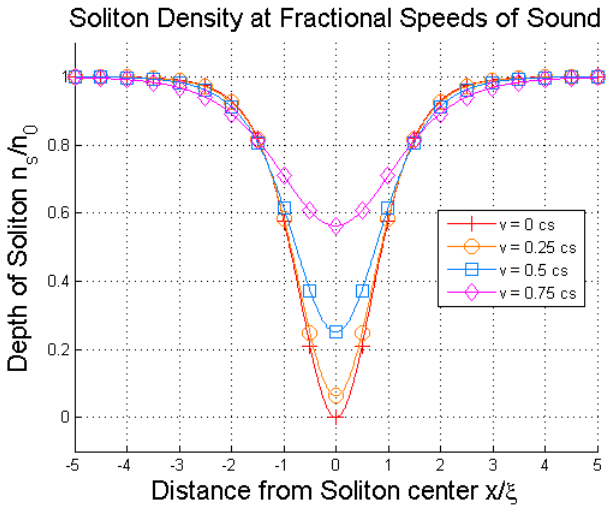

(a) 1D Soliton Depth

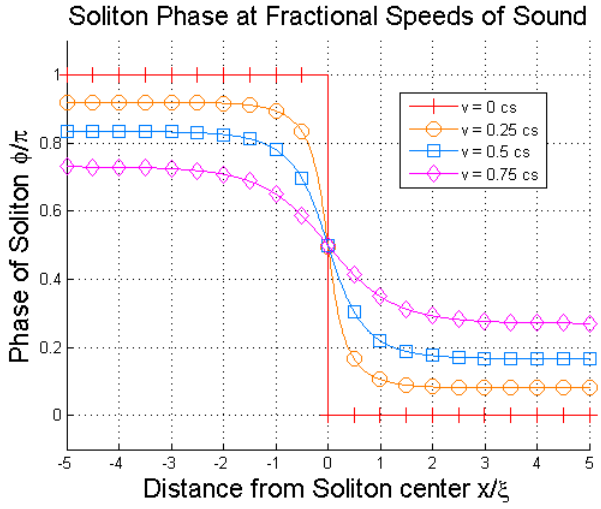

(b) 1D Soliton Phase

Figure 4.1: Depth and phase of a dark soliton in a quasi-1D condensate. The velocity of the soliton is varied in order to show the effect on depth and phase.

oscillates in the trap with a frequency $\omega = \omega_z/\sqrt{2}$. For this experiment $\omega_z = 4.99 \pm 0.3$ Hz, the frequency of longitudinal oscillation of a dark soliton is $\omega = 2\pi 3.54$ Hz. This oscillating behaviour has no effect on the depth of the soliton.

The presence of a dark soliton is an excited state of the system, and by extension it is implied that a dark soliton reaching the speed of sound returns to the ground state of the system. This is because once the dark soliton has accelerated to the speed of sound it has fully dissipated and is no longer present in the condensate. This trend can be observed in Figure 4.1b where the amplitude of the phase slip decreases at higher soliton velocities. There is no longer the characteristic phase slip at $v = c_s$ which leaves only the ground state. The

kinetic energy of the dark soliton can be considered as a negative quantity as the mass of the dark soliton is negative [16]. The dark soliton bare mass is the total number of atoms that would fill the dark soliton given by $M = N_s m < 0$ where N_s is the number of atoms missing to create the dark soliton and m is the mass of the atom [68].

Any dissipative processes will ultimately remove energy from the soliton, reducing its mass and causing the soliton to accelerate. This leads to the soliton becoming wider and shallower. The experimentally generated condensate has a thermal fraction which can scatter off of the dark soliton [53, 28], potentially removing some of the soliton energy. The effect of temperature on the soliton lifetime has been investigated both theoretically and experimentally with a theoretical temperature dependence of the lifetime τ scaling as T^{-4} [28]. A large increase in soliton lifetime into the timescale of seconds was experimentally achieved by reducing the temperature of the condensate to 30 nK[8].

4.2 Dark Solitons in Higher Dimensions

Dark solitons are only dynamically stable in one dimension. In higher dimensions, solitons not only decay through dissipative mechanisms such as the thermal interaction but also through dynamic evolution. The additional degrees of freedom through transverse modes give rise to instabilities known as *snaking instabilities* [48]. First observed in optical wave-guides [63, 48], and theoretically predicted in two and three dimensional Bose condensed systems, snaking instability is the excitation of transverse modes of the condensate. Snaking instability in higher dimensional condensates was predicted as the energetic cost of exciting the transverse modes is lower compared to the quasi-1D case. The instability affects the dark soliton by modulation of the longitudinal depth. The depth modulation translates to a variation in the soliton velocity across the plane. The slowing and acceleration of different areas of the soliton generates bending of the dark soliton transverse density minimum referred to as the nodal plane. The bending acts as positive feedback for the transverse mode oscillation, further bending the soliton until breaking the soliton into vortex rings or vortices depending on the dimensionality of the system.

In three dimensional systems the decay product of the dark soliton is a vortex ring [55]. The timescale over which this occurs depends on the geometry and initial soliton conditions. Experimental observation of the decay to vortex rings has been achieved [23] [2]. Experimentally, the two dimensional case has been far less investigated due to the difficulty in producing a two dimensional trap.

As well as snaking instability, the inhomogeneity of the trap plays a role in the destruction of the multidimensional soliton. The Bugliobov speed of sound is not constant across the nodal plane. The speed of

sound is largest at the centre of the harmonic trap and lowest at the boundaries. Imprinting a dark soliton of a fixed depth, where fixed means a constant phase factor of π is used to generate the dark soliton, on an inhomogeneous condensate in a harmonic trap, will result in a variable soliton velocity across the nodal plane. As c_s is largest in the centre, the soliton velocity will be largest at the centre as well.

Both of the above processes compete in the destruction of the high energy multidimensional dark soliton. A low energy dark soliton will only experience bending due to the density distribution.

The dimensional dynamic stability criterion for dark solitons was developed in a work by Muryshev *et al* [53]. The criterion is derived from the ratio of the Thomas-Fermi radius r to the width of the soliton L and was found that dark solitons became dynamically unstable as $r \sim L$. Numerically it was found that for a soliton of velocity v that r/L increased with a ratio of $n_0 g/\hbar\omega_{x,y,z}$. Above a critical point ξ_c (r/L close to 1), transverse instability and snaking was found [53]. The most stringent stability criterion stated is for stationary solitons where the soliton is stable in that dimension if $\xi_c < 2.5$. The stability values for each dimension for this condensate are $\xi_x = 1.52, \xi_y = 9.55, \xi_z = 76.4$. Solitons generated in this experiment are therefore stable in only the confined dimension whilst unstable in the other two dimensions. It is thus reasonable to consider that the decay dynamics of the solitons generated in this experiment are two dimensional.

4.3 Phase Imprinting Method of Soliton Generation

The primary method for soliton generation used in this work was the phase imprinting method. This technique produces the dark soliton by engineering the phase of the condensate to match the phase distribution of the dark soliton. The phase of the condensate ϕ is addressed through application of a dipole potential U_{dip}. This potential is exposed to the condensate for a period τ_{pulse}. In the regime where the pulse is very short compared to the characteristic timescale of the condensate ($\approx \mu s$) and the potential is far greater than the other energy scales, the result is that the imprint potential results in only a phase change [25]. As the timescale of the imprint is much shorter than the wave function can react to, the majority of terms in the GPE can be neglected after the imprint resulting in [25]

$$\psi(z,t) = \exp[-i\tau_{pulse}U_{dip}/\hbar]\psi(z,0) \tag{4.6}$$

where $\psi(z,t)$ is the post-imprint wave function and $\psi(z,0)$ is the pre-imprint wave function. The exponential results in a phase factor ϕ

$$\phi = U_{dip}\tau_{pulse}/\hbar \tag{4.7}$$

The dipole potential for the Rb87 D2 transition is given from the previous generic U_{dip} with the substitution of the Rb87 values

$$U_{dip}(r) = \frac{3\pi c^2}{2\omega_0^3}\frac{\Gamma}{\Delta}I(r) \tag{4.8}$$

where $I(r)$ is the positional intensity of the light and $\Delta = |\omega_0 - \omega_l|$ is the detuning of the imprint from the D2 line [60].

To create the dark soliton phase profile, a π phase shift needs to be applied to one portion of the BEC which is achieved by applying a dipole potential.

The theoretical width of the soliton l_e is the order of the healing length of the condensate. Therefore the resolution of the optical system used to produce the phase imprint should be of the order of the healing length. From [15] a relation is given for the phase distribution that includes the resolution of imprint edge

$$\phi(z) = \frac{\delta\phi}{2}\left[1 + \tanh\left(\frac{z - z_0}{0.45 l_e}\right)\right] \tag{4.9}$$

where l_e is the width of the edge ranging from an intensity of $10\% - 90\%$ which requires the additional 0.45 factor. In this experiment phase imprint edges are measured 1.1-0.6 μm using different microscope objectives to project the potential.

4.4 Characterising Initial Solitons

This section will discuss the initial soliton structures created in the condensate and their lifetime and decay mechanisms. The experimental parameters relevant to their generation will be given and compared with simulations utilising experimentally achievable parameters.

4.4.1 Experimental Settings

The initial microscope objectives selected to imprint and image the first dark solitons in this experiment are the Mitutoyo 5X microscope objective and a 10X microscope objective. The 5X objective is used to image the SLM onto the atoms, and the 10X to image the atoms using the CCD above the glass chamber. Their selection is based on ease of use for the initial tests. The low magnification objectives have wider focal depths and are more forgiving in their position relative to the atoms as well as having a larger effective field of view. For the phase imprint, light from a Ti-Saph source is blue detuned by -9 GHz from the Rb87 D2 transition

at a measured power of 13 mW between the microscope objectives. A pulse time of 50 μs is chosen such that the imprint is much faster than the coherence time of the condensate. The coherence time is calculated to be $\simeq 350\ mu$s.

Once imprinted, the condensate is held for varying periods to allow any feature generated by the imprint to propagate through the condensate. The condensate is then released and imaged after 10 ms using absorption imaging. The purpose of releasing the imprinted condensate is to allow the condensate to expand. The size of the soliton if held in the trap is calculated to be less than a micron, below the imaging resolution of the 10X objective. Releasing the condensate freezes the position of the soliton and the subsequent cloud expansion brings the soliton to a size which is above the imaging resolution.

4.4.2 Soliton Depth

As previously mentioned, the soliton dynamic stability is related to the dimensionality of the medium it is generated in. These parameters are extracted through a fitting procedure of which an example image is presented in Figure 4.2.

In Figure 4.2, the method of the image processing to obtain parameters of the soliton is shown. The top left image shows the optical density of the cloud after a soliton has been created using the phase imprinting method. The characteristic high density wave from the phase imprint is visible in red, with the low density dark soliton in light green. The central cut of this data is where the 1D soliton is fitted in the second image. The equation used in the least-squares fit is the inverted parabola of the unperturbed condensate with the soliton embedded in it. It is given by

$$OD_{peak} - A(X - X_0)^2 \times \left(\frac{v^2}{c_s^2} + \left(1 - \frac{v^2}{c_s^2} \right) (\tanh(\kappa(X - X_{soli})))^2 \right) \tag{4.10}$$

where OD_{peak} is the maximum optical density of the parabola associated with the imaged condensate, A is a scaling term, X_0 is the central position of the condensate, v and c_s are the soliton velocity and condensate speed of sound, κ is the the term given by $\kappa = \frac{1}{\xi}\sqrt{1 - \frac{v^2}{c_s^2}}$ and X_{soli} is the central position of the soliton.

Within Figure 4.2 the fit and data are overlaid. To the left of the soliton it is possible to observe the corresponding sound wave generated during the phase imprint of the dark soliton. This high density sound wave travels in the opposite direction to the dark soliton and travels at the speed of sound whilst the dark soliton is sub-sonic by definition. As the sound wave and soliton move in opposite longitudinal directions it is not necessary for the fit to include the sound wave.

The depth of the dark soliton as a result of the fitting of the above equation is presented below in

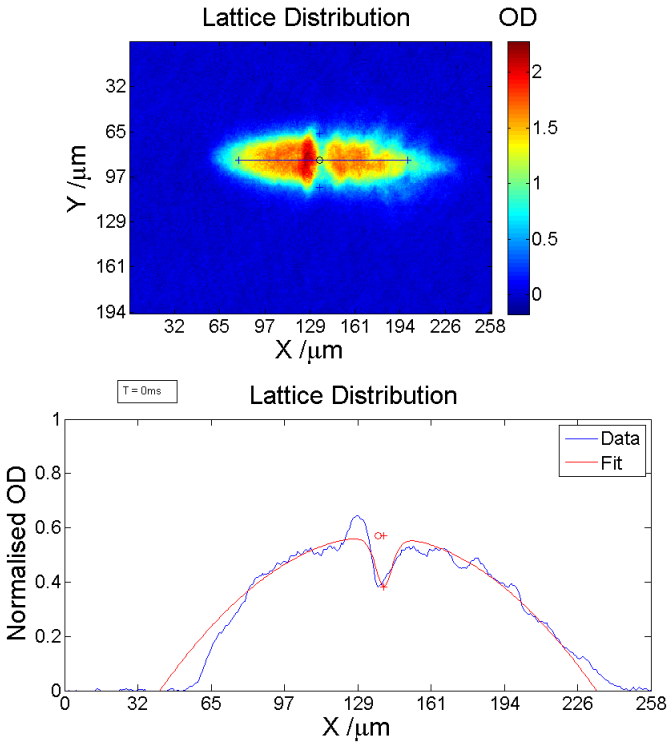

Figure 4.2: Example of the soliton fitting used for data presented. Top image is of optical density displaying a soliton imprinted in a BEC. The normalised central row of the BEC is displayed in the second image with fitting of filtered and unfiltered data.

Figure 4.3 as it propagates through the condensate. The lifetime of the soliton created in this experimental configuration was found to be 7.6 ± 0.6 ms.

The initial peak depth of the soliton is less than 40% of the unperturbed condensate. This small initial depth has an impact on the measured lifetime of the soliton. The soliton velocity, in units of the speed of sound, is given by $\sqrt{1-\frac{n_s}{n_0}}$ which for a depth of 35% gives a calculated soliton velocity of 0.8 c_s. Once the depth of the soliton reaches the 10% regime, it becomes difficult to differentiate the soliton from density fluctuations in the condensate.

In order to establish if the soliton is accelerating, the position of the soliton centre was plotted as a function of the evolution time.

The average position of the soliton centre presented in Figure 4.4 shows little deviation from a linear increase. The difference in velocity between a soliton with a depth of 35% and 12% is only 0.13 c_s. This amount of acceleration is not visible in the position due to the size of positional errors. A linear fit of the

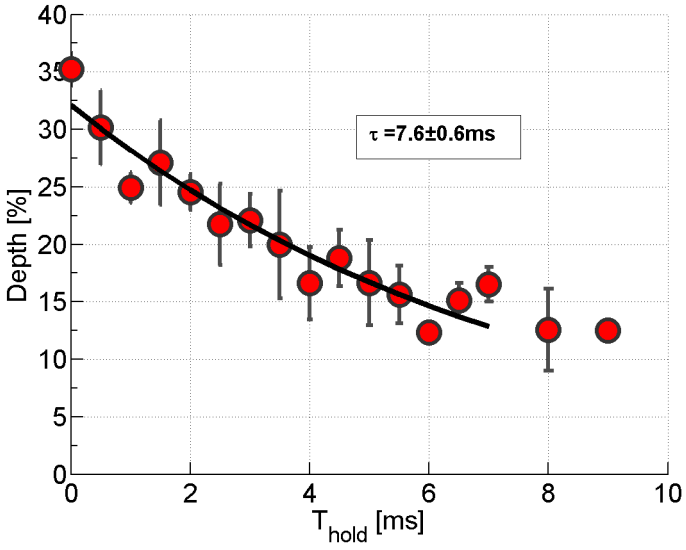

Figure 4.3: Depth of a dark soliton produced with blue detuning as it propagates through the condensate. Each point is the fitted depth of the soliton averaged from 5 images.

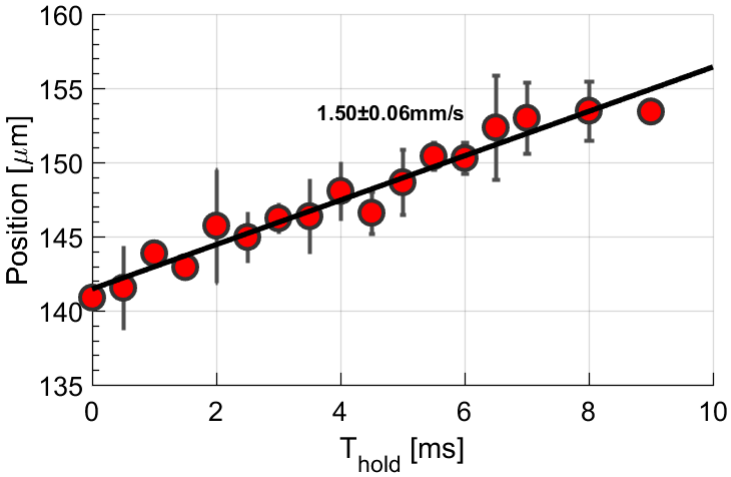

Figure 4.4: Position of the soliton centre, produced with blue detuning, in the condensate. The velocity is taken from a linear fit as the change in velocity is calculated to be 13% given the change in depth over the soliton evolution.

position is used to give an overall velocity of the soliton of 1.50 ± 0.06 mms^{-1}. The velocity of the sound wave moving in the opposite direction is observed as 1.83 ± 0.08 mms^{-1}, indicating that the dark soliton classification is valid. The sound wave can be identified as the high optical density pulse to the left of the soliton in Figure 4.2.

In order to verify the dark soliton being observed is in fact a soliton and not a simple density defect caused by illuminating the condensate, the same portion of condensate was illuminated but the detuning of the light was inverted to be 9GHz red of the D2 line. This change from -9 GHz to +9 GHz results in a sign change for Δ which inverts the sign of the dipole potential which in turn inverts the phase. The phase change is the same magnitude so a dark soliton is still generated, just with the opposite direction of travel. The expected result of this detuning change is that the direction of the atomic flow from the phase imprint will be reversed, generating the same soliton as in Figure 4.3 but moving with an opposite velocity.

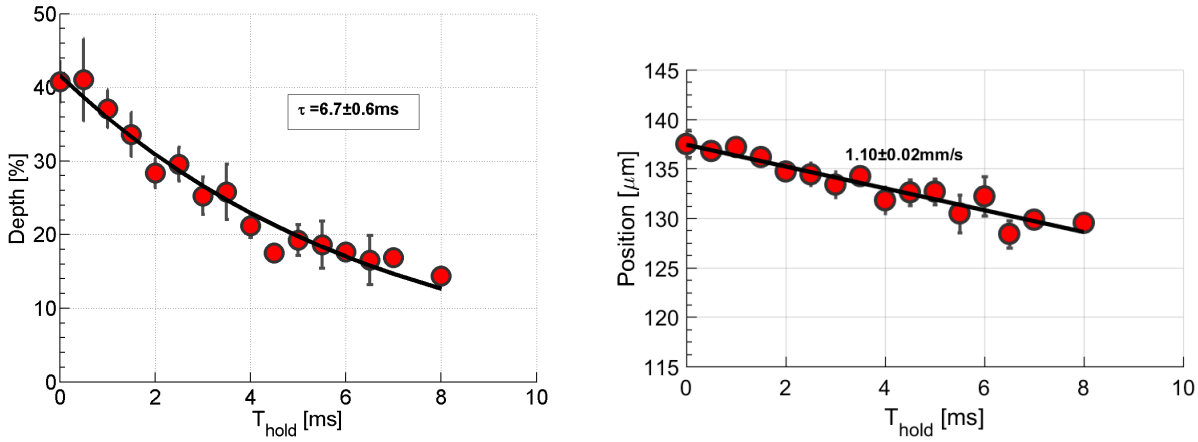

(a) Central Soliton Depth

(b) Central Soliton Position

Figure 4.5: Position and depth of soliton generated with 9 GHz red detuned light showing that the detuning determines the direction in which the soliton propagates if the same side of the condensate is illuminated.

The depth of the soliton after generation is within 5% of the blue detuned data and demonstrates a lifetime of 6.9 ms until reaching the imaging limit of 10% depth. As expected, the the soliton centre moves in the opposite direction through the condensate, despite the light being applied to the same half of the condensate. This change in soliton direction verifies the expected dynamics when alternating the sign of the phase gradient applied to the condensate. The velocity is once again determined by a linear fit as 1.10 $\pm$0.02 mms^{-1}. The difference between the the two velocities is likely due to variation in the resolved edge at the atomic plane. The microscopes are designed to work closer to the visible spectrum. There is a verified worsening in imaging quality as the wavelength of light increases from 780.260 nm which could result in a different edge resolution for the phase imprints.

The short lifetimes of 7.6 $\pm$ 0.6 ms and 6.7 $\pm$ 0.6 ms of the soliton could be the result of several factors. The trapping frequencies of the condensate are 250 Hz, 40 Hz and 5 Hz which classifies the condensate as a highly compressed 3D condensate. In the literature, lifetimes of the order of milliseconds have been observed

in three-dimensional condensates [23]. However, the decay to vortex rings was observed in that experiment. In this experimental set-up, neither detuning was successful in generating a soliton with enough energy to dynamically decay. This work differs from that of Denschlag *et al* through use of the SLM to generate the phase imprint as well as a non-cylindrical condensate.

4.4.3 Change in Optical Objectives

In order to investigate the dynamic instability a sharper image of the SLM onto the condensate is achieved by exchanging microscope objectives to the 20X. Both the SLM and CCD objectives were fitted with 20X objectives. The increase in resolution from the technical data sheet, is a factor of 2 from the 5X to the 20X. The increase in magnification also increases the intensity of the imprint used to generate the soliton, so to maintain the same π phase imprint. The power of the imprint is lowered by a factor of 16 to 0.82 mW in the science cell. By imaging the SLM at the atomic plane, it is possible to verify size of the edge being used to generate the soliton.

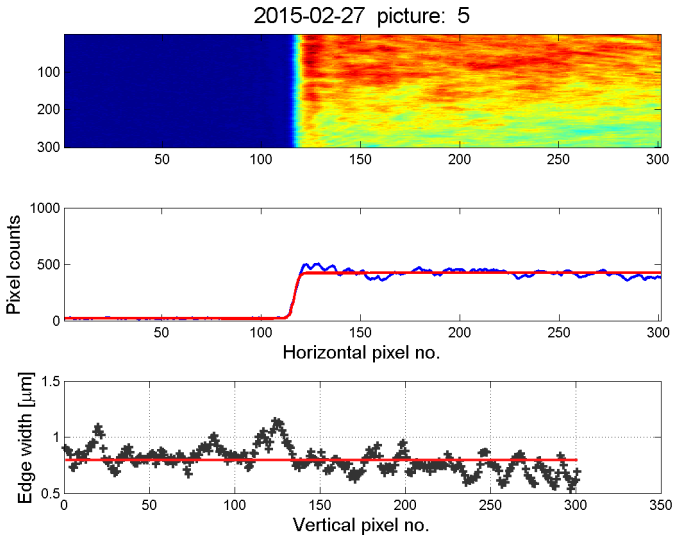

Figure 4.6: Analysis of the SLM imprint edge with the 20X objectives used. The first plot is the image region being investigated. The second plot is of the fitting of the edge and the final plot is of the resolution of the edge through for each row in the region of interest. The average width is found to be 0.81 μm

In Figure 4.6 the results of the change to 20X objectives are presented. The size of the edge l_e is found to be 0.8$\pm$0.3 μm. The exchange of objectives therefore generated an improvement from $l_e = 1.3\pm0.2$ μm with the 5X objective to $l_e = 0.8\pm0.3$ μm.

4.5 Soliton Generation with 20X Objectives

With the change of the microscope objectives, an investigation was undertaken as to explore what effect a sharpened phase step would have on the dynamics of the soliton. In simulation, a wider soliton has an increased resistance to breaking into vortices through snaking instability. By improving the resolution of the SLM, the size of the phase step l_e imprinted is reduced with the expectation that the soliton generated would have been narrow enough to begin exhibiting the snaking instability and dynamic decay processes that had not manifested in the previous experimental configuration.

4.5.1 20X Soliton

The first solitons produced exhibited fairly similar properties to those generated with the lower resolution imprint. The initial depth of the soliton was again found to be 45±3% despite a decrease in the initial width to 2.8 μm from a previous width of 3.5 μm. The depth and position of the soliton over a hold time of 10 ms is shown in Figure 4.7.

As previously mentioned, the depth of the soliton is related to its velocity. As the initial and maximum depth of the soliton produced with the 20X objectives is 45±3%, which is similar to the depth produced with the 5X objective, it is expected that the velocity would be similar. The velocity of the 20X soliton was found to be 1.19±0.09 mms^{-1} compared to the average 1.30±0.05 mms^{-1} of the dark soliton generated with the 5X objective.

Where the two dark solitons differ however is the lifetime. The 20X soliton had a lifetime of 11.9±0.5 ms which is nearly double that of the 5X soliton at 6.7±0.6 ms.

4.5.2 Diffusion of the Soliton

The dark solitons created with the 0.8 μm phase imprint did not decay through the dynamic instability process as the production of vortices was not observed. The dark solitons lost depth during the evolution time, which indicates a reduction in the soliton energy. The process which removed the energy from the condensate is expected to be through the scattering of the soliton with the thermal fraction of uncondensed atoms. In work by Fedichev *et al* [28], a study on the dissipation of kink-states, otherwise known as grey solitons, was performed.

Two regimes emerge for the diffusion time τ_D of the kink-state which depend on the temperature T. For a condensate where $k_BT \ll \mu$, the kink-state will scatter primarily with excitations of energy k_BT. This

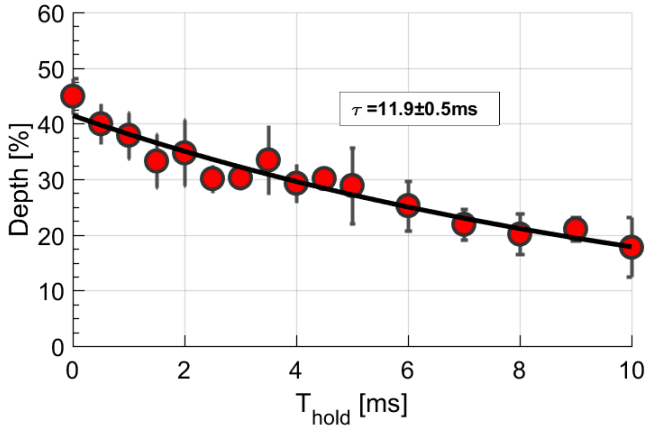

(a) Central Soliton Depth

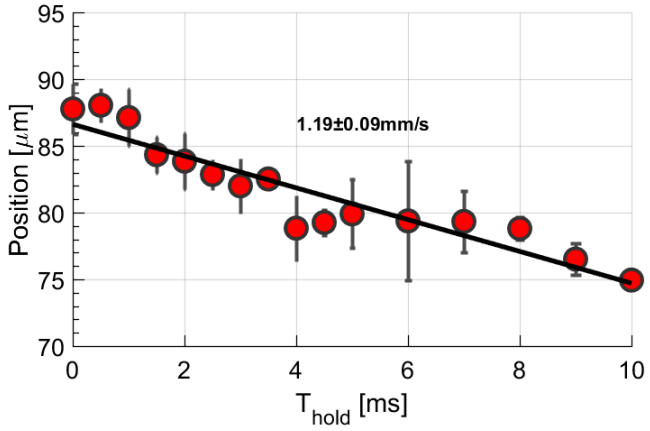

(b) Central Soliton Position

Figure 4.7: Position and depth of soliton generated with 9 GHz red detuned light through 20X objectives.

produces a diffusion time given by

$$\tau_D^{-1} = 24 * \zeta(4)\omega_\perp(\pi n_0 a^3)^{\frac{1}{2}} \left(\frac{T}{\mu}\right)^4 \tag{4.11}$$

where $\zeta(4) \approx 1.08$. In the opposite case where $k_B T \gg \mu$, the diffusion time is reduced to

$$\tau_D^{-1} = \omega_\perp(n_0 a^3)^{\frac{1}{2}} \left(\frac{T}{\mu}\right) \tag{4.12}$$

The energy of the thermal fraction is calculated to be $E_T = k_B T = k_B 36nK = 5 \times 10^{-31} J$ with a chemical

potential of $\mu = 2.5 \times 10^{-31}$. The diffusion times for each regime are therefore

$$\tau_D = \left(24 * \zeta(4) \omega_\perp (\pi n_0 a^3)^{\frac{1}{2}} \left(\frac{T}{\mu} \right)^4 \right)^{-1} \approx 0.14ms \tag{4.13}$$

$$\tau_D = \left(\omega_\perp (n_0 a^3)^{\frac{1}{2}} \left(\frac{T}{\mu} \right) \right)^{-1} \approx 55ms \tag{4.14}$$

The relation between the soliton lifetime τ and the diffusion time τ_D is given by $\tau_D \sim 5\tau$ as the lifetime value is the time taken for the soliton depth to decrease to $1/e$. Comparing the diffusion times for the two regimes it is believed that the condensate is in the regime where $k_B T \gg \mu$ as $5 \times \tau = 5 \times 13$ ms $= 65$ ms. This is an order of magnitude larger than the diffusion time for the $k_B T \ll \mu$ case,

4.6 Vortex Decay of Soliton

The dynamic decay of solitons was observed when the objectives were exchanged. With the 50X objectives it was possible to achieve a measured resolution of 600 nm. This imaging resolution is a factor of 2 larger than the healing length of the condensate. This level of resolution for both the SLM and the CCD made the following images the highest resolution images taken from the experiment. Once again the power used for imaging and imprinting was reduced in order reduce the intensity in the atom plane. Also the length of flash used for the absorption image was shortened from 50 μs to 20 μs as it allowed for an increase in imaging power which generated images with the highest optical density and sharpest features. With longer exposure, the atoms can scatter multiple times and move as they scatter. The natural line width of the imaging transition is 6.6 MHz, so an atom could scatter upwards of 40 times in 50 μs. The increase in momentum during the imaging can blur the detail of the ground state. The shorter imaging pulses were found to improve the resolved detail with the 50X objectives.

Single images of the soliton created with both the 50X and 20X objectives are displayed in Figure 4.9 at a range of hold times, from 0 ms to 10 ms. It is important to note that the 20X data is taken at 10 ms time-of-flight and the 50X data at 5 ms time-of-flight. The difference in expansion time between these images is the reason the condensates appear to have different trapping ratios in Figure 4.9.

In Figure 4.9 the difference in evolution between the soliton generated with the 20X objective and the 50X objective is clear. In the 50X objective images, by 5 ms the soliton has already split into a pair of vortices at the boundary of the condensate. With the soliton generated by the 20X, this splitting was not observed and the soliton grows in width and diminishes in depth. The high energy soliton created with the 0.60 $\pm$ 0.15

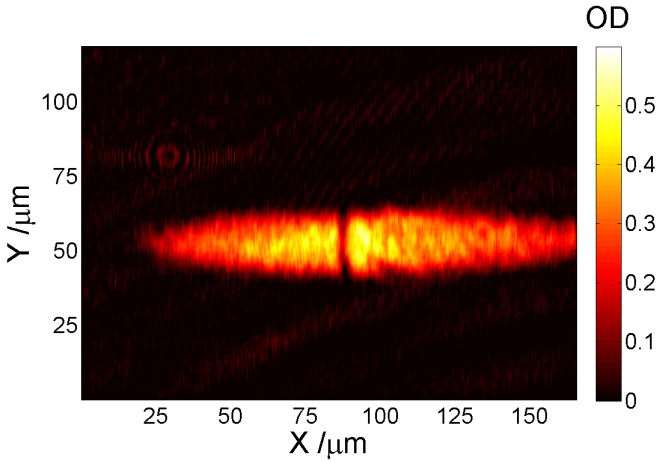

Figure 4.8: Example image of soliton through 50X microscope objectives after 5 ms time-of-flight. The field of view is such that the condensate fills the whole CCD chip. This corresponds to a distance of 180 μm by 140 μm

μm phase step is able to induce snaking instability. This in turn created the pair of vortices which propagate along the boundary of the condensate for 100 ms.

To investigate how the evolution is different between the two cases, it is worth looking at the depth and position of the centre of the nodal plane and comparing it to that of the solitons generated with the lower resolution objectives.

In the first 10 ms the central depth of the soliton evolves from a peak depth of 80%, down to less than 20% in 5.1 ms. The rapid decrease of the central contrast of the dark soliton did not occur with lower energy solitons. The lower energy solitons created with the reduced optical resolution failed to produce vortices.

The depth of the soliton plane closer to the boundary behaves differently to the soliton plane at the centre. As the vortices develop at the boundaries of the condensate, at the edges of the dark soliton, the measured depth of the feature at these points will not reduce as the vortices are generated in place of the dark soliton as snake instability breaks apart the planar soliton. The evolution of the depth n_s/n_0 at the boundary region begins with the same depth as at the centre of the condensate, but as the snaking instabilities bend the dark soliton and create phase winding, vortices develop. The depth of these vortices remain constant and high until reaching the end of the condensate. The vortices are protected against the thermal interaction and density fluctuations as they have a smaller extent as well as having to preserve a topological charge. The depth of the soliton and subsequent vortices over the first 10 ms at a distance of $\pm 6\mu$m from the semi-confined

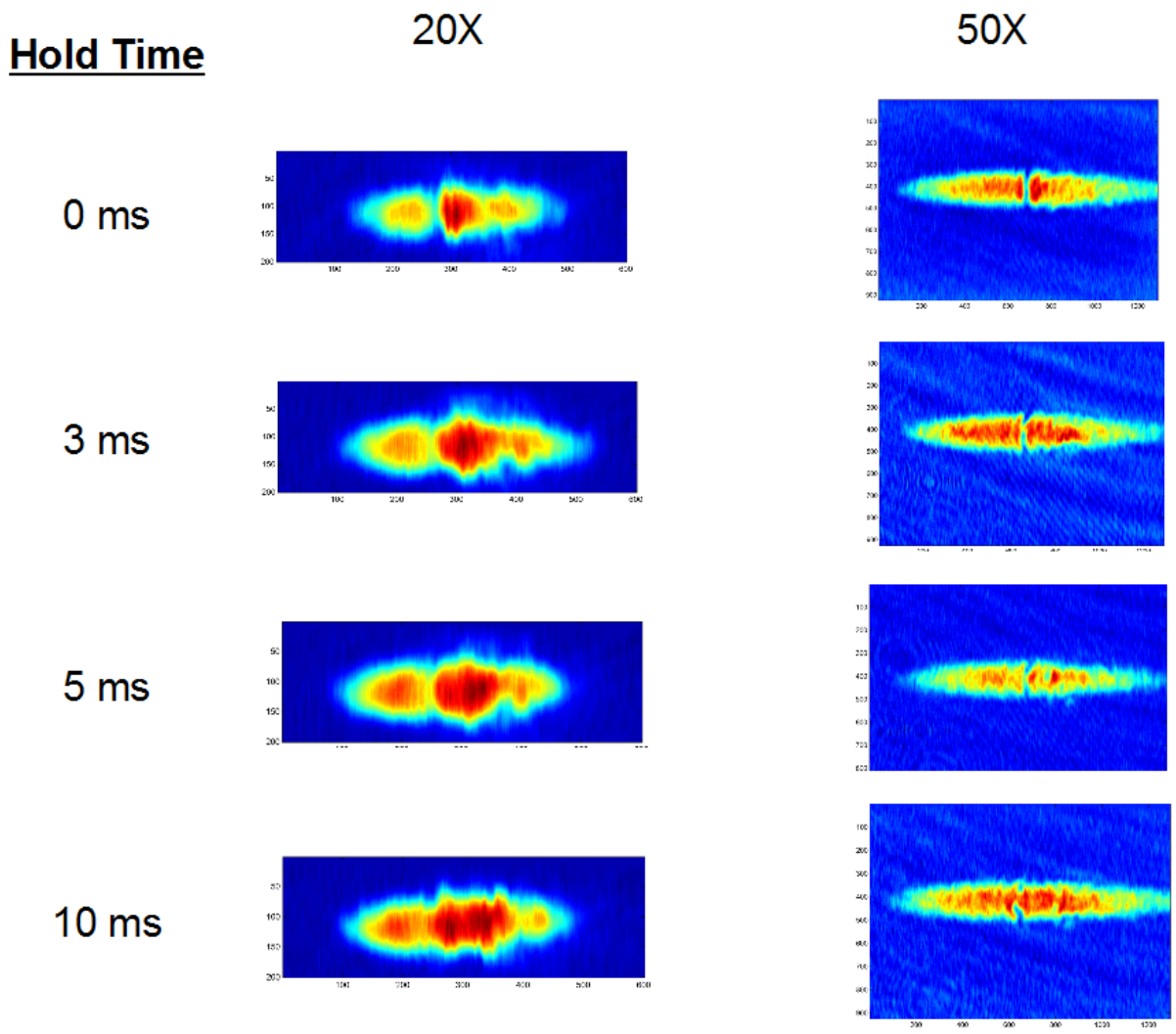

Figure 4.9: Typical images of solitons generated with the 20x and 50X objectives at a selection of hold times ranging from 0 to 10 ms. The difference in evolution is clear in that small vortices form in the 50X case after 5 ms, however this does not occur in the 20X case. The decay product of the dark soliton is expected to be a pair of vortices either side of the condensate centre but an interferometric measurement would be required to examine the phase for confirmation of vortices.

axis centre is presented in Figure 4.12.

The decay of the depth at the boundaries is found to be 23 ms and 58 ms. This is at least a factor of 5 longer than the decay at the centre of the dark soliton. The variation in decay time of the soliton from the centre to the edge indicates a different decay result at the two positions. This is due to the formation of the vortices such as those in Figure 4.9 through snaking instability at the outer boundary of the dark soliton. These vortices are topologically stable and maintain their depth, unlike the planar soliton that spawned

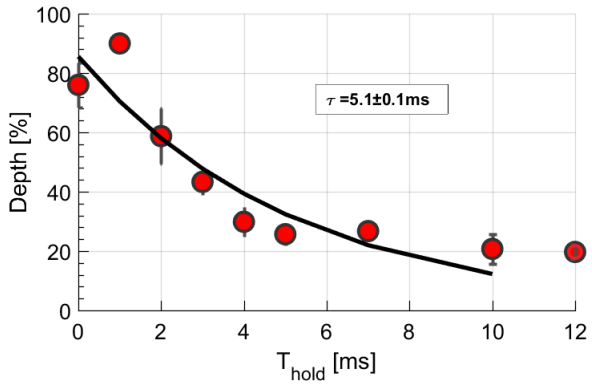

(a) Central Soliton Depth

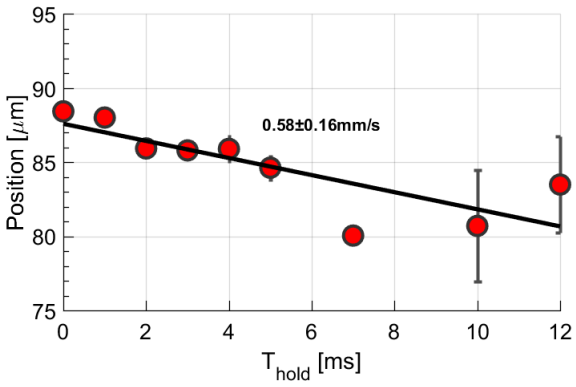

(b) Central Soliton Position

Figure 4.10: Position and depth of soliton generated with 9 GHz red detuned light through 50X objectives.

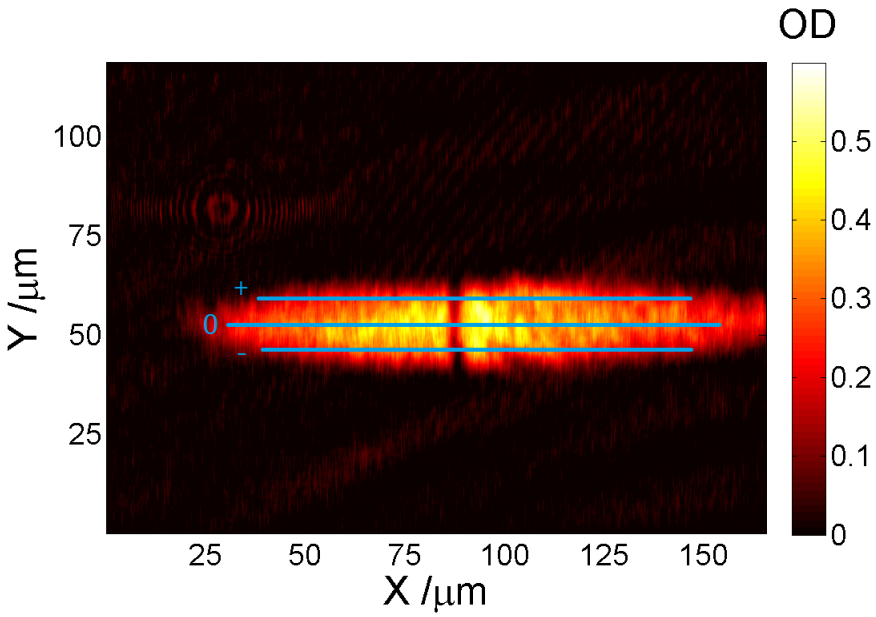

Figure 4.11: Display of sections of where fitting occurs in order to establish how the soliton evolves at the centre and ±6 μm either side of the centre

them.

The depth of the soliton and subsequent vortices has been plotted over the full range of 100 ms in Figure 4.13.

The high average depth of the vortex over a hold time of 100 ms is very different to the thermal dissipation

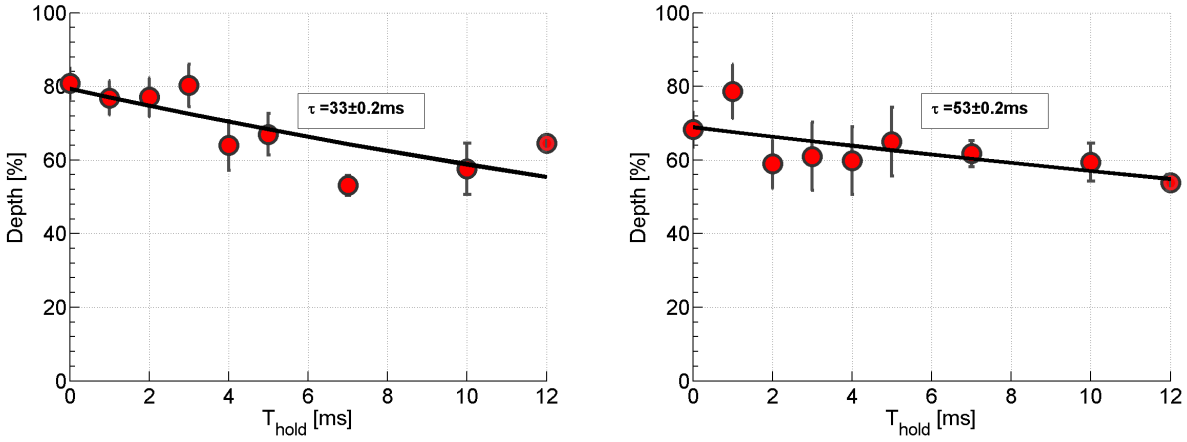

(a) Upper Boundary Soliton Depth

(b) Lower Boundary Soliton Depth

Figure 4.12: Depth of soliton and vortices generated with 9 GHz red detuned light through 50X objectives 6 μm either side of the axial centre of the condensate.

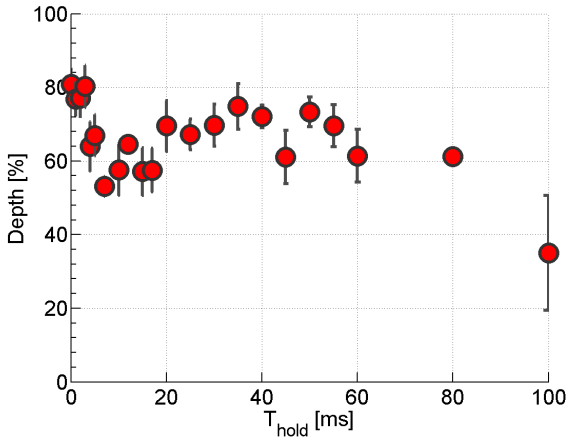

Figure 4.13: The depth of the soliton and subsequent vortex generated from snaking instability. The initial depth is high but decays quickly until the vortex is formed. From this point the vortex propagates along the condensate boundary until at 100 ms it becomes chaotic in position due to it reaching the end of the condensate.

and widening of the soliton generated by the lower resolution objectives. This dynamic decay to a pair of vortices is the expected result of a dark soliton propagating in an an-isotropic medium with two dimensional dynamics. The dynamic decay of a dark soliton in three dimensions has yielded the generation of vortex rings, however if one of the dimensions is confined heavily but not enough to reach 2D, the condensate is unable to support a ring and line vortices are generated instead.

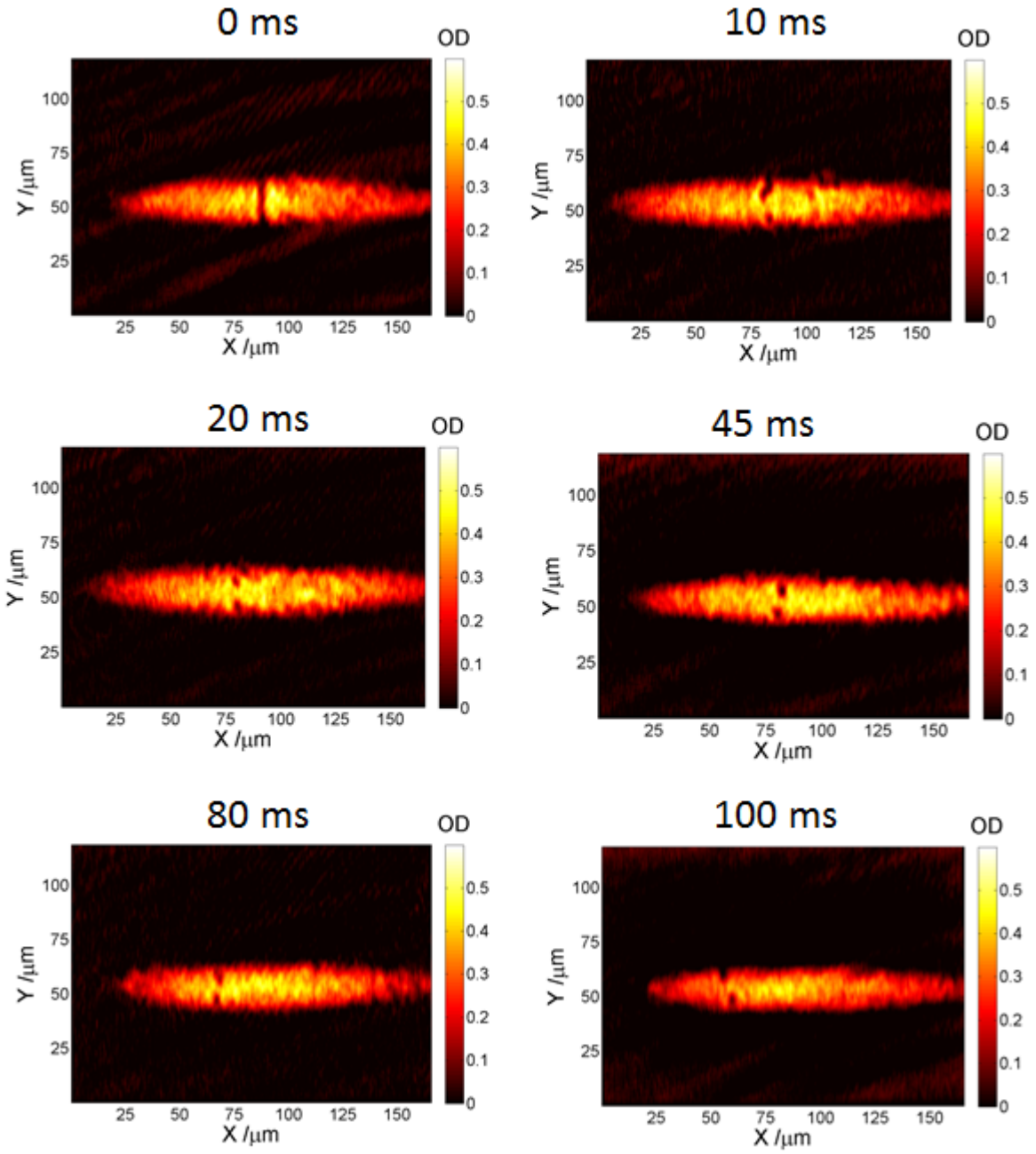

Figure 4.14: Experimental density distribution after a range of evolution times demonstrating the generation of line vortices through the dynamic decay of an imprint dark soliton.

4.6.1 Soliton and Vortex Velocity

The soliton is present as a single nodal plane until 10 ms at which point the vortices at the boundary have formed with the central portion of the soliton plane filled. The position of the soliton node is shown in Figure 4.10b and is found to have a velocity of 0.58 $\pm$0.16 mms^{-1}. This is half the velocity of the soliton generated with the lower resolution 20X objective. Despite this comparatively low initial velocity of the nodal centre, the velocity of the two vortices which are formed after 10 ms mark are found to move at similar velocities of 0.14$\pm$0.07 and 0.13$\pm$0.09 mms^{-1}. The position of the soliton and the vortex cores once they are formed is shown in Figure 4.15.

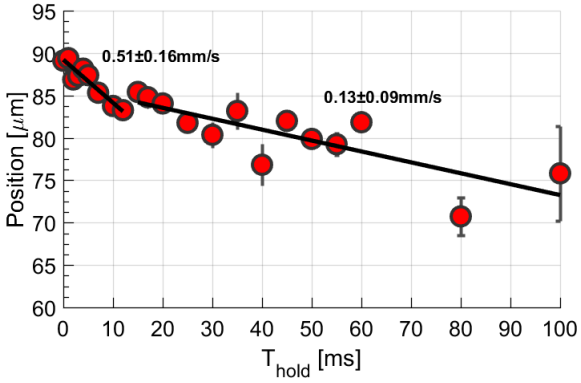

(a) Upper Boundary Soliton/Vortex Position

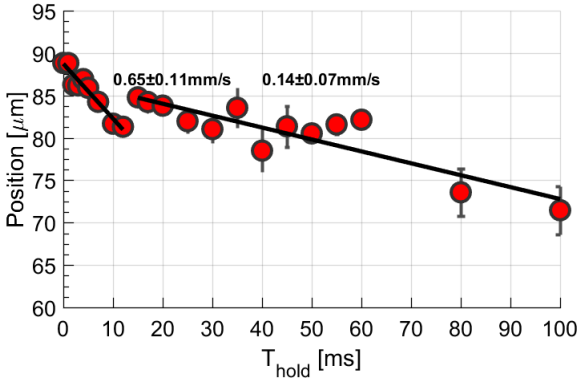

(b) Lower Boundary Soliton/Vortex Position

Figure 4.15: Position of soliton and subsequent vortices generated with 9 GHz red detuned light through 50X objectives 5 μm either side of the axial centre of the condensate. The velocity fit is performed in two sections. A fit of the initial soliton and the fitting of the vortices created.

As both vortices are generated by the same dark soliton, and the system is symmetric about the propagation axis, it is reasonable that both vortex cores should have similar velocities and mirror their positions until some difference in the conditions is experienced by each vortex. After an evolution time greater than 100 ms the vortices have travelled to the end of the condensate and their position around this region becomes chaotic and it is no longer meaningful to track them.

4.6.2 Soliton and Vortex Width

The width of a soliton and the radius of a vortex is given by the characteristic length scale of the system they are generated in. In the case of a BEC this length scale is the healing length. For a condensate of number of 40,000 atoms, with the measured trapping frequencies $\omega_x = 2\pi \times 250$Hz, $\omega_y = 2\pi \times 30$Hz and $\omega_z = 2\pi \times 5$Hz, the healing length at the centre of the condensate is calculated to be $\xi = \sqrt{8\pi n_0 a} = 0.4$ μm. This sets the

width of a soliton and the diameter of a vortex to be 2ξ =0.8 μm whilst it is held in the trap. This is below the resolution limit of the imaging set-up however, so in order to resolve the features the atom cloud is released. The expansion of the atom cloud is mediated first due to the repulsive mean field interaction of the condensate. The mean-field interactions fall away very quickly giving way to ballistic expansion. The expansion of a vortex core during time-of-flight in a BEC has been examined both experimentally and theoretically [47][17]. The expansion of the vortex core during the time-of-flight should be at least the same as the rate of expansion of the transverse size of the condensate. The expansion of the transverse size of the condensate after 5 ms time-of-flight was found to be 50%. The radius of the vortices generated by the snaking instabilities were found to have a radius of 1 μm after the 5 ms time-of-flight. Factoring in the expansion of the transverse axis, in the trap the vortex has a radius of 0.5 μm. The discrepancy between the radius of the vortex and the central healing length may be due to the formation of the vortex away from the centre of the condensate. As the vortices are generated at the boundary of the condensate by the dark soliton, the region of density in which the vortex is formed is lower. The healing length at a region of the condensate where the number-density is half that of the centre is 41% larger. This density correction extends the calculated healing length to 0.564 μm.

The radial size of the vortices generated by the snaking instability do not change in size over the propagation through the condensate. If the holes generated by the dynamic decay of the soliton were simply density fluctuations with no phase structure, then the holes would be filled in on a timescale equal to the speed of sound in the condensate. The speed of sound in the condensate is calculated to be 1.21 mms^{-1}. If the hole were a simple density fluctuation without form stability, it would take of the order of 1 ms for the surrounding condensate atoms to redistribute back to the ground state configuration. As the hole persists for two orders of magnitude longer than this it is reasonable to consider the hole as a vortex.

Figure 4.16 is taken from the same data presented in Figure 4.13 and is the width of the soliton and, after its formation at 10 ms, the width of the vortex at hold times up to 100 ms. The width of soliton and the width of the vortex appear to almost be identical after a 5 ms time-of-flight, at approximately 1 μm. The characteristic length scale for a dark soliton and for a vortex is the healing length of the condensate which suggests that the two features should be similar sizes. This is displayed in Figure 4.16,which shows the features have a constant size.

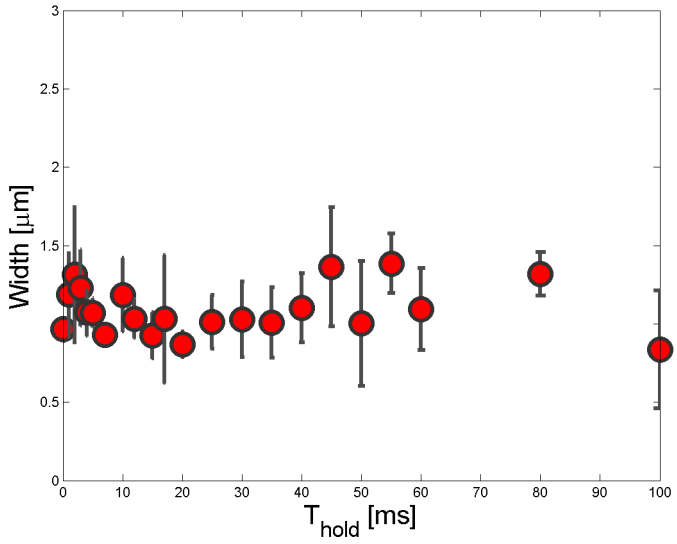

Figure 4.16: Width of the soliton and the subsequent vortices generated during the dynamic decay. Comparing the width at early hold times (0-10 ms) where the soliton is still the dominant feature, and the long hold times where the soliton node is no longer observable and vortices dominate, it is clear the two features have similar sizes $\approx 1\mu m$

4.7 Simulation of Solitons

In order to develop a better understanding of the expected results of soliton imprinting, simulations of the condensate and imprint are performed. The theoretical machinery used to simulate the experimental condensate is called "GPELab" which is a freely available toolbox for MatLab [4]. GPELab neglects temperature effects, including the presence of a thermal fraction surrounding and interacting with the condensate. This toolbox does not have the functionality currently to include a thermal fraction to the simulations. The simulations will therefore require some consideration when comparing with experimental results.

The sequence of simulation first begins with generating the ground state of the condensate. The key parameters of the condensate are supplied to GPELab, such as number of atoms and trapping frequencies, and the ground state is calculated. The experimental parameters and values relevant to the simulation of the ground state are presented in Table 4.1.

The calculated ground state of the condensate, which is held in the trap, is shown in Figure 4.17:

Once the ground state has been calculated, a phase step is applied to the ground state in order to generate the dark soliton. Much like the experiment, this is done by applying a spatial π phase factor to half of the

Parameter	Value	Comments
Atom Number	4×10^4	Measured from time-of-flight images using bimodal fitting process.
Trap Frequencies: ω_x,ω_y,ω_z	2π.(250,40,5) Hz,	Measured both by parametric heating and direct observation of in the trap oscillation.
Simulation Size: N_x,N_y,N_z	2^3,2^5,2^9	The size has been selected for speed of simulation whilst ensuring the healing length is accommodated in all dimensions.

Table 4.1: Summary of the parameters used in simulation of the condensate ground state using MatLab toolbox GPELab

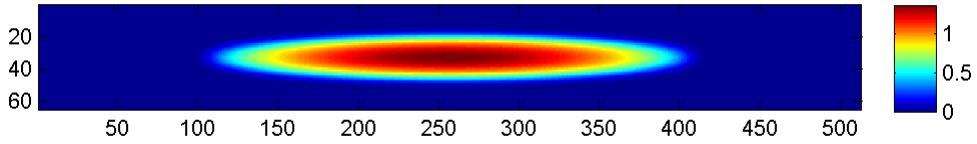

Figure 4.17: Density distribution of the simulated condensate in the trap. Using this wave function as the start point, solitons and their decay are simulated.

condensate described by

$$0.5 * Phase.dphase * (1 + tanh((Geometry3D.X - Phase.X0hat)./Phase.lehat)) \tag{4.15}$$

where $Phase.dphase$ is the amplitude of the phase difference being applied e.g. π, $Geometry3D.X$ is the simulated space of the condensate, $Phase.X0hat$ represents any offset from the centre of the condensate along the weak Z axis and $Phase.lehat$ sets the width of the gradient. The width of the gradient was initially limited to values achievable by the experiment with the variety of optical objectives from a minimum resolution of 600 nm upwards to 3 μm.

Once imprinted, the ground state is evolved in units of 0.5 ms. This time step size is reasonable for watching the formation and following propagation of the dark soliton and the subsequent vortex pair. Finer time step sequences were investigated but yielded no difference in result and took more time to compute.

4.7.1 Vortex Decay Path

In the simulation of the experimental condensate, the decay of the imprinted dark soliton to a pair of low density vortices readily occurred. Matching the size of the phase step with the experimental resolution of

0.60 ± 0.15 μm achieved by the 50X objectives produced the simulated density profiles in Figure 4.19.

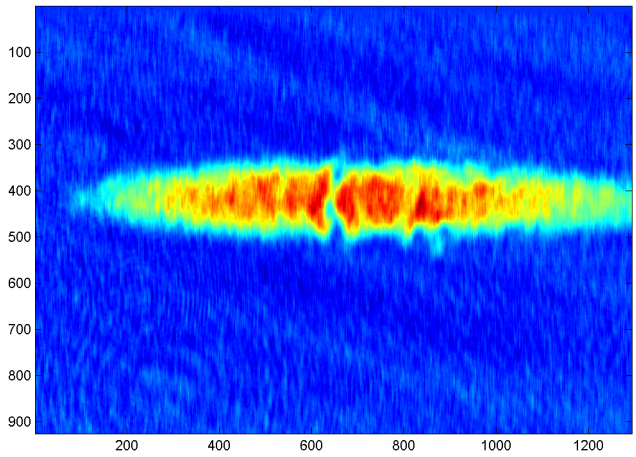

Figure 4.18: Density distribution after 10 ms evolution of an imprinted dark soliton through 50X microscope objectives and 5 ms time-of-flight. The decay of the dark soliton through snaking instability has begun to develop a pair of line vortices.

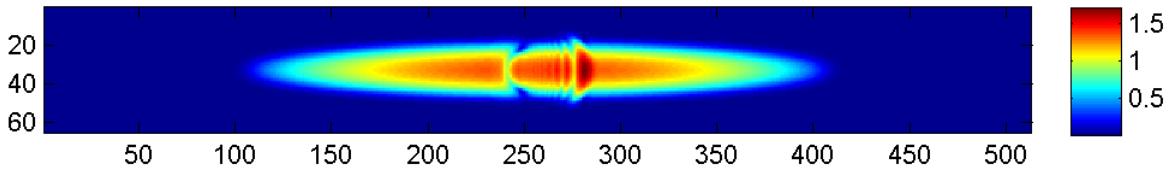

Figure 4.19: Density distribution of simulated condensate after 10 ms evolution of a dark soliton imprinted. The formation of the holes at the boundary is clear as well as the sound wave from the imprint propagating forwards.

By a time of 10 ms, it appears that the snaking instability has bent the dark soliton plane, generating the vortices at the boundary. This simulation timescale matches that of the dark soliton decay observed in the experimental data produced by the 50X objectives. An example of experimental data taken at the same 10 ms evolution time is displayed in Figure 4.18. It displays good agreement with the simulation.

By subtracting the unperturbed ground state from the evolved dynamic simulation it is possible to examine the distribution of atoms between the systems. The resultant matrices represented a three dimensional volume where each voxel contains the residual difference between the evolved wavefunction and the ground

state condensate. Integrating this "difference" matrix along each axis provides a picture of the structures present in the condensate.

Integrating the simulation results through the confined axis of the condensate illustrates that the decay product of the dark soliton is a vortex line. The density distribution of a vortex ring and a pair of line vortices appear the same when imaging from above the confined axis. In order to identify which of the decay products are produced in the dark soliton simulation, imaging through the weakly confined axis is performed. The results are displayed in Figure 4.20, which shows the imprinted condensate relative to the ground state condensate, integrated along the weakly confined axis. The result is a heat map of where there is density variation as a result of the phase imprint. Figure 4.20a displays the initial dark soliton after phase imprinting, where blue indicates negative density difference compared to the unperturbed ground state of the condensate. After 10 ms of evolution the negative density has redistributed to the boundaries of the condensate, forming the two vortex lines. They are not point vortices as they are multiple condensate healing lengths ξ in depth.

When considering whether a vortex ring is a reasonable decay product, special attention should be paid to the aspect ratio that the ring would require in order to join the pair of holes at either side of the condensate. At some point the aspect ratio between the confined axis and the semi confined axis will be too severe to support a ring structure and instead a pair of line vortices are formed.

In simulation of the experimental condensate, the diameter of the holes produced was found to be approximately 2 μm. If these holes were part of a loop, the spatial extent in the confined axis of the tightest vortex loop would be 4 μm. This is larger than the extent of the condensate in the confined axis, which makes it unreasonable for a vortex ring to be a supported decay product.

4.7.2 Non-Vortex Decay Path

In order to replicate the experimental results of dark solitons decaying away without generation of vortex products, simulations of broader phase gradients were performed. By broadening the phase edge, the depth of the soliton generated in simulation was reduced and the width of the soliton increased. This increase in width lead to a slower decay of the soliton. Attempting to match an initial depth and decay rate of the solitons generated with the 5X and 20X objective was not achievable. The issue in simulation was that the maximum depth achieved by a soliton generated with a phase edge of 1 μm was 43%. Within the simulation the healing length of the condensate is 420 nm and a true dark soliton would require the width of the phase transition to be of the order of this size. Use of 1 micron as the phase step width as for the phase imprint corresponds to a grey soliton with an intermediate depth. The threshold peak depth of solitons that were no

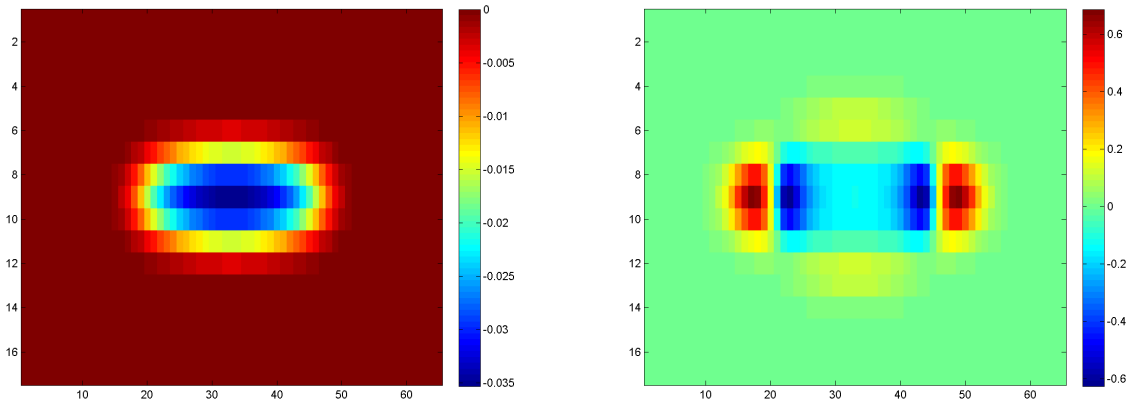

(a) Density difference at 0 ms

(b) Density difference at 10 ms

Figure 4.20: Integrated difference in density from imprinted condensate and ground state after 0 ms and 10 ms evolution. The generation of vortex lines by 10 ms is clearly demonstrated by the two negative density lines.

longer observed to decay into vortices in simulation was found to be 20%. The lifetime of solitons created in this limit were found to exceed 35 ms. Shallower dark solitons, persisted for longer and resisted snake instability for longer too.

4.7.3 Discussion of Soliton Decay Paths

Through the sharpening on the phase mask applied by the SLM, a separate decay path was accessed. The lower resolution limit, where the phase mask was imaged with a resolution of 0.81 μm, produced a soliton with a width l_e of 2.7 μm. This is an order of magnitude larger than the healing length of the condensate. The ideal initial width of soliton is of the order of the healing length. By generating a wide soliton, it imposes limits on the depth to which the soliton can reach, as well as how long the imprint requires to form the dark soliton structure. Low optical resolution results in a shallower phase gradient, which in turn stunts the dark soliton. As the soliton is created wider and shallower, the soliton dynamic decay is slowed. This slower dynamic evolution allows the density and thermal fluctuations present around the condensate to dissipate energy from the dark soliton before the dynamic decay into vortices. This is why the dynamic decay is not observed with the lower resolution.

By exchanging to the higher resolution objectives, where the soliton generated had an initial width of only 1 μm, it is possible for the soliton to form more quickly. Once the dark soliton has formed it begins a dynamic decay through interaction with the transverse modes of the trap. This manifests as the aforementioned snake

instability, which leads to the dynamic decay resulting in a counter-rotating vortex pair at the boundary of the condensate. These vortices are less susceptible to density fluctuations and thermal dissipation than the nodal plane of a dark soliton as they have a smaller extent and have to preserve their rotational charge. The vortex lines propagate around the condensate at a fixed velocity until colliding at the end of the trap.

4.8 Conclusion

This chapter has presented the experimental data of both decay through thermal dissipation as well as dynamic decay into line vortices through snake instability. These two separate regimes were accessed by varying the resolution of the phase mask used to generate the dark soliton. The lower resolution phase mask placed a lower limit on the size of soliton produced which in turn limited the maximum depth achievable. This extended the time required to reach the dynamic decay regime which meant that thermal dissipation of the dark soliton dominated the decay. Achieving a sharper phase mask decreased the soliton size and increased the maximum depth. This allowed the dark soliton to begin decaying through snake instability before thermal dissipation could prevent the formation of vortices. These vortices were observed for hold times exceeding 100 ms, over an order of magnitude longer than the solitons which succumbed to thermal dissipation. Simulations of the experimental soliton production is performed to aid investigation of the timescales and decay process. Examining cross-sections of the simulations confirm the decay of the dark solitons into line vortices which persist in the condensate boundaries.

CHAPTER 5

JONES-ROBERTS SOLITONS

This chapter will present the first experimental realisation of two dimensional Jones-Roberts solitons in a Bose-Einstein condensate. In order to justify the results presented, the theory of this family of excitations will be covered, followed by discussion of the similarities and differences compared to the standard dark solitons produced in the same experimental arrangement. The properties of the experimental Jones-Roberts solitons will be investigated as well as discussion of the uses they could serve in future experiments. Further work beyond this thesis has been done with the data published in Meyer *et al* [50].

5.1 Jones-Roberts Soliton Theory

Dark solitons and vortices are simple excitations that can be generated in a condensate, but they are not the only stable structures capable of being produced in a non-linear medium. Jones-Roberts Solitons (JRS) are a class of solitons identified in 1982 by CA Jones and PH Roberts [39]. This group of solitons was identified from numerical integration of the GPE, with Jones and Roberts recognising trends in the new class of solitons. Unlike the standard planar dark soliton discussed and presented in the earlier chapter, the JRS is a density minimum of finite extent with a different phase structure. JRS are able to exist as either a three or two dimensional object depending on the dimensionality of the medium they are created in.

5.1.1 3D Jones-Roberts Solitons

In three dimensions, the JRS density distribution manifests as either a vortex ring or as a rarefaction pulse [39][10]. A rarefaction pulse is a finite volume or area in which there is a reduced density compared to the normally unperturbed medium. The 3D JRS is capable of transitioning between the vortex ring and a rarefaction pulse. The criterion for this transition is related to the 3D JRS energy and momentum.

The 3D JRS dispersion curve is constructed from plotting the energy E and momentum p. It is found that the 3D JRS dispersion comprises of two branches which meet at a minimum momentum p_{min} and minimum energy E_{min} [39]. The lower branch of the 3D JRS dispersion curve asymptotically describes vortex rings. The energy, momentum and velocity of vortex rings are given by, respectively,[9]

$$E = \tfrac{1}{2}\rho\kappa^2 R\left(ln\tfrac{8R}{a} + L_0 - 2\right) \tag{5.1}$$

$$p = \rho\kappa\pi R^2 \tag{5.2}$$

$$v = (\kappa/4\pi R)\left(ln\tfrac{8R}{a} + L_0 - 1\right) \tag{5.3}$$

where ρ is the density of the fluid, κ is the circulation of the fluid, R is the radius of the vortex ring, a is the radius of the vortex core and L_0 is the minimum spacing. These equations only describe the 3D JRS whilst on the lower branch of the curve as $E \to \infty$ and $p \to \infty$ while $U \leq 0.6$.

As the momentum of the 3D JRS decreases, the solutions move away from the vortex ring form with the radius of the vortex ring R decreasing until a threshold momentum of p_{min} where the 3D JRS vortex ring radius $R \to 0$. At this point the vorticity of the ring is lost and the 3D JRS transitions in to a rarefaction pulse. This transition is observed to occur at 3D JRS velocity $U > 0.625c_s$ [9].

The upper branch of the 3D JRS dispersion curve manifests as rarefaction pulses which, as momentum $p \to \infty$, become larger in physical extent, shallower and unstable in the system.

The property values for a 3D JRS are presented in Table 5.1 from Jones *et al* [39].

U	E	p	m	ω
0.4	129	233	22.6	3.36
0.5	80.7	123.5	13.0	2.31
0.6	56.4	78.9	8.97	1.06
0.63	52.3	72.2	8.37	-
0.66	50.7	69.6	8.20	-
0.68	53.7	74.1	8.8	-

Table 5.1: Table of 3D JRS energy E, momentum p, dipole moment m and angular momentum ω at velocity U as listed in dimensionless units from Jones *et al* [39]. The minimum cusp at $U = 0.63$ can be picked out from the table and loss of vorticity. At velocities above $U = 0.63$ the excitation is best described as a rarefaction pulse.

The energy and momentum reference in Table 5.1 are calculated from dimensionless equations [39]

$$E = \frac{1}{2}\int_{V\infty} |\nabla\Psi|^2 dV + \frac{1}{4}\int_{V\infty} (1-|\Psi|^2)^2 dV \tag{5.4}$$

$$E = Up + \frac{1}{4}\int_{V\infty} (1-|\Psi|^2)|1-\Psi|^2 dV \tag{5.5}$$

where V is the volume the 3D JRS is generated in, U is the velocity of the 3D JRS and p is the momentum.

5.1.2 2D Jones-Roberts Soliton

The 2D JRS does not exhibit a minimum point in momentum and energy that the 3D JRS demonstrates in the dispersion curve. Instead, the momentum and energy of the 2D JRS monotonically decrease as the velocity of the 2D JRS tends to the speed of sound. A schematic of the 2D JRS dispersion curve is displayed in Figure 5.1. At high 2D JRS energy, which corresponds to a low velocity, a 2D JRS manifests as a vortex-antivortex pair. A vortex-antivortex pair has the phase distribution of two point-like 2π phase windings of opposite polarity. As the 2D JRS energy decreases, the separation of the vortex-antivortex pair decreases until the vortex cores are no longer separated. Vorticity is then lost and the 2D JRS transitions into a 2D rarefaction pulse. The phase diagram of the 2D rarefaction pulse is visualised in Figure 5.2 as a finite length phase edge with a π winding at the ends. As the 2D JRS's velocity tends to the speed of sound, the 2D JRS becomes larger in physical extent and shallower, until merging back into the condensate at the speed of sound.

The energy of the 2D JRS is related to the velocity of the JRS and is a conserved value like the standard dark soliton. The ratio of the JRS velocity to the local speed of sound determines the JRS form. In a homogeneous medium with no energy loss mechanisms this translates to a steady form for the 2D JRS.

5.1.3 2D JRS in Inhomogeneous Media

In the inhomogeneous distribution of a harmonically confined condensate, as the 2D JRS moves from a high density region in to a low density region, it is found that the 2D JRS can transition between the vortex-antivortex form and the rarefaction pulse. This transition occurs as the 2D JRS gains energy moving from a high density region to a low density region. This gain in energy can be enough to allow a 2D JRS in the rarefaction state to transition back to the higher energy vortex dipole state.

Continuing the effect of an inhomogeneous medium, the physical extent of a dark soliton extends to the boundary of the condensate and covers the full density distribution making it vulnerable to snake instabilities

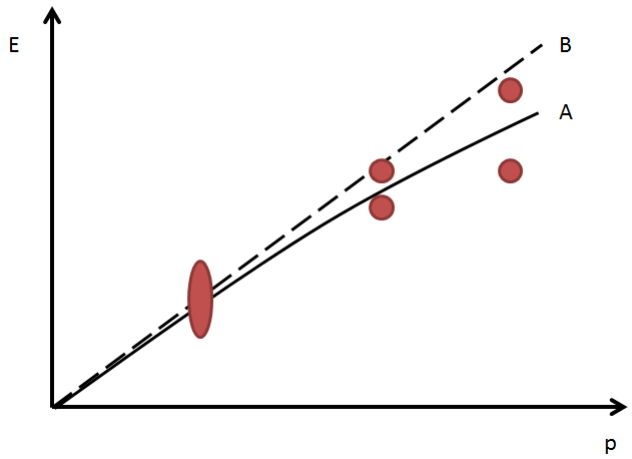

Figure 5.1: Schematic dispersion curve **A** of the 2D JRS, and phonon dispersion curve **B** based from original paper by Jones-Roberts [39]. At higher momentum-energy the JRS is a vortex-antivortex pair which merge into a rarefaction pulse at lower momentum-energy. These physical representation of these states are shown with red examples, with the pairs as vortex-antivortex and the single rarefaction pulse at low energy.

as demonstrated in the previous data. A 2D JRS is finite in extent and therefore experiences less density variation over itself. This difference in spatial extent could translate into an increased stability compared to a dark soliton produced in the same trapped system. An increased stability may make a JRS a good candidate for investigation of transport dynamics across a condensate.

The medium in which the theoretical work by Jones and Roberts was done was a homogeneous condensate. The lack of density variation results in JRS moving exclusively in a straight line at a constant velocity. If the condensate density distribution is no longer homogeneous but harmonically distributed, such as in standard dipole trapped condensates, then the 2D JRS will be refracted. In theoretical work by Smirnov *et al* [56] a quasi-soliton, of which the JRS is a type, was generated in an inhomogeneous condensate. The evolution of the implanted 2D JRS was observed and investigated. The density distribution of the condensate is found to affect the trajectory of the quasi-soliton in a way similar to geometric optics. As the JRS moves into denser regions of the condensate it experiences the smooth gradient of the density profile and the 2D JRS trajectory is curved towards the lower density region.

5.2 Production of Jones-Roberts Solitons

The phase imprinting method used for the standard dark soliton decay is utilised for the 2D JRS production. A triangular phase imprint was identified as a good candidate for 2D JRS production. In simulations the triangular imprint is found to generate motion in the condensate which culminates in a pair of stable and travelling JRS. Discussion of the simulations performed is given later in the chapter. Choosing a triangle pointing in to the centre of the condensate, it is possible to generate two 2D JRS moving in opposite directions with a single imprint. This is different to the standard dark soliton phase imprint as the phase distribution of the dark soliton is imprinted to generate it instead of using the subsequent condensate motion.

Figure 5.2: Schematic of the phase distribution for a 2D JRS

This choice of production method is experimentally easy to perform, as the SLM can generate any two dimensional mask through the image hosted on it. The experimental difficulty in generating the 2D JRS pair was in placing the imprint on the condensate precisely enough that the JRS would be generated. The shape of the triangle and the strength of the imprint was critical in producing a stable JRS to observe.

The size of the imprint is a triangle with a height of 16.1±0.1 μm and a base of 16±0.1 μm at the image plane, on the condensate. This size of triangle is of the order of semi confined axis of the condensate which makes the positioning a critical parameter in generating the 2D JRS. The size of the condensate in the semi confined axis is also an issue in that sound waves from the imprint can reflect back into the 2D JRS. This reflection issue was not present with the standard dark soliton phase imprint as the sound waves dissipate before reflection occurs. The phase imprint parameters for 2D JRS production are an imprint of 780.256 ±0.02 nm for a period of 30 μs.This is a red detuned phase imprint which is selected so that the direction of propagation is away from the imprinted section of the condensate. The aim of this direction selection is to provide the 2D JRS with as minimally perturbed medium to propagate through. The detuning of +7.88 ±

0.1 GHz corresponds to a phase imprint of π. This value of phase will be used in the simulations later in this chapter.

5.3 Characterisation of the 2D JRS

The shape and distribution of the excitations generated by the triangular imprint are important in helping classify them as JRS.

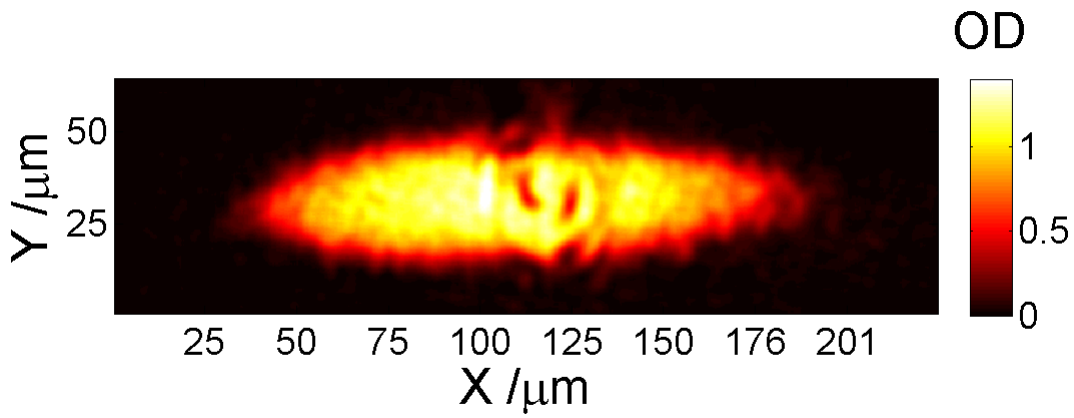

Figure 5.3: Image of a pair of JRS after a 5 ms evolution in trap and a 10 ms time-of-flight.

The excitations are found to be finite extent in all dimensions. This compact nature is different to the planar dark solitons discussed earlier as dark solitons reach across the semi-confined axis of the condensate. The finite extent in the plane of the condensate excludes it from being a standard dark soliton.

Another potential candidate for the excitations generated would be a single vortex line. The density distribution of a vortex line is circular both in trap and after expansion. The shape of the excitations generated with the triangular imprint are not circular and display an approximate 2:1 ratio. This ratio lends to the characterisation of the excitations as a bound vortex-antivortex pair or a vortex ring. The Jones-Roberts soliton can exist in these forms at high energy depending on the dimensionality. The other form available to the Jones-Roberts soliton is a rarefaction pulse.

The justification for classing the excitations produced as two dimensional is as follows. The healing length of the BEC is calculated as 420 nm whilst the Thomas-Fermi radius in the confined axis is calculated to be 1.1 μm. The size of the smallest vortex ring which could be generated would be of the order of 4ξ which is larger than the available space in the confined dimension. Although the condensate is not in the two dimensional regime, it is unable to support vortex rings which means that only two dimensional Jones-Roberts solitons

can be generated in this trap geometry.

In the high energy case, there should a large separation of the vortex cores which is not observed in experiment. This suggests that the excitations are created as rarefaction pulses or that they are on the cusp between the two forms where the optical system is unable to resolve the separation.

5.4 Experimental Evolution of the 2D JRS pair

In order to observe the evolution of the 2D JRS, the expansion and absorption imaging process is performed. Once imprinted with the triangular phase distribution, the condensate is allowed to evolve for up to 45 ms while held in trap. The condensate is released from the confining dipole potential and allowed to expand over 10 ms. As with the planar dark soliton results, releasing freezes the density distribution of the condensate and the following ballistic expansion of the condensate enlarges the 2D JRS to the resolvable size of approximately 7 μm.

Absorption images of the pair of 2D JRS evolving through the condensate are displayed in Figure 5.4.

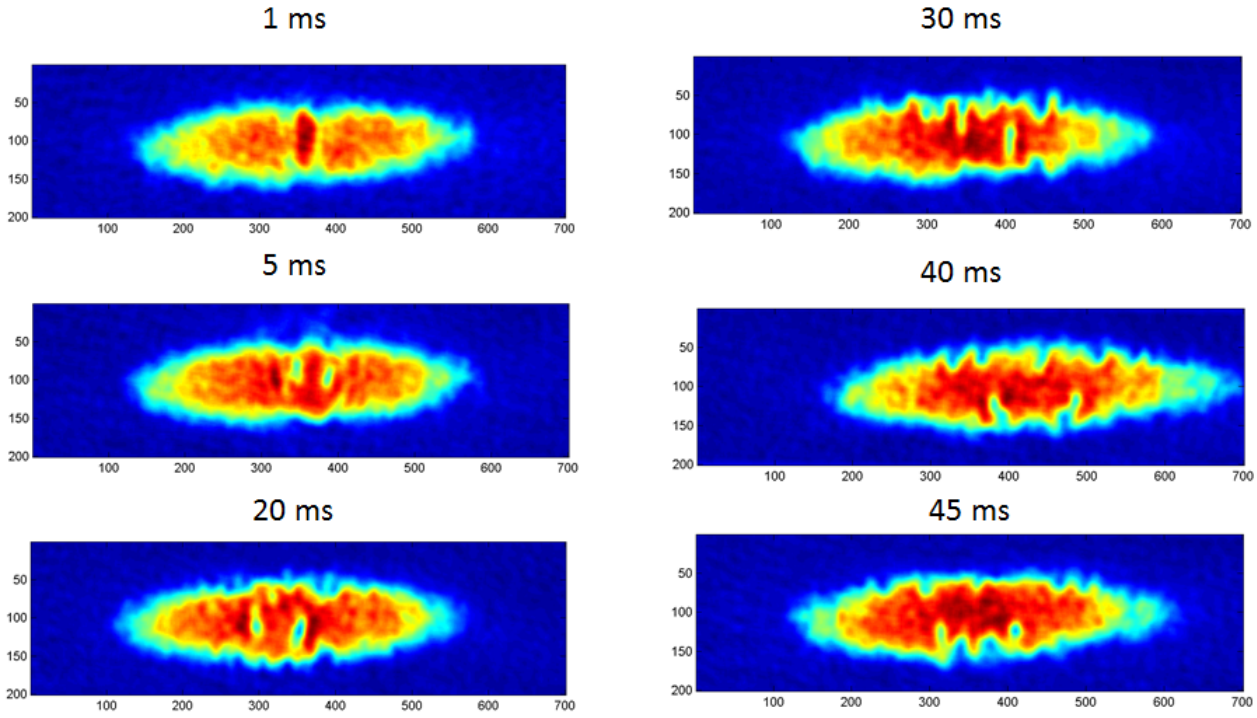

Figure 5.4: Absorption images of the condensate after a triangular phase imprint of π. At each stage of the 45 ms evolution, a clear pair of low density regions are observed as they propagate down to the condensate boundary. Data taken after 10 ms time-of-flight.

The evolution of the condensate after the triangular phase imprint is shown in Figure 5.4. The generation and subsequent motion of two 2D JRS rarefaction pulses is displayed. After 1 ms of the imprint there is little change to the condensate distribution other than an initial high density region in the area where the imprint is made. After 5 ms in the dipole trap the generation of two rarefaction pulses has occurred. These low density regions are not a single vortex as they are elliptical in shape. The major and minor axis lengths of elliptical rarefaction pulse after 5 ms evolution is found to be 13.3 $\pm$0.2 μm and 6.2 $\pm$0.3 μm. This is after 10 ms time-of-flight. The relative depth n/n_0 of the pulses is found to be 46% after 5 ms of evolution in the trap. The relative depth of the planer dark solitons generated in the previous chapter is found to be 28% after the same evolution period.

Over the next 45 ms the rarefaction pulses propagate across the semi-confined axis of the condensate until reaching the condensate boundary. At the condensate boundary the rarefaction pulses have changed in shape from an ellipse into a kidney shape. In some images at 45 ms evolution, such as in Figure 5.4, the 2D JRS has disintegrated at the boundary breaking the bent JRS structure into two separate vortices. This process is found in the simulations of quasi-solitons near condensate boundaries [56].

5.5 Depth of JRS

The excitations displayed are considered to be 2D JRS from their physical distribution in Figure 5.4 coupled with simulations of the triangular phase imprint. When considering the depth of the 2D JRS observed, it is worth recalling how the standard planar dark soliton depth behaves. The depth of a dark soliton is determined by the soliton velocity through v^2/c_s^2 where c_s is the local speed of sound. For a 2D JRS the velocity determines the energy and thus the form. This in turn determines the depth of the 2D JRS. Whilst the 2D JRS is high energy, vorticity is present and the 2D JRS comprises of the pair of vortex-antivortex, which have a zero density at the centres. Therefore $n/n_0 = 0$ until the JRS energy lowers until the 2D JRS transitions to a rarefaction pulse which becomes shallower and increases in spatial extent as the 2D JRS velocity tends to c_s.

In the experiment, the pair of 2D JRS produced have their depth monitored after a 10 ms time-of-flight expansion.

Figure 5.5 shows the average depth of the pair of 2D JRS as they propagate through the condensate. The longest period of time the JRS could propagate was found to be 45 ms. By 45 ms both the 2D JRS have crossed the semi-confined axis of the condensate; a distance of 32 μm. On reaching the boundary, the form and position of the 2D JRS becomes chaotic between experimental cycles.

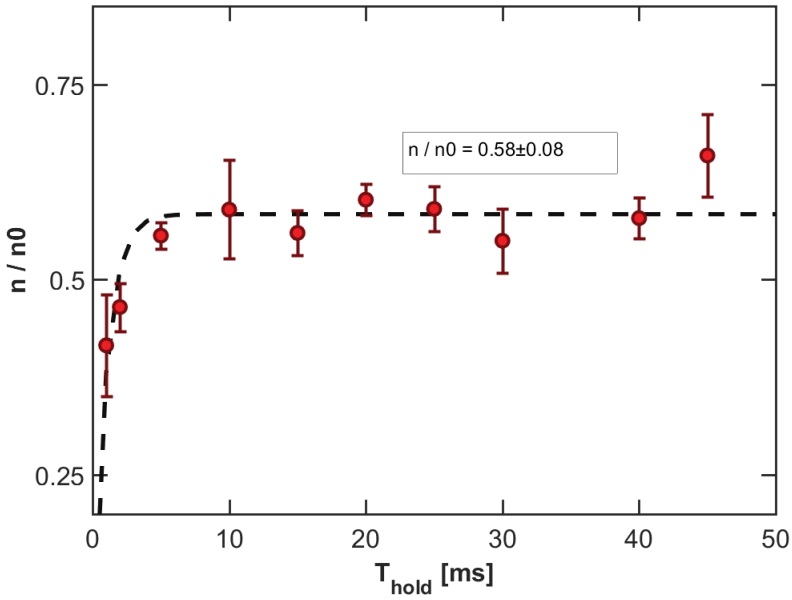

Figure 5.5: Average depth of the JRS as they propagate through the condensate. The JRS develop to their full depth of 0.58 ± 0.08 n_0 by 7 ms and persist at over 50% for 45 ms.

The results of the average 2D JRS depth is more like the long-lived vortex decay products of the dark solitons from the previous chapter than the dissipated dark soliton. Unlike the dark solitons which are found to have the highest depth at creation, the 2D JRS take an average of 7 ms to reach the peak depth of 58 ± 8 %. The 2D JRS are not directly imprinted but evolve out of the resulting motion generated by the triangular imprint.The phase imprint of the dark soliton relies on engineering the condensate phase to match the distribution of the dark soliton. The triangular imprint does not match the phase distribution of the 2D JRS but the resulting evolution results in the 2D JRS production. Once reaching the peak depth, the JRS maintain their depth until they become chaotic at the condensate boundary. Due to the stability of the 2D JRS over the total propagation time, assigning a value for the lifetime, as was done for the planar dark solitons, is not valid. Ultimately the 2D JRS are stable over the available measuring period of 45 ms. If the 2D JRS rarefaction pulse was to lose energy through dissipative processes during its propagation, then the depth would reduce and the spatial extent would increase as the form of the JRS is energy dependent [39]. This is not observed in the 2D JRS data despite the dark solitons created with the same system dissipating away over a time-scale of 12 ms. The stability of the 2D JRS compared to that of the dark solitons is believed to be due to the finite extent of the excitation. The dark soliton interacts with the boundary of the condensate and experiences the dynamic instabilities which result in the decay to vortices which is not

a decay path available to the 2D JRS. There is the added stability when in the vortex pair state due to the maintenance of the circulation around the phase windings.

5.6 Position of the 2D JRS

The position of each 2D JRS is mapped as they propagate across the imprinted condensate. This is done by extracting the centre position of the 2D JRS. The results are displayed in Figure 5.6.

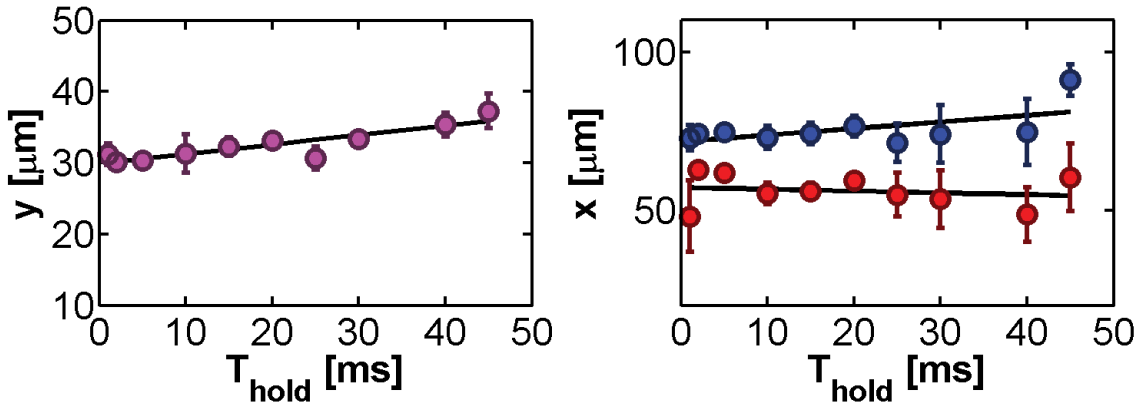

Figure 5.6: Transverse (y) and longitudinal (x) positions of the JRSs produced by the triangular imprint. Both JRS moved together in a positive transverse direction so the average of the pairs transverse position is presented.

Figure 5.6 displays the transverse (y) and longitudinal (x) position of the JRS. The red-detuned triangular imprint ensures that both 2D JRS will move away from the imprinted area. This direction manifests as a result of the phase gradient dictating direction of atomic flow, like the dark soliton case. Using a linear fit, the transverse velocity of the pair of JRS across the semi-confined axis is found to be 0.13 mms $\pm$ 0.04^{-1}. This is far below the speed of sound $c_s = 1.3$ mms^{-1} which is indicative of soliton behaviour.

The longitudinal velocity is opposite for each 2D JRS as they are produced out of the motion generated by each side of the triangle imprint. This results in a small and opposite velocity, separating the 2D JRS from each other, making them easier to distinguish. The longitudinal velocities are found to be 0.21 and -0.06 mms^{-1}. The magnitude of the velocities gives 0.25 mms^{-1} and 0.14 mms^{-1}. The difference in velocity between the two JRS is most likely down to differences in the imprint that generated them. If there was a gradient of light intensity across the triangle, it would result in a minor phase gradient which would affect the condensate motion which produces the 2D JRS and the properties once generated.

Regarding the theoretical prediction of the refraction of the JRS as it propagates through an inhomogeneous medium [56], it is not clear from the positional data if this bending of trajectory occurs. The trajectory of the 2D JRS pair takes them from the dense centre of the condensate, to the condensate boundary. This path will induce minimal curvature compared to the case discussed in [56] where the quasi-soliton is travelling almost parallel to the longitudinal axis and is refracted out from the trap centre.

5.7 Shape of JRS

The shape of the 2D JRS produced in the experiment were analysed using an ellipse fitting protocol. Through measurement of the major axis α and minor axis β of both 2D JRS produced, it is possible to quantify how the pair of 2D JRS physically varied over the course of their evolution.

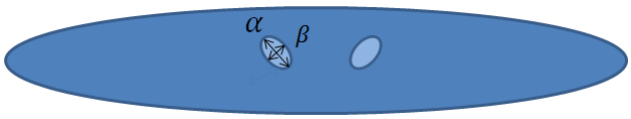

Figure 5.7: Schematic of the ellipse fitting used for analysing the variation in shape as the 2D JRS propagates through the condensate

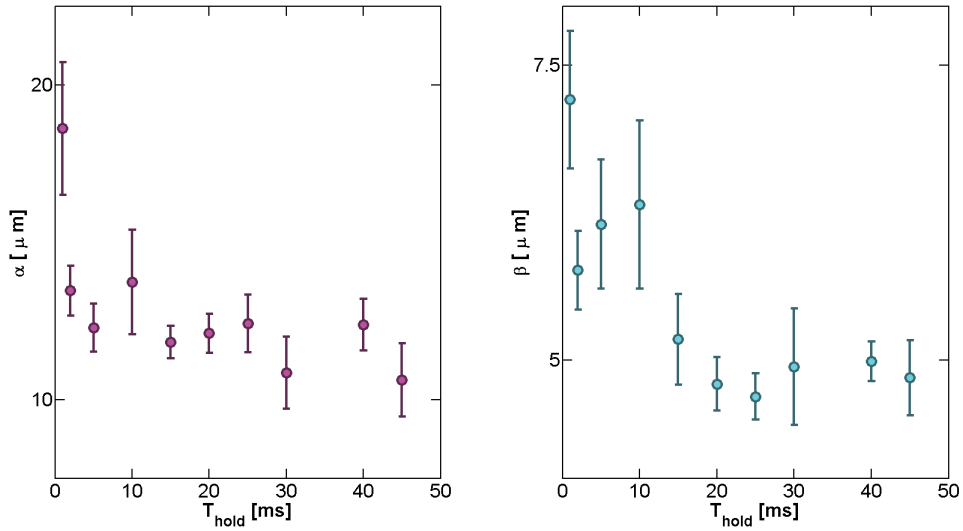

Figure 5.8: Average major and minor axis of the ellipse that the 2D JRS forms after an expansion of 10 ms. There is a general trend of both axes of the JRS's spatial extent decreasing over the evolution.

Figure 5.7 displays the average major and minor axis size over the 45 ms evolution of the pair of 2D JRSs. The JRSs are considered to be formed by 7 ms as this was the point at which their depth became consistent

between experimental sequences. The major and minor axes of the JRS after 7 ms evolution and 10 ms expansion were found to be 13 μm and 6 μm respectively. Over the course of their propagation, both major and minor axes of the JRS rarefaction are found to remain stable during propagation. If the 2D JRS were to lose energy, they would increase in physical extent. This indicates a resistance to the snake instability that lead to the rapid dynamic decay of dark solitons in the same system from the previous chapter. The resilience to dynamic decay would make the 2D JRS a good candidate for investigation into transport across disordered systems.

5.8 Orientation of the JRS

The orientation of the JRS is determined by the angular difference between the two foci that make up the JRSs. The angle given is relative to the longitudinal axis of the condensate.

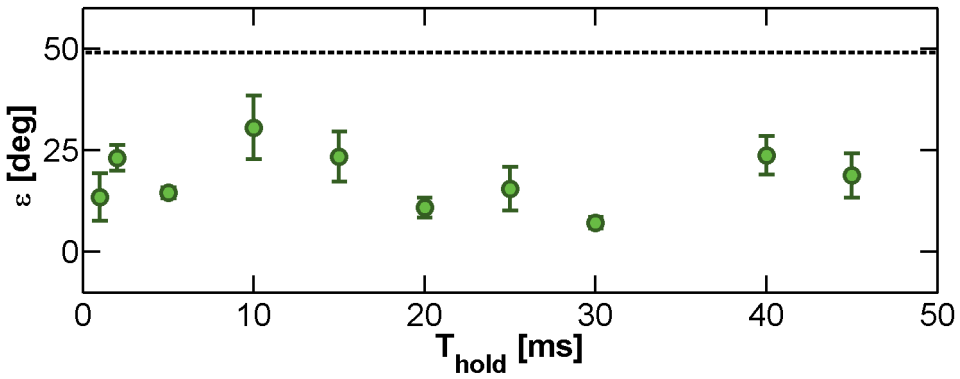

Figure 5.9: Orientation of the JRS relative the longitudinal axis of the trap.

Figure 5.9 displays the orientation of the JRS. The orientation does not vary over the course of the evolution time which indicates that there is minimal refraction as previously mentioned.

5.9 Simulation for Comparison

To verify the experimentally observed 2D JRS, computer simulations of the experimental process are performed. Using the same MatLab toolbox involved in the dark soliton simulation, GPELab, the ground state of the condensate is calculated. The number of atoms used is 40,000 with the dipole trapping frequencies of $\omega_x = 2\pi * 250$ Hz, $\omega_y = 2\pi * 40$ Hz and $\omega_z = 2\pi * 5$ Hz.

Once the energetic difference between subsequent iterations of the ground state calculation has decreased below a threshold of 2×10^{-4} in the dimensionless energy unit of the simulation, a triangular phase is applied to the condensate. A collection of vectors produce an isosceles triangle with a base width of 13.2 μm and height of 17.6 μm. The triangle is a phase factor with which the ground state is multiplied by. A phase value between 0.8 π to π were found to be best for simulated generation of the 2D JRS.

The spatially phase shifted ground state is then evolved at 0.5 ms intervals for 40 ms with the resulting phase and density distributions recorded.

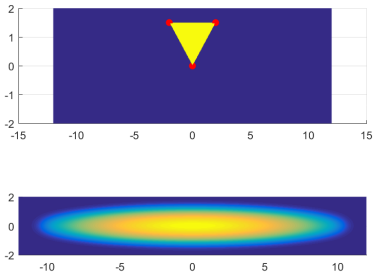

Figure 5.10: The triangular phase imprint used in simulations. The first image is of the phase distribution applied to the condensate. Yellow corresponds to phase factor of π whilst blue is zero. The simulated ground state is displayed beneath.

5.9.1 Simulation Results

The density distribution of the simulated condensate and the resulting phase is displayed in Figure 5.11. The images displayed are *in situ* which results in features being smaller than the experimental data, which is from an expanded condensate.

Figure 5.11 displays both the density distribution and phase of the JRS imprinted condensate at times ranging from 0-40 ms. The pair of 2D JRS can be picked out in the vortex-antivortex state at 10 ms before converting kinetic energy in to potential as they travel to the centre of the condensate. This results in the conversion to the rarefaction pulses by 20 ms and is reversed as the pair of 2D JRS head to the boundary.

A linear scaling factor is used in the simulation results in order to account for the difference in size due to expansion. The 10 ms expansion used in the experiment corresponds to a scaling factor $C \approx 3$.

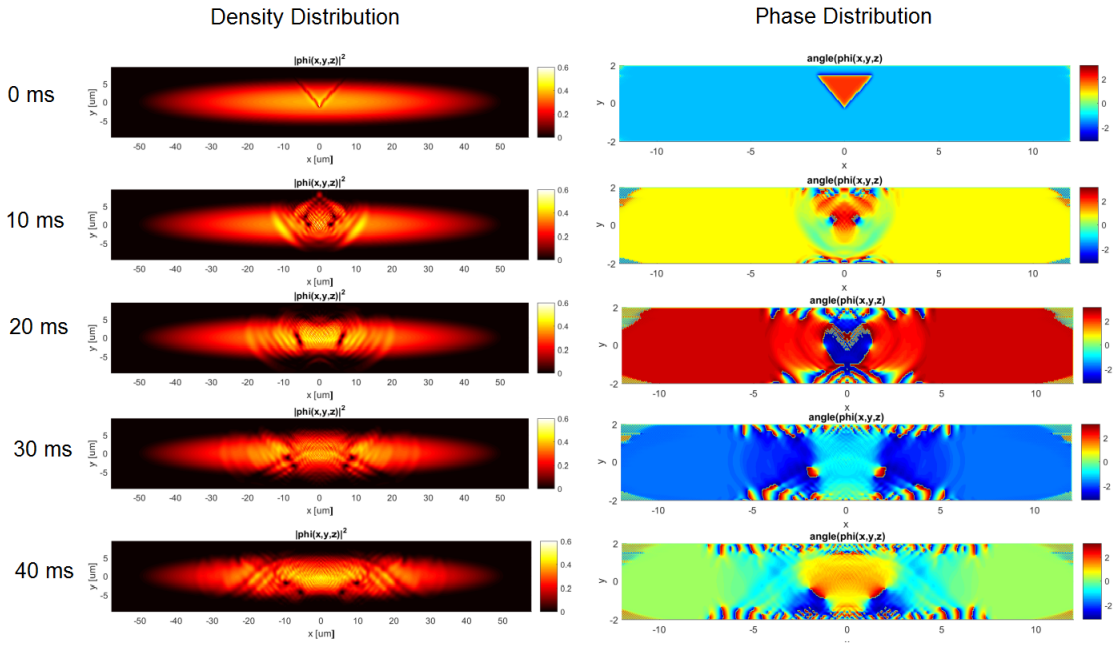

Figure 5.11: Both the density and phase distributions of the simulation up to an evolution time of 40 ms. The low density pair is the 2D JRS with the corresponding phase distribution.

Simulation Depth

Experimentally, the 2D JRS was found to require approximately 7 ms to achieve the maximum depth of 0.65 n_0, at which point it is considered fully formed. The simulation results show a similar trend, whereby the 2D JRS is visually distinguishable from other density fluctuations at a time of 8 ms. In simulation, the pair of 2D JRS start in the high energy vortex dipole state. As they propagate to the denser centre of the trap the separation of the cores decreases, resulting in the loss of vorticity and the conversion of the 2D JRS to the rarefaction phase. In Figure 5.11 the return to vortex pairs has occurred by 30 ms at which point the interaction with the boundary of the condensate separates the JRS into individual line vortices.

The 3D simulation of a triangular imprint in a condensate of the same parameters as in the experimental set up yield close fitting features and time-scales with that of the experimental results. As the simulation is in three dimensions it is possible to examine the shape of the JRS in axes that were not accessible in experimental data.

By integrating over the weak axis ω_z instead of the strong axis ω_x, it is possible to examine whether the claim that the JRS observed in experiment are two or three dimensional. As with the planar dark solitons, the density distribution from simulations show a column of low density as opposed to a ring, indicating that what is generated is a vortex line and not a vortex ring. A vortex line is the 2D extension of a point vortex

where the zero density core extends through the condensate to the other side. A vortex ring is different in that the two ends are connected to form a continuous ring.

5.9.2 Simulated JRS Shape

The simulations of the JRS imprint are analysed using the the same image processing protocol as the experimental data. Investigation of the shape of the 2D JRS generated in simulation is displayed in Figure 5.12.

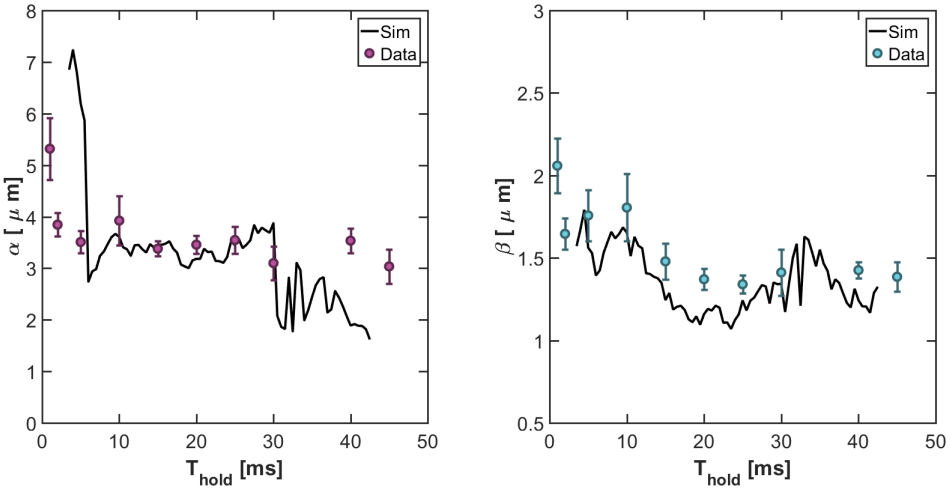

Figure 5.12: Evolution of both the major axis α and minor axis β of the 2D JRS. The line is generated from fitting the simulations, whilst points are taken from the experimental data. There is a scaling factor of $\frac{1}{3}$ which accounts for the expansion due to time-of-flight.

Figure 5.12 displays a good agreement between simulation and experiment for both major and minor axes of the 2D JRS. The experimental data is divided by a scaling factor of 3 in order to account for the expansion of the JRS during the 10 ms time-of-flight in the experimental data.

First examining the major axis α, the sharp decrease in the major axis length during the first few milliseconds is reproduced in simulation. This is believed to be the stabilisation of the 2D JRS out of the condensate motion which has generated it.

The mean velocity of the simulated 2D JRS is found to be 0.4 mms^{-1} which compares well to the measured velocity of 0.2 mm^{-1} in experiment. The discrepancy between the exact values is likely down to the stability of imprint position in experiment. Using the simulation, it is possible to examine how sensitive the path of the 2D JRS is with relation to the position of the imprint in the condensate. Changing the vertical position

of the imprint over increments as small as 0.5 μm affects the trajectory of the simulated 2D JRS. A change in imprint vertical position of 1 μm is found to remove nearly all transverse velocity, resulting in the 2D JRS forming and refracting back to the imprinted edge of the condensate. This sensitivity in experiment leads to an averaged position of the 2D JRS which could result in lower measured velocity.

During the period where the 2D JRS is still bound, the shape does not vary. This is unlike the standard planar dark solitons generated in the condensate where the soliton increases in size and decreases in depth due to loss of energy through instability. The stability in shape and depth of the observed 2D JRS in simulation and experiment is indicative of a resistance to the instabilities which affected the dark solitons.

5.10 Conclusion

To conclude, the Jones-Roberts soliton has been presented along with the properties of the three dimensional and two dimensional Jones-Roberts solitons. The form of Jones-Roberts solitons are found to vary with the soliton energy. Two dimensional Jones-Roberts solitons were generated in the experimental condensate using a phase imprint. A triangular phase distribution was identified as a shape which would result in a pair of Jones-Roberts solitons being formed. They were found to be far more stable than the dark solitons generated in the same condensate. Simulations of the imprinting process were performed in order to scrutinise the Jones-Roberts solitons with greater resolution than was achievable with the optics used in the experiment.

CHAPTER 6

OUTLOOK

The experiment is capable of investigating other areas of condensate physics, not just the topological defects induced in this thesis. One area of potential future experimental investigation could be done with regard to the Kibble-Zurek mechanism (KZM). The initial results of quench tests are presented in the following section.

A technical area for future experimental development will be full utilisation of the spatial light modulator (SLM). Initial tests of the SLM's capability with ultra-cold atoms were performed and will be detailed in this section as the beginnings of future directions.

6.1 Kibble-Zurek Mechanism Observations

The Kibble-Zurek Mechanism (KZM) describes the formation of defects in a non-equilibrium system during a second-order phase transition at a finite rate [44]. Originally proposed by T.Kibble to describe the fluctuations in density of the early universe [43], the theory was expanded for condensed matter physics by W.H. Zurek [69]. This theoretical extension brought forward a cosmological prediction into systems capable of being produced in experiment. Condensed matter systems became a testing ground for the power law scaling of defects that the KZM predicted. Bose-Einstein condensation is a clean and highly controlled system which undergoes a second-order phase transition making it an ideal system to test KZM. A second-order phase transition is characterised by a divergent correlation length near the critical point. In the case of the Bose-Einstein condensation this occurs at temperature T_c where the macroscopic population of the ground state begins.

The KZM covers the formation of causally disconnected domains across a phase transition. Beginning with a thermal gas above the quantum phase transition, fluctuations in density and energy distribute themselves

at the characteristic time-scale of the system. For a thermal gas this is set by the thermal velocity of the atoms. As the system is driven towards to the phase transition, the characteristic timescale increases and diverges at the point where the condensation begins. This divergence of the relaxation time prevents the system from following adiabatically leading to symmetry breaking.

The formation of a homogeneous phase across the condensate occurs if the velocity of the phase boundary is slower than the perturbation velocity, then fluctuations are distributed during the domain formation, generating a single domain of constant phase. In the other case, where the relaxation time is slower than the formation of phase, density variation cannot redistribute and separate domains are formed. Each domain has a distinct phase which can interact at the domain boundaries. There is possibility for the formation of phase defects which prevent the system reaching the energetic ground state. Faster quenching across the phase transition increases the number of domains, which in turn increases the rate of defect generation.

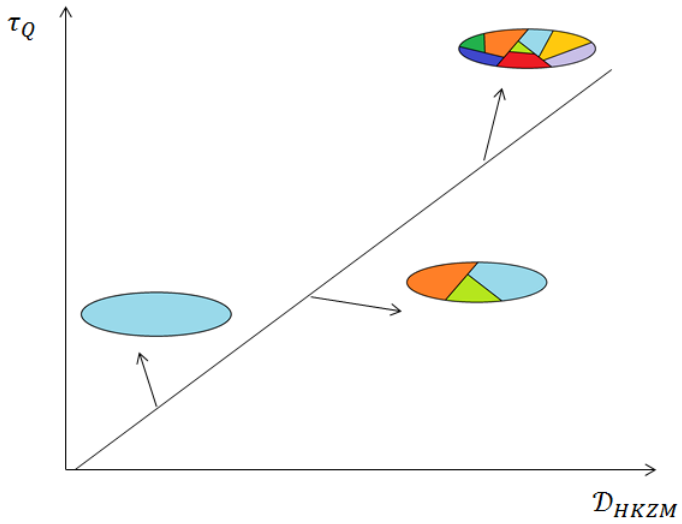

Figure 6.1: Schematic of how faster quenching rates across the critical point in the KZM increases the number of phase domains shown as different colours, leading to increased defect generation.

So far the consideration of the KZM has been for a homogeneous density distribution. In this case the whole system undergoes the phase transition at the same time at all points. The density of defects generated through a quench in a homogeneous system can be estimated using [22]

$$\mathcal{D}_{HKZM} = \frac{1}{f\xi_0^2}\left(\frac{\tau_0 2\delta}{\tau T_c(0)}\right)^{\frac{2v}{1+vz}} \sim \tau_Q^{-1/2} \tag{6.1}$$

where f is the efficiency of the process, ξ_0 is the healing length of the condensate, τ_0 is a scaling factor, δ is the linear temperature change across the critical temperature from the initial temperature $T_i = T_c(0) + \delta$ to the

final temperature $T_f = T_c(0) - \delta$, τ is the relaxation time, $T_c(0)$ is the temperature at the critical transition point and v, z are the scaling exponents which vary depending on the system the KZM is describing. The defect density rate is inversely related to the square root of the quench rate τ_Q. The scaling exponents for a homogeneous mean-field description are $v = 1/2$ and $z = 2$, which can be substituted into the defect density equation to form a relation [22].

Recent observation of spontaneous vortex generation in experimental condensates [18], including the use of the KZM as a means of solitonic vortex production [44], to further investigate the KZM scaling as well as the formation of defects milliseconds after the initial formation of the condensate. This is a difficult regime to analyse as the coarse structure of the early condensate is difficult to separate from the uncondensed cloud.

6.1.1 Experimental Production of Spontaneous Vortices

Whilst obtaining the data for the planar dark solitons, the formation of defects in the condensate were observed infrequently. Vortices with a highly reduced optical density where observed after a time-of-flight expansion. Examples of such defects are shown below

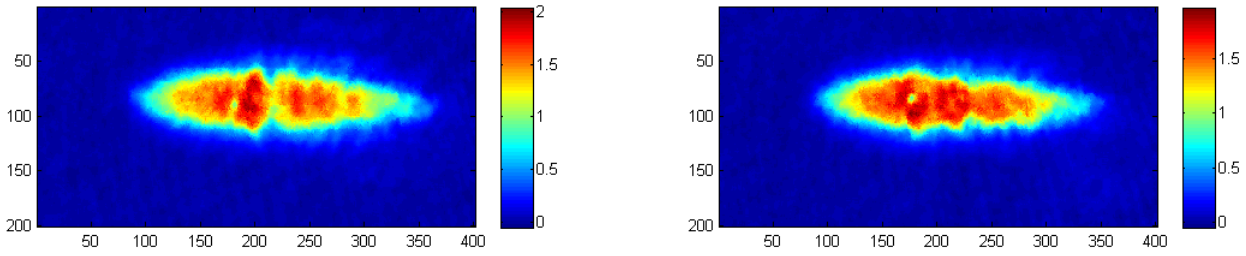

(a) 1 ms evolution after imprint

(b) 4 ms evolution after imprint

Figure 6.2: Absorption images of the condensate after phase imprinting with round density defects present. The phase imprint was made to the right side of the condensate

Within Figure 6.2 are two absorption images of condensates which have been imprint on the right-side with a blue detuned π pulse in order to generate a dark soliton. These images were different from the majority as they displayed round density defects which were random in position and high in depth. They were first considered as possible products of the imprint, however their position relative to the phase imprint

indicated that they were not directly incident with the light. Despite the separation of the imprint light and the position of the density defects it is conceivable that the imprint may have still induced the defects.

Both the quench rate of the condensate is varied as well as the final temperature of the condensate. With regard to the KZM varying both the rate of evaporation and the final temperature ultimately results in varying the only varying the quench rate. The dipole trap laser power at which condensation began was identified as 155 ±13 mW which corresponds to a temperature of 1.1 μK. The dipole trap power was linearly ramped from 155mW to 54 mW, 47 mW and 39 mW at rates between 2 seconds and 0.75s. The resultant frequency of defect generation was recorded for each combination of quenches.

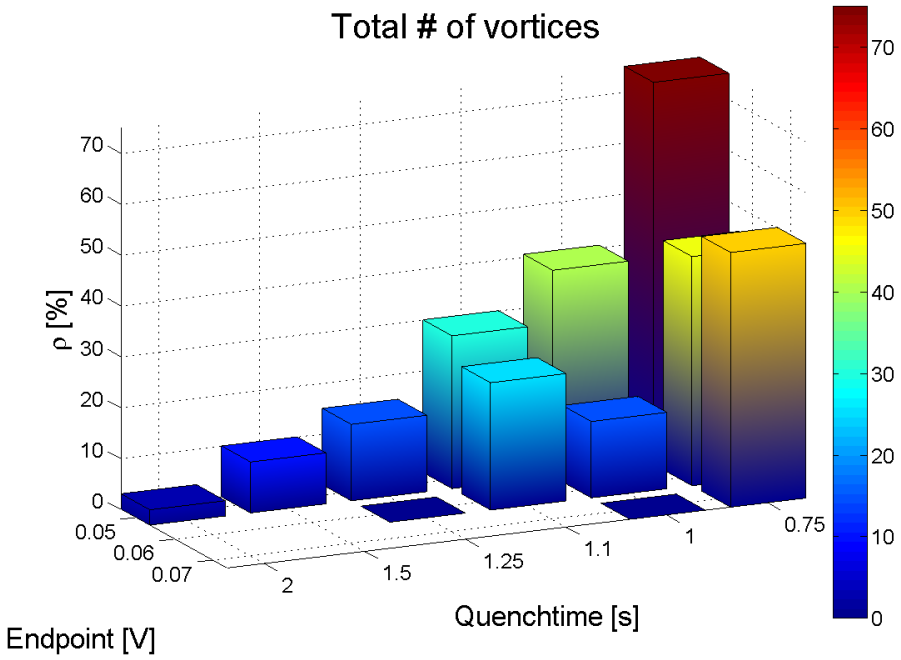

Figure 6.3: Distribution of vortex production probability for a range of quench rates and final dipole trap powers. A general trend of faster quench rates more frequently producing vortices was observed.

The general trend of Figure 6.3 show faster quenches resulted in an increased probability of vortex formation in the condensate. This is qualitatively in line with what is expected if the generation of vortices was controlled by the KZM. Further work is required in order to investigate the KZM in the very early stages of condensate formation.

6.2 SLM Potentials

Some condensate experiments aim to simulate condensed matter systems such as crystal structures in order to investigate the underlying physics of their properties. Optical lattices are used to produce the periodic structure of the crystals, albeit on larger length scales $\sim 1\mu$m. Optical lattices for atomic experiments can be produced using crossed or retro-reflected off-resonant laser beams [11]. The standing wave potential of a retro-reflected 1D lattice is given by $V_{lat} = V_0 \sin^2(kz)$ where V_0 is the lattice depth and k is the magnitude of the wave vector [24]. The limitation of a retro-reflected potential is that it can not produce irregular structures in 1D or 2D. An SLM can produce both the regular potentials required for a lattice, as well as irregular structures of arbitrary size. For an SLM, the creation of a hexagonal lattice or a 1D lattice is determined by the image. Given this flexibility, there has been previous work by other groups towards custom trapping potentials for condensates using a phase modulating SLM [13], but these SLMs are slow to update their images compared to the 10kHz refresh rate of the DMD SLM used in this work. The use of a DMD SLM to produce potentials for cold atoms has been reported recently in work by the University of Queensland [31]. The first initial potentials produced by the DMD SLM set-up for this experiment are presented in this section.

6.2.1 1D SLM Lattice

An electric field with a spatially periodic intensity distribution will apply a positionally dependent AC Stark shift to the internal energy levels of the neutral atoms [11]. This energy shift is manipulated through the coupling of the electric dipole moment of the atom to the electric field, exerting an effective potential on the atom. The depth of the lattice is given by the intensity of the of the light. The sign of the potential is determined by the sign of the detuning $\delta = \omega_L - \omega_0$, where ω_L is the frequency of the lattice laser and ω_0 is the frequency of the atomic transition being addressed. In the case of this experiment the transition is the Rb-87 D2 transition.

The simplest optical lattice is a 1D square or a squared sine wave. Generally a retro-reflected lattice produces spacings of around a micron.

In this experiment, the spatially variant light field is generated using the DMD SLM as opposed to interference of laser light. A wavelength range between 760nm-795nm allowed for flexibility in choosing an attractive or repulsive potential as the Rb87 D2 transition is 780.241 nm. Using a blue detuning ($\omega_L > \omega_{D2}$), the atoms are repelled where light is present, analogous to raising potential walls. In this case the confining harmonic potential generated by the 1550 nm trap has to remain on to confine the atoms. A red detuning

would produce an attractive lattice potential, stacking with the dipole trap potential.

This functional limit in wavelength above 780 nm had further implications. The dipole force generated by the light is inversely proportional to the detuning, however the scattering rate is inversely proportional to the detuning squared [32]. Generally heating caused through scattering events is minimised by using large detunings with high power to generate the potential. As a result, the selection of a blue detuning for initial testing was made, using a wavelength of 770 nm generating a potential barrier of 19 nK and scattering rate of 0.005 photons per second.

The simplest structure to form with the SLM is a large 1D square lattice. A sine structure is more difficult as the on/off nature of the SLM pixels makes intermediate intensities difficult to engineer. It is important to note that the 1D lattice produced by the SLM is box-like with the harmonic potential floor. This is expected to affect calculating properties such as the tunnelling rate.

The striped pattern selected has a frequency of 10 SLM pixels on, 10 SLM pixels off. This corresponds to a spatial frequency of 200 μm on the SLM before passing through the 20X microscope objective. In the atomic plane, the lattice pattern is reduced to a 10 μm period.

The atoms are held in the lattice for 200 ms. The intensity of the light in the atom plane is calculated to be 28.5 mW/cm^2, corresponding to a calculated temperature barrier of approximately 20 nK. Figure 6.4 displays the resultant distribution of atoms after the application of the SLM lattice.

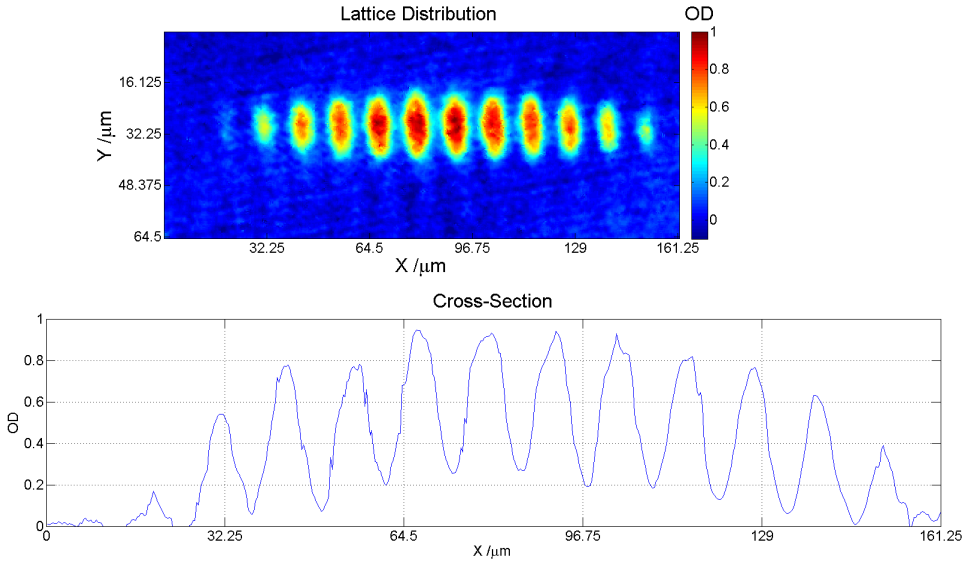

Figure 6.4: *In situ* absorption image of the condensate after the exposure of the SLM pattern using 774 nm for 200 ms after the formation of the condensate. The profile of the lattice is shown below the absorption image.

To determine if the 19 nK depth was sufficent a measure of the visibility is performed. The visibility of a fringe pattern is defined as

$$V = \frac{OD_{max} - OD_{min}}{OD_{max} + OD_{min}} \tag{6.2}$$

where $OD_{max/min}$ is the maximum and minimum optical density corresponding to the lattice peaks and troughs. With the 200 ms exposure of the SLM pattern a visibility of 87.5% is achieved. This suggests that there are still atoms which can move thermally over the barrier, linking the lattice sites. The separation of each lattice site, centre to centre, is found to be 11.3 μm. The deviation from the 10 μm lattice image is likely due to the lattice depth being too low, combined with the resolution of the image in the atomic plane. As discussed in the previous section, the resolution of an edge achieved with the 20X objectives was measured as 0.8 μ. This level of blurring at each edge of the lattice would increase the measured size of the site.

The SLM potential was applied instantly to the full power. The non-adiabatic application of the potential could generate heating. In order to determine the heating rate, the SLM potential is removed and the atoms are released from the dipole trap. If each lattice site has remained self coherent, severed from the other sites, as the individual sites expand and overlap during free fall there is matter-wave interference. The spatial frequency of the matter-wave interference after a time-of-flight is given by

$$D = \frac{ht}{Md} \tag{6.3}$$

where t is the time-of-flight, M is the mass of the Rb atom and d is the spatial period of the lattice [33].

Conversely, if the loading of the 1D lattice generated enough heat to reduce the atomic density such that the sites are no longer condensed. With a lack of condensation, there is no collective coherence and by extension no possibility of forming matter-wave interference. Each site expands ballistically and with the spatial frequency of the lattice being preserved.

Releasing the confining harmonic potential and the applied SLM lattice, and allowing a 10 ms time-of-flight, resulted in a density distribution displayed in Figure 6.5.

A fringe pattern is present after the release of the lattice implying coherence was still present after the condensate was held in the lattice for 200 ms. The spatial period of the interference fringes was found to be 4.66 μm through a fitting of a cosine function to the fringe pattern. The calculated interference fringe period using Equation 6.3 was 4.57 μm which is in good agreement with the experimentally measured value.

The visibility of the fringes was calculated to be 14.8%. The low level of visibility suggests a reduced

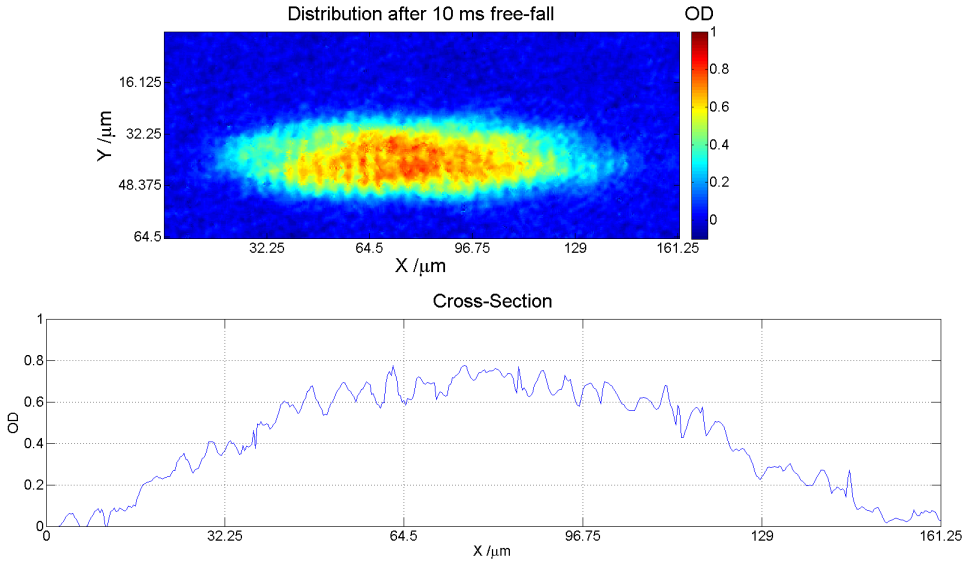

Figure 6.5: Absorption image of atoms from lattice after a 10 ms time-of-flight. The profile of the absorption image is displayed beneath showing a clear fringe pattern on the left portion of the image. The frequency of the fringe pattern was found to be 4.66 μm

coherence. The reduced coherence is mostly likely as a result of the loading of the lattice. Using a more adiabatic approach to loading the lattice such as raising the potential instead of flashing the potential on could improve coherence preservation.

6.2.2 2D Lattice and Other Potentials

The extension to the 2D lattice was performed by using chequerboard pattern. Both a 20x20 and 10x10 pixel pattern were applied to the condensate through the 20X objective. This resulted in a site size of 10 μm and 5 μm respectively. The distributions shown below are after an exposure of 764 nm for 1 s.

The purpose of such structures as an initial attempt to place atoms in 2D distributions. The distributions in Figure 6.6 display one of the potential areas for development. The SLM pattern is not faithfully produced in the corners of the squares. There are several suggestions for future improvement. Increasing the trap depth will increase the confinement in the the corners. Alternatively the pattern on the SLM can be modified to better match the desired potential. Using the flexibility of the SLM, potentials such as double wells or even complex 2D webs could be achieved. Factoring in the dynamic feature of the SLM it will be possible to generate moving potentials which could lead to controlled atomic samples being distributed and controlled with ease.

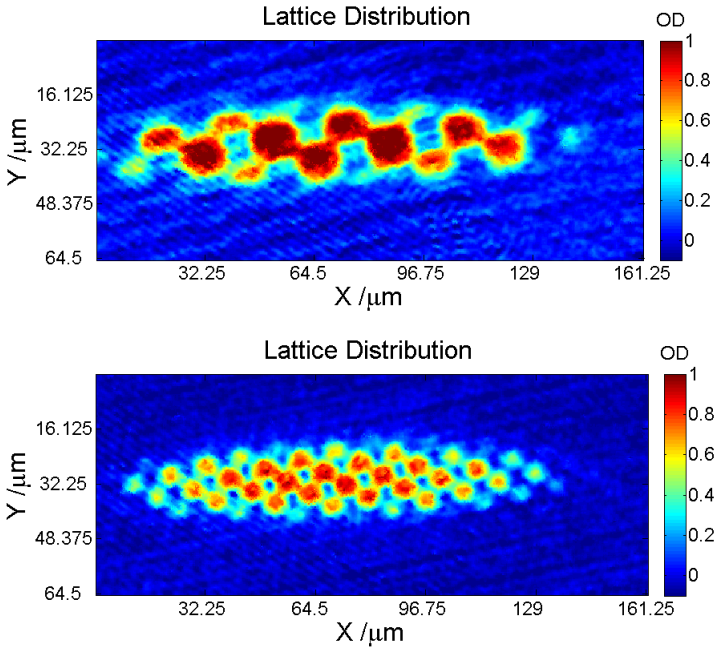

Figure 6.6: *In situ* absorption image of two 2D lattices after 1s exposure to the 764 nm SLM potential.

6.3 Conclusion

To summarise, early work into the Kibble-Zurek mechanism as a source of spontaneously generated vortices is presented. Early indications of vortex production is in keeping with the Kibble-Zurek framework. The faster quench rates result in a higher probability of vortex observation in the condensate. The initial use of the DMD SLM as a means of dipole potential manipulation is shown. Simple lattice structures are applied to the confining harmonic potential, resulting in interesting atom distributions where a small degree of coherence is still found to exist. This is measured through an interference measurement from releasing a large one dimensional lattice potential imposed on the condensate. Initial images of two dimensional SLM potentials are presented.

CHAPTER 7

CONCLUSION

The work of this thesis has been towards the investigation of dark solitons in a pancake shaped condensate. The use of a Spatial Light Modulator to develop arbitrary potentials lead to the experimental production of the theoretically predicted Jones-Roberts solitons.

The experiment has undergone technical improvements through the installation and characterisation of the optical systems around the glass cell. High resolution microscope objectives have been installed and used to image both the condensate and the imprint image reflected from the SLM.

The generation of dark solitons is achieved through a phase imprinting method where the imprint shape is controlled by the SLM. The initial dark solitons generated were shallow in depth $\sim 35\%$ and experienced a lifetime of 7 ms using a phase step of 1.3 ± 0.2 μ m. The detuning dependent direction of the dark soliton is used as a check. Improvement of the imprint step width to 0.8 ± 0.3 μm yielded an improvement in soliton depth $\sim 50\%$ resulting in a lifetime of the dark soliton of $\tau = 11.9 \pm 0.5$ ms. The dissipation of the dark soliton is discussed suggesting the soliton decays through thermal scattering.

Using a phase step of 0.6 ± 0.15 μm it was possible to generate a high energy soliton where the depth is 85%+. The rapid decay of the dark soliton in 10 ms into a pair of line vortices with a velocity of 0.13 ± 0.09 mms^{-1}. These line vortices propagate for times longer than 100 ms towards the end of the condensate at which point their positions become chaotic. This decay to line vortices is the expected product of a dynamic decay in two dimensions and is found to occur on a similar time scale in numeric 3D simulations of the experiment.

The generation of a class of soliton known as a Jones-Roberts soliton (JRS) was performed experimentally for the first time. A triangular phase imprint is produced using the SLM results in the formation of two 2D JRS. The 2D JRSs are form stable and propagate for 40 ms with a constant depth $\sim 55\%$ until reaching the

boundary of the trap. The size of the JRS in both axes is stable as it propagates, which is postulated is an effect of the JRS stability preventing energy loss as it travels through the condensate density distribution. This could make the JRS an excellent candidate for transport investigation across noisy systems.

Early work on spontaneous vortex generation through the Kibble-Zurek mechanism is presented. The probability of spontaneous vortex generation is found to increase with faster temperature quenches and lower temperature points.

Finally, the initial use of the spatial light modulator to influence the condensate distribution with a programmable dipole potential is demonstrated. Large lattice distributions are produced using different images loaded to the spatial light modulator. Coherence between lattice site is observed which suggests that the spatial light modulator has the potential to be used for more complex distributions in future. Using the area of the spatial light modulator, it would be possible to form chains of condensate populations such as multiple Josephson junctions investigating tunnelling effects.

Appendix A: Soliton Image Analysis

In this section a detailed description of the image processing techniques used to identify the soliton will be given.

The atoms are imaged using a standard technique known as absorption imaging. The atoms are first dropped, allowing them to expand. As the cloud has undergone condensation, it expands not initially under ballistic expansion, but through mean-field forces. Once the density of the cloud has become low enough through mean field expansion, ballistic expansion takes over. Allowing the cloud to expand before imaging is known as a *time-of-flight (TOF)* measurement. The soliton features in trap are smaller than the resolution limit of the optical system, so by performing an expansion it makes the features easier to detect. As the mean-field interactions become weak almost instantly out of the trap, the soliton feature will be frozen in terms of its position and shape expanding at the same rate with the condensate.

To image the soliton features a technique known as absorption imaging is used. A short pulse of resonant light is used to image the condensate. For the purpose of this work, the resonant light is that of the D2 transition of Rb-87. The atoms are highly likely to scatter the resonant light, casting a shadow on to the CCD. This form of imaging is a destructive measurement.

Two separate images are taken in order to create the absorption image; one with atoms casting a shadow and one without atoms. The atoms absorb the light casting a shadow on to the CCD in the first image. As the atoms absorb the light and re-emit, the momentum provided by the flash scatters the atoms. This makes absorption imaging a destructive measurement. A new condensate must be created after imaging the last one. A second image is then taken where there are no atoms. Comparing the difference between the two images produces the distribution and density of the atoms.

Optical fringes can vary in position and intensity between the "atoms" and "no-atoms" images. The fringes are produced through retro-reflections in the science cell glass or scattering around dust particles on the glass surface. These fringes are generally stable between images but can lead to misleading effects. If the fringe varies between the atoms and no-atoms images then large remnants can remain. A defringing algorithm is used to remove fringes by creating a library of "no-atoms" images. The algorithm looks for the best linear combination of library images to generate a "no-atoms" image that will remove the fringes in the "atoms" image as completely as possible.

Once the de fringing algorithm has completed, the subtracted image is converted into optical density by $OD = -log(Atoms/DefringedNo - Atoms)$. It is then background corrected by examining a portion of the image, where no atoms are present, to account for any difference in intensity between the two images. Any

difference found is added to adjust the background.

A 5x5 smoothing filter is applied to the image in order to aid the program to find the centre and edges of the BEC. The data is then normalised and a bimodal fit of a parabola for the BEC, and a Gaussian for the thermal cloud. This is done to find the centre of the condensate in the image as the position of condensate can vary from image to image. The fit is subtracted from the data to highlight any deviation from the expected shape. This highlights density features such as solitons and vortices. Each column of the subtraction is summed as a dark soliton appears as a large negative collection of columns. The position of this minimum in the image is used to set the initial position parameter for the soliton fitting routine.

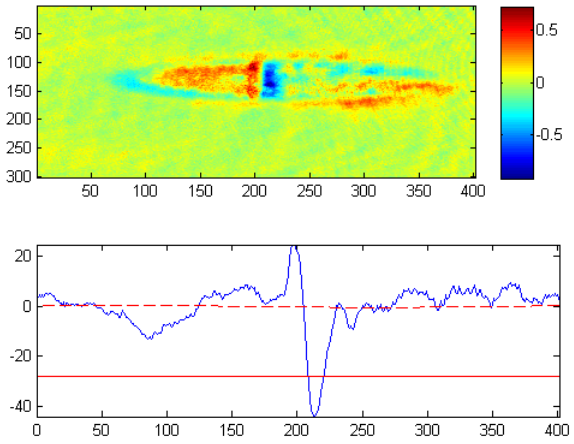

Figure 1: Example of subtraction of 2D bimodal fit from experimental data. The red areas highlight high density regions and blue the low density regions which are then summed below to aid the initial settings of the soliton fitting process.

A least-squares fit is used to calculate the soliton depth, size and position in a cut through the center of the condensate. This is first done with the smoothed data and then the unfiltered data as check that there aren't any large deviations due to the image processing. The plots presented will be using fits of the unfiltered data.

Appendix B: Optical Molasses

Optical molasses is a cooling technique which relies on the interaction of the atom and counter propagating laser beams. It was first observed experimentally by Chu *et al* [19]. The molasses process utilises the Doppler shift generated by the motion of the atom relative to the counter propagating laser beams.

The force experienced by the atom moving in one dimension inside a pair of counter propagating beams is given by [29]

$$F_{molasses} = F_{scatt}(\omega_L - \omega - kv) - F_{scatt}(\omega_L - \omega + kv) \tag{1}$$

$$\simeq F_{scatt}(\omega_L - \omega_0) - kv\frac{\delta F}{\delta \omega} - \left[F_{scatt}(\omega_L - \omega_0) + kv\frac{\delta F}{\delta \omega}\right] \tag{2}$$

$$\simeq -2kv\frac{\delta F}{\delta \omega} \tag{3}$$

where low velocities $kv \ll \Gamma$ are assumed. The motion of the atom towards one of the beams will lead to a Doppler shift resulting in an increased probability of scattering the counter propagating beam relative to the atom. This is displayed in Figure 2

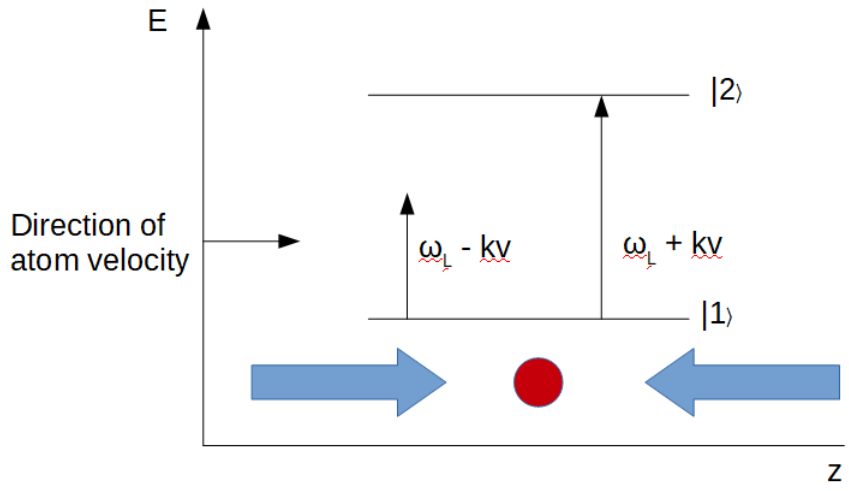

Figure 2: Optical molasses energy diagram for an atom in the rest frame with velocity v. The arrow to the right indicates the direction of motion for the atom. As the frequency of the laser light ω_L is detuned away from resonance ω_0, the counter propagating beam $\omega_L + kv$ is more likely to scatter the moving atom. This results in a friction force against the atom as the direction of the de-excited photon is random and produces no net force over many cycles.

The force experienced by the atom can be considered a friction of the form $F_{molasses} = -\alpha v$ where α is

given by

$$\alpha = 2k\frac{\delta F}{\delta \omega} = 4\hbar k^2 \frac{I}{I_{sat}} \frac{-2\delta/\Gamma}{I_{sat}[1+(2\delta/\Gamma)^2]^2} \tag{4}$$

where I is the intensity of the laser light, I_{sat} is the saturation intensity for the atomic transition, δ is the detuning and Γ is the linewidth of the atomic transition. The laser light frequency ω_L is detuned below the atomic transition frequency ω_0.

This technique provides a damping force for a range of velocities, where the molasses force is theoretically zero at $v = 0$. This is not a physical limit as there are heating effects from fluctuations in the force. The temperature limit T_D of the Doppler cooling technique is given by [29]

$$k_B T_D = \frac{\hbar\Gamma}{2} \tag{5}$$

For the D2 transition of Rb-87 this corresponds to a temperature limit of T_D =145 μK.

LIST OF REFERENCES

[1] Charlotte Alicia and Susan O Neale. *Towards solitons in a 2D BEC*. PhD thesis, University of Birmingham, 2014.

[2] B. P. Anderson, P. C. Haljan, C. a. Regal, D. L. Feder, L. a. Collins, C. W. Clark, and E. a. Cornell. Watching Dark Solitons Decay into Vortex Rings in a Bose-Einstein Condensate. *Physical Review Letters*, 86(14):2926–2929, 4 2001.

[3] M. H. Anderson, J. R. Ensher, M. R. Matthews, C. E. Wieman, and E. A. Cornell. Observation of Bose-Einstein Condensation in a Dilute Atomic Vapor. *Science*, 269(5221):198–201, 1995.

[4] X Antoine and R Duboscq. GPELab: A Matlab toolbox for computing stationary solutions and dynamics of Gross-Pitaevskii Equations (GPE), User-guide,(2013).

[5] Gaetano Assanto, Luis A. Cisneros, Antonmaria A. Minzoni, Benjamin D. Skuse, Noel F. Smyth, and Annette L. Worthy. Soliton steering by longitudinal modulation of the nonlinearity in waveguide arrays. *Physical Review Letters*, 104(5):17–19, 2010.

[6] Mathis Baumert. *Dipole traps and optical lattices for quantum simulations*. PhD thesis, University of Birmingham, 2012.

[7] Christoph Becker. Multi component Bose-Einstein condensates From mean field physics to strong Dissertation. 2008.

[8] Christoph Becker, Simon Stellmer, Parvis Soltan-Panahi, Sren Dörscher, Mathis Baumert, Eva-Maria Richter, Jochen Kronjäger, Kai Bongs, and Klaus Sengstock. Oscillations and interactions of dark and darkbright solitons in BoseEinstein condensates. *Nature Physics*, 4(6):496–501, 5 2008.

[9] Natalia Berloff. *Stationary and Time Dependent Gross-Pitaevskii Equations*. American Mathematical Society, 2006.

[10] Natalia G Berloff. Interactions of vortices with rarefaction solitary waves in a Bose-Einstein condensate and their role in the decay of superfluid turbulence. 053601:1–7, 2004.

[11] Immanuel Bloch. Ultracold quantum gases in optical lattices. *Nature Physics*, 1(1):23–30, 2005.

[12] Satyendranath Bose. Planck's law and the light quantum hypothesis. *Journal of Astrophysics and Astronomy*, 15(1):3–7, 1976.

[13] Graham D Bruce, Matthew Y H Johnson, Edward Cormack, David a W Richards, James Mayoh, and Donatella Cassettari. Feedback-enhanced algorithm for aberration correction of holographic atom traps. *Journal of Physics B: Atomic, Molecular and Optical Physics*, 48(11):115303, 2015.

[14] S. Burger, K. Bongs, S. Dettmer, W. Ertmer, K. Sengstock, a. Sanpera, G. V. Shlyapnikov, and M. Lewenstein. Dark Solitons in Bose-Einstein Condensates. *Physical Review Letters*, 83(25):5198–5201, 12 1999.

[15] S. Burger, L. D. Carr, P. Öhberg, K. Sengstock, and a. Sanpera. Generation and interaction of solitons in Bose-Einstein condensates. *Physical Review A*, 65(4):043611, 4 2002.

[16] Th. Busch and J. R. Anglin. Motion of Dark Solitons in Trapped Bose-Einstein Condensates. *Physical Review Letters*, 84(11):2298–2301, 3 2000.

[17] Y. Castin and R. Dum. Bose-Einstein Condensates in Time Dependent Traps. *Physical Review Letters*, 77(27):5315–5319, 1996.

[18] Lauriane Chomaz, Laura Corman, Tom Bienaimé, Rmi Desbuquois, Christof Weitenberg, Sylvain Nascimbène, Jrme Beugnon, and Jean Dalibard. Emergence of coherence via transverse condensation in a uniform quasi-two-dimensional Bose gas. *Nature Communications*, 6:6162, 2015.

[19] Steven; L. Hollberg; J. E. Bjorkholm; Alex Cable; A. Ashkin Chu. Three-Dimensional Viscous Confinement and Cooling of Atoms by Resonance Radiation Pressure. 33(3):123–126, 1985.

[20] Claude Cohen Tannoudji. Chapter 20. In *Advances in atomic physics : an overview*, chapter 20, pages 515–518. 2011.

[21] Franco Dalfovo, Stefano Giorgini, LP Pitaevskii, and Sandro Stringari. Theory of Bose-Einstein condensation in trapped gases. *Reviews of Modern Physics*, 71(3):463–512, 1999.

[22] A. Del Campo, A. Retzker, and M. B. Plenio. The inhomogeneous Kibble-Zurek mechanism: Vortex nucleation during Bose-Einstein condensation. *New Journal of Physics*, 13:1–11, 2011.

[23] J. Denschlag. Generating Solitons by Phase Engineering of a Bose-Einstein Condensate. *Science*, 287(5450):97–101, 1 2000.

[24] D. Dickerscheid, D. van Oosten, P. Denteneer, and H. Stoof. Ultracold atoms in optical lattices. *Phys. Rev. A*, 68(4):1–13, 2003.

[25] L. Dobrek, M. Gajda, M. Lewenstein, K. Sengstock, G. Birkl, and W. Ertmer. Optical Generation of Vortices in trapped Bose-Einstein Condensates. page 8, 7 1999.

[26] Daniel M. Farkas, Evan A. Salim, and Jaime Ramirez-Serrano. Production of Rubidium Bose-Einstein Condensates at a 1 Hz Rate. pages 1–14, 2014.

[27] M. Fattori, C. D'Errico, G. Roati, M. Zaccanti, M. Jona-Lasinio, M. Modugno, M. Inguscio, and G. Modugno. Atom interferometry with a weakly interacting bose-einstein condensate. *Physical Review Letters*, 100(8):1–5, 2008.

[28] P O Fedichev, A E Muryshev, and G V Shlyapnikov. 1 . 60(4):3220–3224, 1999.

[29] Christopher J Foot. Atomic Physics. *Nature*, 71(2):35–6, 2005.

[30] Rudolf Gati. *Bose-Einstein Condensates in a Single Double Well Potential*. PhD thesis, 2007.

[31] G. Gauthier, I. Lenton, N. McKay Parry, M. Baker, M. J. Davis, H. Rubinsztein-Dunlop, and T. W. Neely. Configurable microscopic optical potentials for Bose-Einstein condensates using a digital-micromirror device. pages 1–9, 2016.

[32] Rudolf Grimm, Matthias Weidemüller, and Yurii B. Ovchinnikov. Optical dipole traps for neutral atoms. page 39, 2 1999.

[33] Zoran Hadzibabic, Sabine Stock, Baptiste Battelier, Vincent Bretin, and Jean Dalibard. Interference of an array of independent Bose-Einstein condensates. *Physical Review Letters*, 93(18):1–4, 2004.

[34] Thomas Heimburg and Andrew D Jackson. On soliton propagation in biomembranes and nerves. *Proceedings of the National Academy of Sciences of the United States of America*, 102(28):9790–5, 7 2005.

[35] Michael Holynski. *Creating a two dimensional cold mixture experiment*. PhD thesis, University of Birmingham, 2012.

[36] Guoxiang Huang, Valeri a. Makarov, and Manuel G. Velarde. Two-dimensional solitons in Bose-Einstein condensates with a disk-shaped trap. *Physical Review A*, 67(2):023604, 2 2003.

[37] A D Jackson, G M Kavoulakis, and C J Pethick. Solitary waves in clouds of Bose-Einstein condensed atoms. *Physical Review A*, 58(3):2417–2422, 9 1998.

[38] Dylan Jervis and Joseph H. Thywissen. Making an ultracold gas. page 16, 1 2014.

[39] C Jones and P H Roberts. Motions in a Bose condensate. IV. Axisymmetric solitary waves. *Journal of Physics A: Mathematical and General*, 15(8):2599–2619, 1982.

[40] W. Ketterle, D. S. Durfee, and D. M. Stamper-Kurn. Making, probing and understanding Bose-Einstein condensates. page 90, 4 1999.

[41] Wolfgang Ketterle, M R Andrews, K B Davis, D S Durfee, D M Kurn, M O Mewes, and N J van Druten. BoseEinstein condensation of ultracold atomic gases. *Physica Scripta*, T66(April):31–37, 1996.

[42] L. Khaykovich, F. Schreck, G. Ferrari, T. Bourdel, J. Cubizolles, L. D. Carr, Y. Castin, and C. Salomon. Formation of a matter-wave bright soliton. *Science*, 296(5571):1290–1293, 2002.

[43] T W B Kibble. Topology of cosmic domains and strings. *Journal of Physics A: Mathematical and General*, 9(8):1387–1398, 2001.

[44] Giacomo Lamporesi, Simone Donadello, Simone Serafini, Franco Dalfovo, and Gabriele Ferrari. Spontaneous creation of KibbleZurek solitons in a BoseEinstein condensate. *Nature Physics*, 9(10):656–660, 9 2013.

[45] C. T. Law and G. a. Swartzlander, Jr. Optical vortex solitons and the stability of dark soliton stripes. *Optics Letters*, 18(8):586, 1993.

[46] S Levy, E Lahoud, I Shomroni, and J Steinhauer. The a.c. and d.c. Josephson effects in a Bose-Einstein condensate. *Nature*, 449(7162):579–83, 10 2007.

[47] K.W. Madison, F. Chevy, and W. Wohlleben. Vortex formation in a stirred Bose-Einstein condensate. *Physical review letters*, 84(5):806–809, 2000.

[48] a. Mamaev, M. Saffman, and a. Zozulya. Propagation of Dark Stripe Beams in Nonlinear Media: Snake Instability and Creation of Optical Vortices. *Physical Review Letters*, 76:2262–2265, 1996.

[49] Nadine Meyer. *Building and characterisation of a dual species quantum simulator*. PhD thesis, University of Hamburg, 2014.

[50] Nadine Meyer, Harry Proud, Marisa Perea-Ortiz, Charlotte ONeale, Mathis Baumert, Michael Holynski, Jochen Kronjäger, Giovanni Barontini, and Kai Bongs. Observation of Two-Dimensional Localized Jones-Roberts Solitons in Bose-Einstein Condensates. *Physical Review Letters*, 119(15):150403, 2017.

[51] Rowan W. G. Moore, Lucie A. Lee, Elizabeth A. Findlay, Lara Torralbo-Campo, Graham D. Bruce, and Donatella Cassettari. Measurement of Vacuum Pressure with a Magneto-Optical Trap: a Pressure-Rise Method. pages 1–4, 2014.

[52] T. Müller, T. Wendrich, M. Gilowski, C. Jentsch, E. M. Rasel, and W. Ertmer. Versatile compact atomic source for high-resolution dual atom interferometry. *Physical Review A - Atomic, Molecular, and Optical Physics*, 76(6), 2007.

[53] A. Muryshev, G. V. Shlyapnikov, W. Ertmer, K. Sengstock, and M. Lewenstein. Dynamics of Dark Solitons in Elongated Bose-Einstein Condensates. *Physical Review Letters*, 89(11):110401, 8 2002.

[54] Marisa Perea Ortiz. *Progress towards a quantum simulator with cold atoms*. PhD thesis, University fo Birmingham, 2014.

[55] N P Proukakis, N G Parker, D J Frantzeskakis, and C S Adams. Analogies between dark solitons in atomic BoseEinstein condensates and optical systems. *Journal of Optics B: Quantum and Semiclassical Optics*, 6(5):S380–S391, 2004.

[56] L. A. Smirnov and V. A. Mironov. Dynamics of two-dimensional dark quasisolitons in a smoothly inhomogeneous Bose-Einstein condensate. *Physical Review A - Atomic, Molecular, and Optical Physics*, 85(5):1–12, 2012.

[57] N L Smith, W H Heathcote, G Hechenblaikner, E Nugent, and C J Foot. Quasi-2D confinement of a BEC in a combined optical and magnetic potential. *Journal of Physics B: Atomic, Molecular and Optical Physics*, 38(3):223–235, 2005.

[58] Roger K. Smith. Travelling waves and bores in the lower atmosphere: the 'morning glory' and related phenomena. *Earth Science Reviews*, 25(4):267–290, 1988.

[59] Kurchatov Square. Stability of standing matter waves in a trap. 60(4):2665–2668, 1999.

[60] Daniel A Steck. Rubidium 87 D Line Data. pages 1–29, 2003.

[61] Jeff Steinhauer. Observation of thermal Hawking radiation and its entanglement in an analogue black hole. *Nature Physics*, 12(August):1–14, 2016.

[62] S. Stellmer, C. Becker, P. Soltan-Panahi, E.-M. Richter, S. Dörscher, M. Baumert, J. Kronjäger, K. Bongs, and K. Sengstock. Collisions of Dark Solitons in Elongated Bose-Einstein Condensates. *Physical Review Letters*, 101(12):120406, 9 2008.

[63] V Tikhonenko, J Christou, B Luther-Davies, and Y S Kivshar. Observation of vortex solitons created by the instability of dark soliton stripes. *Optics letters*, 21(15):1129–1131, 1996.

[64] Marios C. Tsatsos, Pedro E S Tavares, Andre Cidrim, Amilson R. Fritsch, Monica A. Caracanhas, F. Ednilson A dos Santos, Carlo F. Barenghi, and Vanderlei S. Bagnato. Quantum turbulence in trapped atomic Bose-Einstein condensates. *Physics Reports*, 622:1–52, 2016.

[65] Nikolay K. Vitanov, Amin Chabchoub, and Norbert Hoffmann. Deep-water waves : On the nonlinear Schrödinger equation and its solutions. *Journal of Theoretical and Applied Mechanics*, 43(2):1–11, 2013.

[66] Gregor Weihs, Thomas Jennewein, Christoph Simon, Harald Weinfurter, and Anton Zeilinger. P Hysical R Eview Letters. *Physical Review Letters*, 82(February):1–5, 1998.

[67] R. I. Woodward and E. J. R. Kelleher. Dark solitons in laser radiation build-up dynamics. 032221(January):1–7, 2016.

[68] Tarik Yefsah, Ariel T Sommer, Mark J H Ku, Lawrence W Cheuk, Wenjie Ji, Waseem S Bakr, and Martin W Zwierlein. Heavy solitons in a fermionic superfluid. *Nature*, 499(7459):426–30, 7 2013.

[69] Wojciech H. Zurek. Cosmological experiments in superfluid helium. *Nature*, 317:505–508, 1985.